A new concept of data assimilation method between PC-MRI measurement and CFD simulation of blood flow analysis on patient-specific cerebral aneurysm

MOHD AZRUL HISHAM BIN MOHD ADIB

MARCH 2017

A new concept of data assimilation method between PC-MRI measurement and CFD simulation of blood flow analysis on patient-specific cerebral aneurysm

A dissertation submitted to
THE GRADUATE SCHOOL OF ENGINEERING SCIENCE
OSAKA UNIVERSITY
In partial fulfillment of the requirements for the degree of
DOCTOR OF PHILOSOPHY IN ENGINEERING

By
MOHD AZRUL HISHAM BIN MOHD ADIB

MARCH 2017

ABSTRACT

Computational fluid dynamics (CFD) analysis has been extensively performed to investigate patient-specific blood flow fields and hemodynamics factors on the cerebral aneurysm. There are two key issues for the patient-specific CFD simulation; one is realistic vessel geometry, and the other is boundary condition. Meanwhile, the cerebral aneurysm often develops at the bifurcation of cerebral arteries, so the analysis of the model with multiple outlet boundaries remains a critical issue. On the other hand, according to the advancement in medical imaging technique, blood flow field is able to be obtained invasively using phase contrast magnetic resonance imaging (PC-MRI). Unfortunately, since the current spatial resolution of the PC-MRI is insufficient to reproduce the blood flow field in cerebral vessels with a diameter of a few millimeters, with directly using PC-MRI velocity profile. In this regard, various approaches to combine the numerical simulation and measurement data, so-called data assimilation (DA) have been recently developed for blood flow problems. This thesis conducts a computational approach based data assimilation on reducing the velocity differences between the PC-MRI measurement and the CFD simulation on the patient-specific aneurysm.

In the first part of the thesis, the effects of extracted patient-specific geometries with different threshold image intensities on flow solution were investigated by using CFD studies. The reconstruction of the vessel geometries was derived using the determination threshold coefficient (C_{thres}) method and the blood flow analyses were conducted by a pressure fixed (*P*-fixed) approach and flow-rate control (*Q*-control) approach, where expresses the outlet boundary in CFD analysis as an *ad hoc* outlet pressure and adjustment the outlet pressure by modified the flow rate difference respectively. The results exhibited that the inlet area and volume of the vascular model decrease as the value C_{thres} increases, whereas the wall shear

stress (WSS) distribution increases as C_{thres} increases. The minimum velocity difference between PC-MRI measurement and CFD simulation was obtained at a C_{thres} value of 0.3. This relationship potentially gives the physically adequate realistic vessel geometry to achieve the minimum value of velocity difference on flow fields for each patient.

Next, the study was focused to propose a basic framework for imposing a pressure condition on the outlet boundary in order to minimize the velocity differences between PC-MRI measurement and CFD simulation. The velocity-field optimized (V-optimized) approach was proposed to couple velocity fields in the measurement and computation, in which a set of pressure values on outlet boundary is determined based on an optimization problem. This present approach solves the direct problem iteratively. To evaluate the effects of imposing the outlet pressure, this P-fixed approach, Q-control approach, and V-optimized approach (the present approach) were compared. The result showed that, the highest reduction in velocity difference occurs at the V-optimized approach, where the velocity difference (normalized by inlet velocity) is 19.3%. This present approach also confirmed that the differences in boundary treatments affect the WSS values in both local domains for an aneurysm and non-aneurysm region.

For the consideration of improvement on the exhaustive search to find the optimal solution in V-optimized approach, a novel data assimilation method for patient-specific blood flow analysis based on conventional feedback control theory called the *physically consistent feedback control-based data assimilation* (PFC-DA) method was proposed. In the PFC-DA method, the signal was attributed to a residual velocity difference between the numerical and measured velocities, which is cast as a source term in a Poisson equation for the potential scalar field that induces flow in a closed system. The pressure values at the inlet and outlet boundaries are recursively calculated by this potential scalar field. Through the feasibility study on the PFC-DA method demonstrated the flow was automatically separated into respective daughter

branches by determining the boundary pressure and the higher resolution in computational mesh provides the WSS profile. As compared with the proposed *V*-optimized approach, although this PFC-DA method does not guarantee the optimal solution, only one additional Poisson equation for the scalar potential is required, providing an improvement for such a small additional computational cost. These achievements clearly exhibit a huge potential of the new direction in patient-specific PC-MRI integrated blood flow analysis for a cerebral aneurysm.

TABLE OF CONTENTS

Chapter 3

Minimizing the blood velocity difference between PC-MRI and CFD simulation in cerebral arteries and aneurysms

Chapter 4

The feasibility study of physically consistent feedback control based data assimilation (PFC-DA) methods on patient-specific aneurysms

LIST OF ABBREVIATIONS

PC-MRI	Phase Contrast Magnetic Resonance Imaging
CFD	Computational Fluid Dynamics
WSS	Wall Shear Stress
VOF	Volume of Fluids
BDIM	Boundary Data Immersion Method
PFC-DA	Physically Consistent Feedback Control based Data Assimilation
CFL	Courant Friedrichs Lewy
DSA	Digital Subtraction Angiology
ICA	Internal Carotid Artery
VENC	Velocity Encoding
TOF	Time of Flight
FA	Flip Angle
FOV	Field of View
ICP	Iterative Closest Point

LIST OF FIGURES

LIST OF TABLES

Chapter 1

Introduction

1.1 Cerebral aneurysm

Cerebrovascular disease is a vascular disease of the cerebral circulation. Most commonly this is a stroke or mini-stroke and sometimes can be a hemorrhagic stroke. The number of deaths for cerebrovascular disease has decreased at the peak of the 1960s due to advances in medical technology, and it is the fourth largest after a brain tumor, heart disease, and pneumonia in statistics of 2012 [1]. Since cerebrovascular diseases are directly related to injury or necrosis of brain tissue, many cases died immediately after rupture; it is known as a disease that causes serious sequelae even if it survives, which causes a long-term care condition (Ministry of Health, Labor and Welfare 2013). Subarachnoid hemorrhage, a major cerebrovascular disease, is one of the cerebral hemorrhages occurring at the bottom of the brain, and 75% of this disease is caused by rupture of a cerebral aneurysm [1]. A cerebral aneurysm is a common vascular disease characterized by local ballooning of a cerebral artery and usually occurs at the bifurcations and branches of the large arteries, typically in the circle of Willis, as shown in Fig. 1.1 [2]. Approximately 85% of the aneurysms develop in the anterior part of the circle of Willis and involve the internal carotid arteries and their major branches that supply the anterior and middle sections of the brain. About 1.5% to 5% of the general population had developed a cerebral aneurysm and recorded about 3 to 5 million people in the United States have cerebral aneurysms, but most are not producing any symptoms [3]. Between 0.5% and 3% of people with a brain aneurysm may suffer from bleeding. The risk of rupture varies depending on the aneurysm location and size. Recent epidemiological analyses show that the

overall prevalence of a cerebral aneurysm is 3.2% in a population without the comorbidity [3]. Even in cases of survived patients, 1:3 ratio of survivors remain dependent [4], and then their quality of life seems to be significantly reduced.

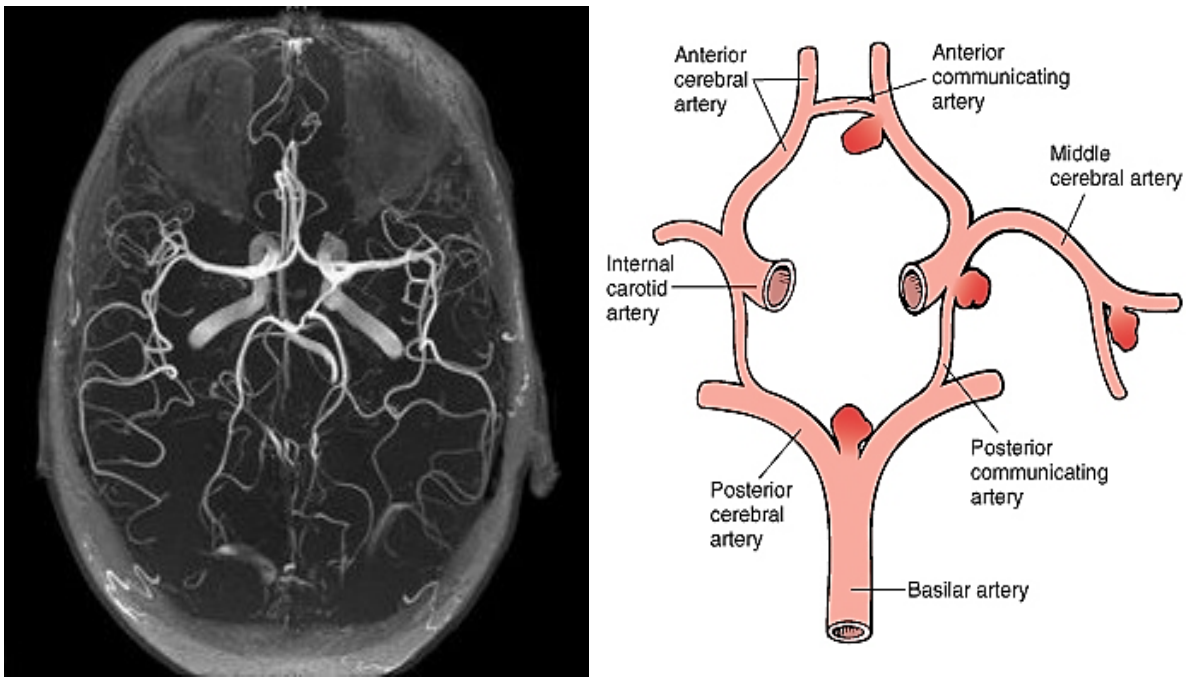

Figure 1.1 Schematic representation of the Circle of Willis by [2]. CT angiography of cerebral arteries (*left*) and the cerebral aneurysms in the circle of Willis (*right*)

Furthermore, the treatment method to prevent the aneurysm rupture is limited to the surgical method, and thus the treatment of cerebral aneurysms includes the severe risk of the internal bleeding. Whereas, the risk of the aneurysm rupture is not substantially high. Reported by [4], for the five-year risk of the aneurysm rupture was 3.4% but in one-year risk was only 1.4%. As a result of the review, the annual rupture rate of a cerebral aneurysm in the Japanese population is 2.7% [5].

1.2 Computational fluid dynamics (CFD) analysis on cerebral aneurysm

In order to acquire blood flow velocity and pressure distribution in cerebral blood vessels, CFD analysis is broadly performed using a vascular model constructed from images captured by measuring devices such as PC-MRI, CT, and ultrasonic measurement. By CFD analysis, it becomes possible to acquire blood flow dynamics and mechanical field in the blood vessel which cannot be obtained by measurement. The relationship between wall shear stress (WSS) and viscosity of the blood is influenced by the growth and rupture process of a cerebral aneurysm [6]. There are extensive studies on the shear stress applied to the surface. However, in a previous study investigating the rupture factor by CFD analysis, it was reported that locally high shear stress [7] applied to the aneurysm wall contributes to rupture, and relatively low shear stress [8] has been reported to be involved in rupture. Different factors such as assumptions, model shapes and boundary conditions in mathematical models can be considered as causes of different report results. In particular, since the blood flow velocity obtained from a healthy subject as a boundary condition and the value obtained from the past literature are set as the boundary condition in the existing study, the primary cause is considered to be a uniform setting of the boundary condition. By [9] reported, there are changed the velocity at the inlet boundary condition based on parameters such as Reynolds number using a model that developed a cerebral aneurysm in the arterial bifurcation, perform by CFD analysis. As a result, the flow distribution after branching depends on the value of velocity inlet boundary and it is affected where the wall shear stress is low. Thus, the boundary condition setting is important when considering hemodynamics individual patient-specific aneurysm.

1.3 Phase contrast magnetic resonance imaging (PC-MRI) measurement and blood flow information

Magnetic resonance imaging is widely accepted by clinicians as a valuable tool for diagnosing cardiac and vascular diseases, measuring disease severity and assessing patient response to medical and surgical therapy. The technique has been further developed over the last few decades to provide not only morphological information on cardiovascular anatomy, but also functional information on cardiac perfusion, myocardial viability, and blood flow. Since the original description in the 1980s [10], [11], [12], phase contrast magnetic resonance imaging (PC-MRI) has seen broad clinical acceptance for the visualization and quantitative evaluation of blood flow in the heart, aorta and large vessels [13]. Further development of PC-MRI techniques has allowed for the acquisition of a time-resolved (CINE), three-dimensional (3D) PC-MRI with three-directional velocity encoding which is often referred to as "4D flow MRI. The combination of 3D blood flow visualization with flow quantification enables a new and previously unfeasible comprehensive evaluation of the impact of cardiovascular pathologies on global and local changes in cardiac or vascular hemodynamics [14], [15]. An important PC-MRI parameter is the *VENC*, which represents the maximum flow velocity that can be acquired. It is important to note, that velocity noise is directly related to the *VENC* [16]. Therefore, selecting a high *VENC* may alleviate the issue of velocity aliasing but will also increase the level of velocity noise in flow velocity images. The *VENC* should ideally select as high as needed to avoid aliasing but as low as possible to reduce velocity noise. As a general rule, to capture the best image quality, the chosen *VENC* should represent the physiological velocity of the vessel of interest and be adapted to the measurement of interest and present hemodynamic conditions.

1.4 PC-MRI measurement integrated CFD simulation based data assimilation (DA) method

The integration between PC-MRI and CFD simulation has been shown in [17]-[20], and the details explanation about the blood movement inside intracranial aneurysms were introduced. By [20], [21] shows the good understanding on hemodynamic studies in the prediction of the flow field problems through internal carotid arteries. However, little information is available in the literature about the accuracy of the approach and quantitative differences between PC-MRI measurement and CFD simulation, especially on configuration [21] and boundary condition. The authors of [22], [23] did the same observation but practically focus on carotid bifurcation arteries (CBA).

Integration analyses coupling the numerical simulation with PC-MRI measurements have been attempted, using techniques from control theory [24] and data assimilation (DA) [25]. Ultrasonic-measurement-integrated (UMI) simulations [26] were also carried out, where a body force derived from differences in the velocity fields between the ultrasonic measurement and simulation is incorporated into the momentum equation based on feedback control theory. These UMI simulations were first applied for a two-dimensional model [24], then extended to a three-dimensional model [26] for blood flow in an aorta with an aneurysm. Although the UMI simulations have been widely applied for practical blood flow problems, it is questionable whether the body force is physically correct; in addition, a modification technique is required to obtain a consistent pressure field. A data assimilation (DA) technique was used for integration analysis based on a variational method (or 3D adjoint method) [25] or Bayesian inference [27]. In the variational method, a cost function related to the velocity difference between the measurement and simulation is minimized by the least-squares method with respect to boundary conditions such as the stress vectors on the inlet/outlet boundary, where

the governing equations are used as constraints. Thus, it becomes an inverse problem to obtain the boundary conditions, minimizing the cost function. The resulting velocity field is physically consistent because the boundary condition is estimated. However, because the problem is *ill-posed*, a Tikhonov regularization term is added to the system with an arbitrary parameter; this creates a huge discrete system that is time-consuming and expensive to solve.

1.5 Motivation and aim of the thesis

The main motivation of this thesis is to develop a new concept of data assimilation method for reproducing an exact flow field by reducing the velocity difference between PC-MRI measurement and CFD simulation with using all the PC-MRI velocity data for patient-specific cerebral aneurysm. Currently, the clinical assessment of the cerebral aneurysm mainly focuses on the anatomical features of the patients observed by the medical imaging techniques. However, the data assimilation (DA) method has been extensively developed to investigate the patient-specific blood flow and hemodynamics factor on cerebral aneurysms by combining the measurement and simulation. Thus, the quantitative evaluation of blood flow field considering the real patient-specific geometry is strongly dependent on vessel configuration and boundary condition setup.

The aim of this thesis is to conduct a computational approach based data assimilation method. We want to obtain an exact flow field by reducing the velocity differences between CFD simulation and PC-MRI measurement (with noise). In the first part of this thesis, the effects of extracted patient-specific geometries with difference threshold image intensities on flow solution were investigated by using CFD studies. Next, the study was focused to propose a basic framework for imposing a pressure condition on the outlet boundary using velocity-field optimized (V-optimized) approach, in order to minimize the velocity differences between

PC-MRI measurement and CFD simulation. Finally, the feasibility study on a novel data assimilation method for patient-specific blood flow analysis based on conventional feedback control theory called the *physically consistent feedback control-based data assimilation* (PFC-DA) method was investigated.

1.6 Outline of the thesis

Chapter 2 describes the CFD studies to investigate the effect of extracted patient-specific geometries with a different coefficient of threshold image intensities on flow solution. Chapter 3 focuses on proposing a basic framework for imposing a pressure condition on the outlet boundary to minimize the velocity differences between PC-MRI measurement and CFD simulation where we compare three different CFD approaches namely, pressure fixed (P-fixed) approach, flow-rate control (Q-control) approach and velocity-field optimized (V-optimized) approach. Chapter 4 presents a feasibility study on a novel *physically consistent feedback control-based data assimilation* (PFC-DA) method for patient-specific blood flow analysis. Chapter 5 concludes the thesis by summarizing the major findings and describes the future work.

Chapter 2

Influence of extracted geometries on velocity difference between PC-MRI measurement and CFD simulation for patient-specific blood flow fields

2.1 Introduction

Early studies investigated hemodynamics in idealized arterial geometries; the current trend is to use the realistic patient-specific geometry of vivo arteries. It is required to implement realistic geometrical models on individual basis, since individual configurations is the rule rather than the exception, and blood flow characteristics strongly depend on vessel configuration [28], [34].

Computational fluid dynamics (CFD) study would be a powerful tool to investigate the blood flow characteristics for a patient-specific aneurysm. In previous studies [29], [30], validation of CFD simulation is extremely important to solve the flow field in hemodynamic problems. Conversely, a combined PC-MRI measurement and CFD simulation introduced the good understanding on hemodynamic studies in the prediction of the flow field problems through internal carotid arteries. However, little information is available in the literature about the accuracy of the approach and quantitative differences between PC-MRI measurement and CFD simulation, especially on the configuration of vessel geometry [21], [31]. As for the blood flow simulation in a cerebral aneurysm, the computational result depends on the vessel configuration, and that simplification of the geometry may possibly observe the effect on flow field [32]. Since we assumed that the blood vessel configuration was accurately reconstructed, the effect of deviance on blood vessel geometry from real one remains to be investigated.

In recent years, remarkable progress has been made in simulating blood flow constructed between computational simulation and medical imaging measurement. It had reported that when the blood vessel configuration close to the upstream, boundary condition was moderate, and the application of idealized velocity profile was valid [33]. Therefore, in this chapter, it is importance to investigate the effect of reconstructed geometries on velocity difference between PC-MRI measurements and CFD simulation.

The aim of this chapter was to investigate the effects of extracted patient-specific geometries with difference threshold coefficient (C_{thres}) and estimate the velocity difference of the blood flow field in PC-MRI measurement and CFD simulation with using the CFD studies.

2.2 Methodology

2.2.1 Clinical data

There are ten patient-specific aneurysms with different sexes acquired from clinical digital subtraction angiology (DSA) at Osaka University hospital. These ten patients underwent open surgery between August 2010 and October 2012. Table 2.1 shows the clinical characteristics of the side-location, gender, number of outlet branches and diameter of aneurysm size. The measurement of aneurysm diameter was conducted, and the medical images used for surface reconstruction were obtained using 3D rotational angiography (3D-RA). The 512 corresponding projection images were reconstructed into a 3D data set of 512 x 512 x 512 voxels with a resolution from 0.1 to 0.17 mm.

Table 2.1 Clinical characteristics.

Patient	Side	Sex	Outlet branch	Location	Aneurysm diameter (mm)
1	Right	M	3	ICA	2.81 - 3.52
2	-	M	3	ACA	1.81 - 2.39
3	Left	M	3	MCA	5.68 - 6.52
4	-	F	3	BA	4.35 - 5.13
5	Left	M	3	ICA	7.91 - 6.80
6	Left	M	3	MCA	6.05 - 6.65
7	Left	M	3	ICA	8.12 - 9.13
8	-	F	2	ACA	1.92 - 2.61
9	-	M	2	ACA	4.52 - 5.32
10	-	M	2	BA	3.86 - 4.60

M: Male. F: Female. ICA: Internal carotid artery. ACA: Anterior cerebral artery. MCA: Middle cerebral artery. BA: Basilar artery. The aneurysm diameter is measured in the vascular model reconstructed by threshold coefficient value of 0.3.

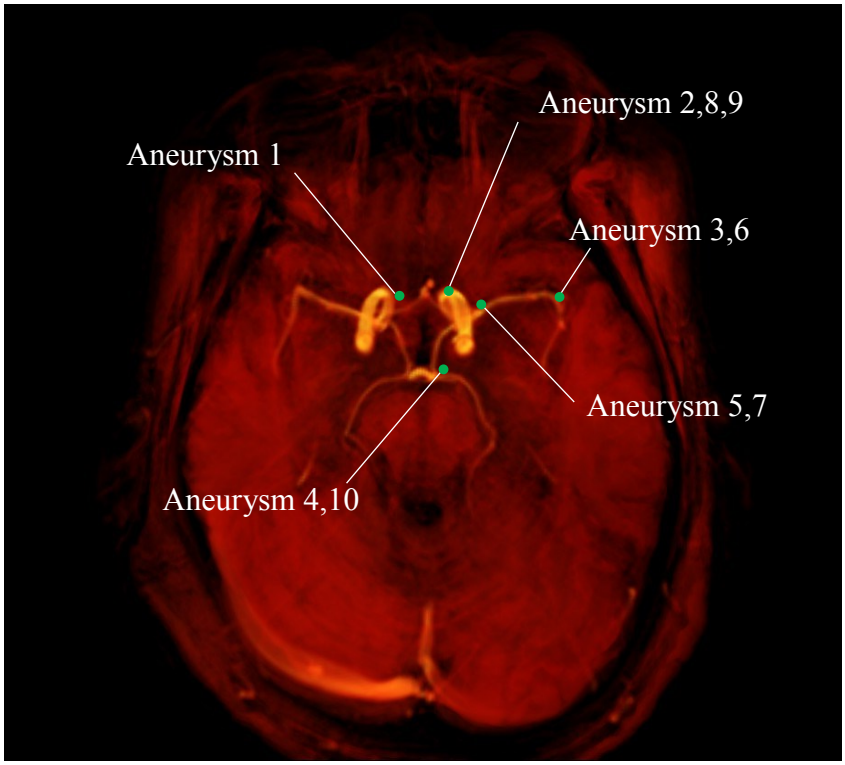

Fig 2.1. The location of aneurysms 1-10 in the typical cerebral vasculature. Note, the image is generated from Phase contrast-MRI using AMIRA^{TM} 5.4.2 software.

2.2.2 Image segmentation using a determination threshold coefficient method

The medical imaging data were acquired from ten different patients featuring two or three branches of internal carotid artery (ICA). The image segmentation and surface reconstruction of the vessel were performed from DSA images in AMIRA 5.4.2 (Visage Imaging, Berlin, Germany). The threshold coefficient method [34] was introduced to extract the vessel geometry adequately. We selected a representative cross-section, where the blood vessel was distinct with a large diameter, and set a straight line in the cross-section across the blood vessel shown in Fig. 2.2(a). Then, the minimal and maximal values of the image intensity along the line, $I_{\min}$ and $I_{\max}$, were obtained and calculated the threshold image intensity, I_{thres}, by using a threshold coefficient defined as:

$$C_{thres} = \left(\frac{I_{thres} - I_{\min}}{I_{\max} - I_{\min}} \right) \tag{2.1}$$

In this investigation, five different threshold coefficients (C_{thres} = 0.2, 0.3, 0.4, 0.5, and 0.6) values were employed as shown in Fig. 2.2(b). Consequently, 50 segmented vascular models were created in total for ten patients.

The 3D reconstruction of the cerebral aneurysm geometry was done using AMIRA 5.4.2. The cerebral aneurysm surface was given by 3D triangle meshes based on the unconstrained smoothing function of AMIRA 5.4.2 (see Fig. 2.3(a)). To reduce the remains of spatial irregularity of the obtained surface meshes, a physical-based surface (spring network model) smoothing process was carried out (see Fig. 2.3(b)), which the stretching and bending were applied to each edge of the mesh and pair of the adjacent meshes, respectively. Details are described in Appendix 1.

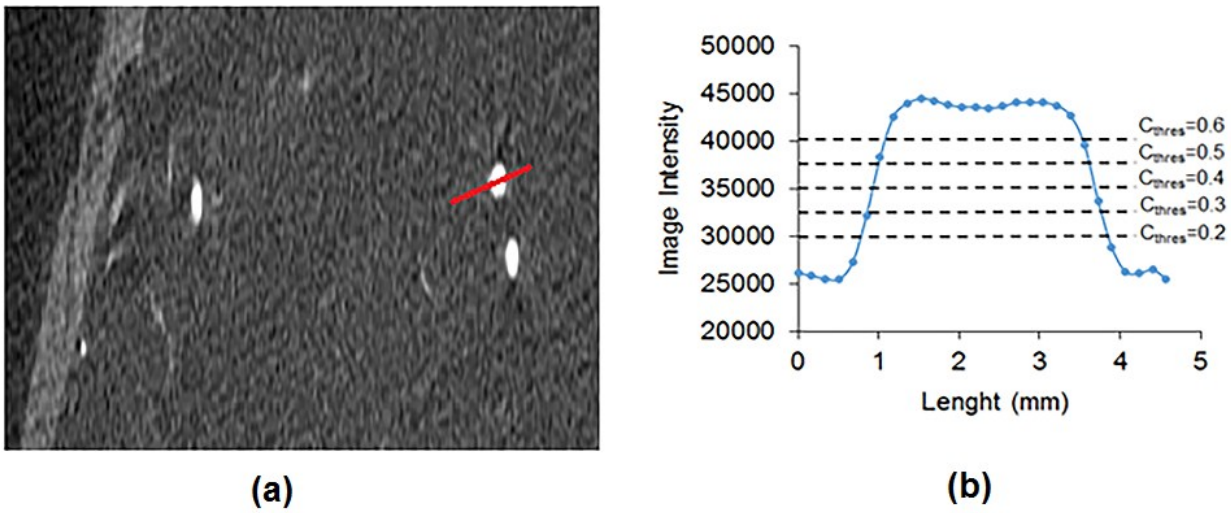

Fig. 2.2 Schematic of the threshold coefficient method of vascular reconstruction. **(a)** DSA image. A red line is set as an axis of the evaluation. (b) Image intensity profile along the evaluation axis in (a) and the respective threshold levels defined in (2.1).

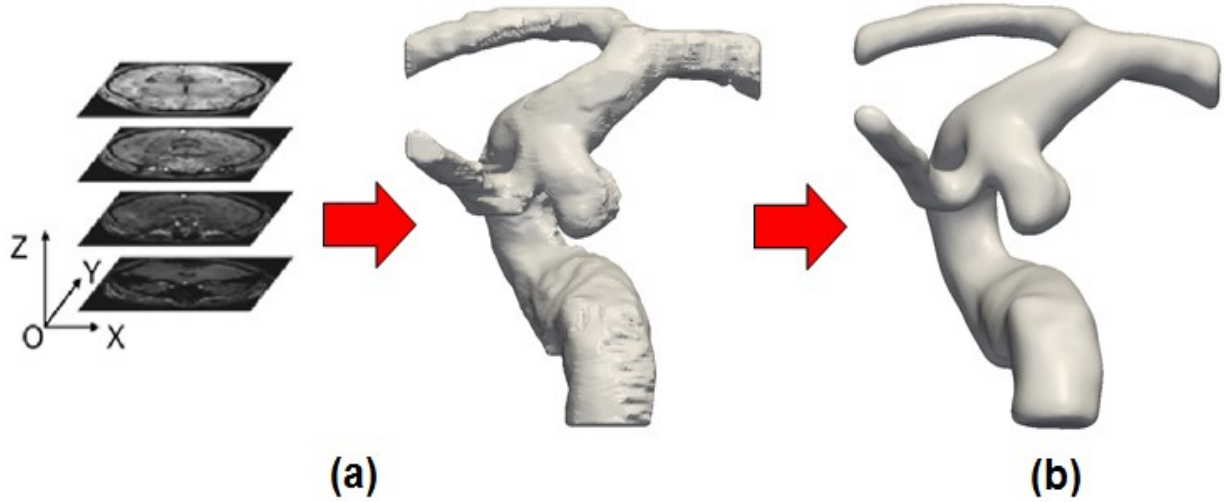

Fig. 2.3 Process of the construction of the cerebral aneurysms geometry from clinical DSA images. (a) The patient-specific geometry of the aneurysm is extracted using AMIRA 5.4.2 from medical DSA images, and surface meshes are constructed. (b) The surface smoothing is done by the physics-based surface smoothing process using a spring network model.

2.2.3 PC-MRI acquisition

The PC-MRI examinations were performed on a 3.0T MRI scanner (Philips Achieva TX) using a standard head coil. 4D-flow provides us with time-resolved 3D voxel data, each of which has three-directional flow velocity components. A gradient echo phase contrast imaging sequence was applied using retrospective cardiac gating using peripheral pulse unit, resulting in 15 frames/phases over the cardiac cycle. The imaging parameters for 4D-flow were as follows; echo time (TE) 3.8 ms, repetition time (TR) 8.1 ms, 15^0 flip angle (FA), 1 mm slice thickness, 250 x 180 mm field of view (FOV), scan matrix 256 x 192 pixels, voxel size 0.7 x 0.7 x 0.5 mm, 56 number of slices and a velocity sensitivity (*VENC*) of 120 cm/s. 3D time-of-flight (TOF) MR angiography was performed for geometric information. Imaging parameters for 3D TOF MR Angiography were as follows; TR/TE 22/3.5 ms, FA 220, FOV 200 mm, matrix 293 x 512, and 0.7mm slice of thickness.

2.2.4 Velocity field obtain from PC-MRI measurement

In PC-MRI image, the vascular region was extracted using the range of the intensity value where the surrounding tissue of the blood vessel is not selected as much as possible in measurement data. The intensity value of the blood vessel region is set to 1, and for the non-blood vessel, the region is set to 0. A 3D velocity field was obtained from the voxel intensity value in each of the three phase images corresponding to each voxel of the vessel region extracted from the PC-MRI image. As shown in Fig. 2.4(a), coordinate axis is taken with the pixel in the lower left corner as the reference point. The values of i and j represent pixel positions on the image, expressed as integers from 1 to the number of pixels, and the value of k represents the slice position of the image and is represented by an integer from 1 to the

number of slices (2.2). The measurement result is recorded on the phase image with 12 bits (4096 gradations).

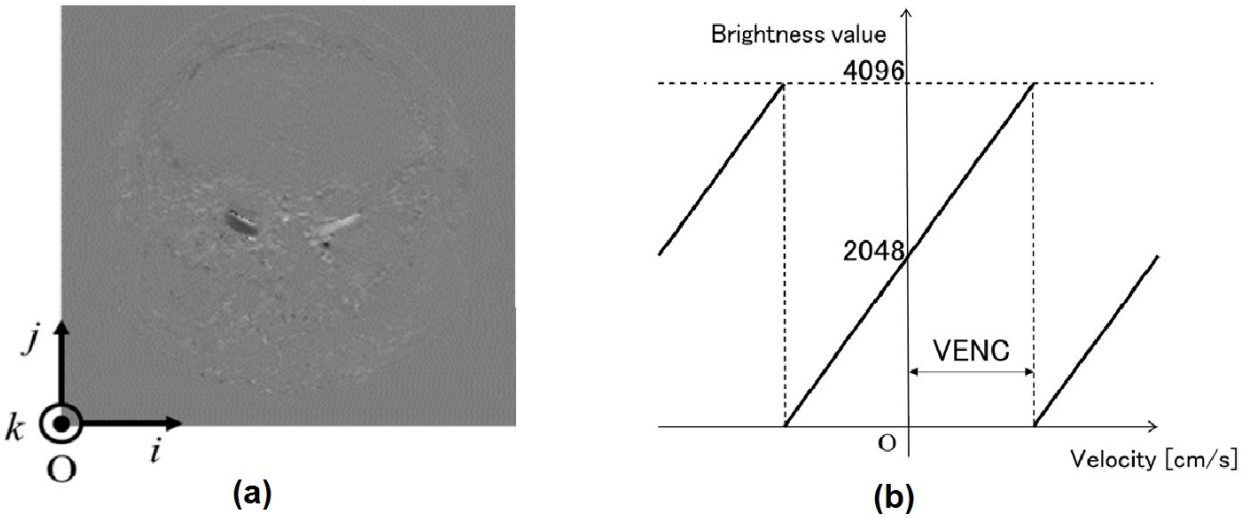

Fig. 2.4 (a) Coordinate axes in a plane. (b) The relationship between the brightness values and the velocity.

The relationship between intensity value and speed is shown in Fig. 2.4(b). At this time, *VENC* is the absolute value of the speed measurement range at the time of phase image, and the intensity value and the speed are in a linear relation (2.3).

$$v(i,j,\mathrm{k}) = \begin{bmatrix} v_x(i,j,\mathrm{k}) \\ v_y(i,j,\mathrm{k}) \\ v_z(i,j,\mathrm{k}) \end{bmatrix} \tag{2.2}$$

$$v_n(i,j,\mathrm{k}) = \frac{VENC\left(p_n(i,j,\mathrm{k}) - 2048\right)}{2048} \quad (n = x,y,z) \tag{2.3}$$

However, as shows in Fig. 2.4(b), the speed value outside the range of *VENC* is the folded value. This is called folding artefact. A velocity vector in each voxel constituting the cerebral blood vessel region extracted from the PC-MRI image was calculated from three phase images to generate a three-dimensional velocity field. Table 2.2 shows the spatial average inlet velocity obtained from PC-MRI measurement images at peak systole, and corresponding Reynolds

numbers are shown based on the inlet vessel diameter and typical kinematic viscosity of the blood.

Normally, the aneurysm geometry obtained from PC-MRI was presented in voxels (see Fig. 2.5(a)) and for the three-dimensional velocity field acquired from the PC-MRI measurement as shown in Fig. 2.5(b). Both images were visualized by ParaView (Kitware Inc.).

In order to investigate the velocity differences between PC-MRI measurement and CFD simulation, it is necessary to register the cerebral aneurysm shape model with the shape obtained from the PC-MRI image. Therefore, these two model are possible to register by coordinate transformation using an Iterative Closest Point (ICP) algorithm [35] where is widely used as a basic method of alignment between two 3D models. Details are described in Appendix 2.

Table 2.2 Average inlet velocity and corresponding Reynolds number obtained from PC-MRI data at peak systole.

	Patient 1	**Patient 2**	**Patient 3**	**Patient 4**	**Patient 5**	**Patient 6**	**Patient 7**	**Patient 8**	**Patient 9**	**Patient 10**
Inlet velocity (m/s)	0.212	0.601	0.294	0.729	0.201	0.335	0.307	0.731	0.463	0.455
Reynolds number	142	427	435	558	230	213	201	475	523	148

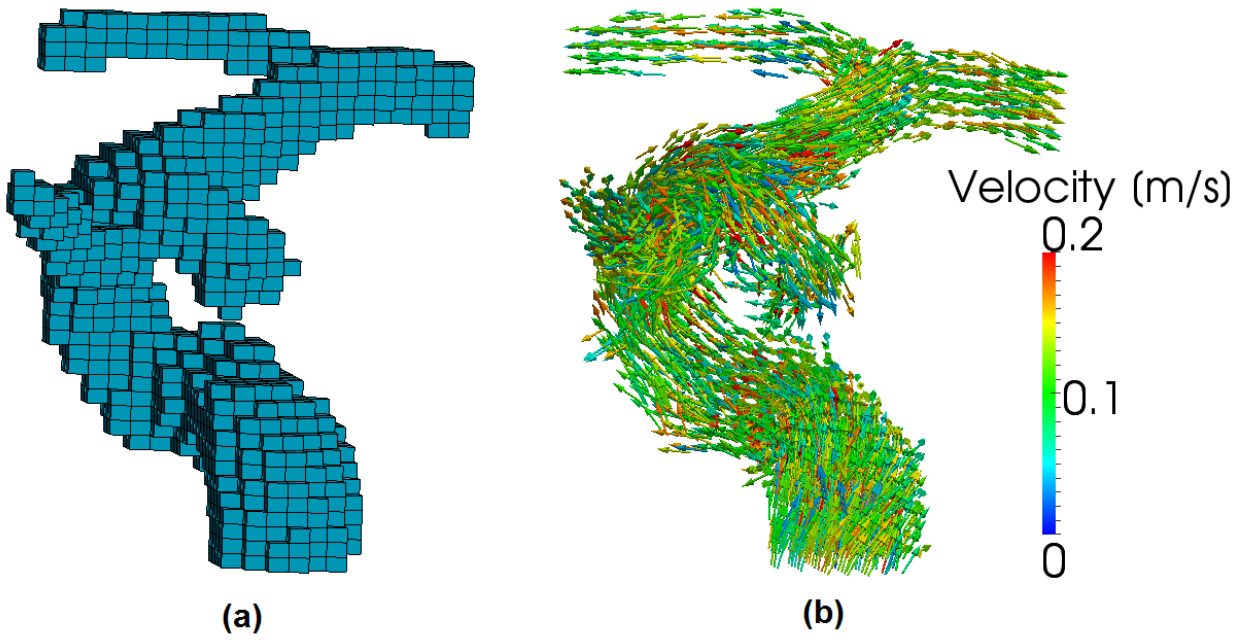

Fig. 2.5 a cerebral aneurysm obtained from PC-MRI intensity image in patient 1. (a) Reconstruction of vascular geometry presented by voxel. (b) Typical velocity fields in a cerebral aneurysm obtained from PC-MRI measurement.

2.2.5 Blood flow analysis

Generation of the computational mesh for the blood flow analysis was done using the commercial software STAR-CCM+ 6.04.014 (CD-Adapco, Yokohama, Japan). Five prism layer meshes with a 10% wrapper scale were set in the vicinity of the wall, and polyhedral meshes were adopted for the rest of the flow region. The parameters for meshing were determined so that the base size of the mesh is 0.6 mm (meshes above 10% of base size are allowable). The total number of meshes as shows in Table 2.3. Since the Reynolds number of the blood flow in the cerebral artery ranges from 142 to 558 (see Table 2.2), the flow is assumed as laminar flow. The aneurysms region was defined by the volume mesh separation of arterial geometries as shown in Fig. 2.6 by the function of STAR-CCM+.

Table 2.3 Number of meshes for each patient.

Patient No.	Number of elements
1	383189
2	147968
3	485528
4	250411
5	488850
6	409488
7	566241
8	276357
9	200107
10	156343

Blood was assumed to be an incompressible Newtonian fluid because the non-Newtonian nature of blood only generates secondary effects on blood flow as compared with the geometry of the flow region [36]. Although flow in the cerebral artery is normally unsteady with a Womersley number of 3, steady flow was assumed for simplicity [37]. For the present simulation, the flow was modeled with the Navier-Stokes equation and the equation of continuity, given by

$$\rho(\mathbf{u}\cdot\nabla)\mathbf{u} = -\nabla p + \mu\nabla^2\mathbf{u}, \tag{2.4}$$

$$\nabla\cdot\mathbf{u} = 0, \tag{2.5}$$

where $\mathbf{u}$ is the velocity vector of the flow, p is the pressure, ρ the density, and the μ viscosity of the fluid. The simulation condition was set as follows. Blood was treated as a specific density of ρ = 1050 kg/m^3, and viscosity $\mu = 3.5 \times 10^{-3}$ Pa.s. Arterial walls were assumed to be rigid, and a no-slip condition, $\mathbf{u} = 0$ was applied. On the inlet boundary Γ_{in}, the uniform velocity was imposed shown in Table 2.2 and a zero gradient condition for the pressure. On the outlet boundary Γ_{out}, a zero gradient condition for the velocity was imposed and a Dirichlet boundary condition for the pressure, set at an arbitrary value.

Generally, for incompressible fluid analysis involving the multiple outlets, when the inlet velocity is fixed, the outlet pressures should also be fixed. However, in blood flow analysis, a part of the general circulation is extracted and addressed, and thus the outlet pressures are not deterministically obtained. In order to investigate the effects of extracted geometry on velocity difference between PC-MRI measurement and CFD simulation on the patient-specific aneurysm, two different approaches to determine the outlet boundary condition were introduced, called the pressure-fixed (*P*-fixed) approach and flow-rate control (*Q*-control) approach.

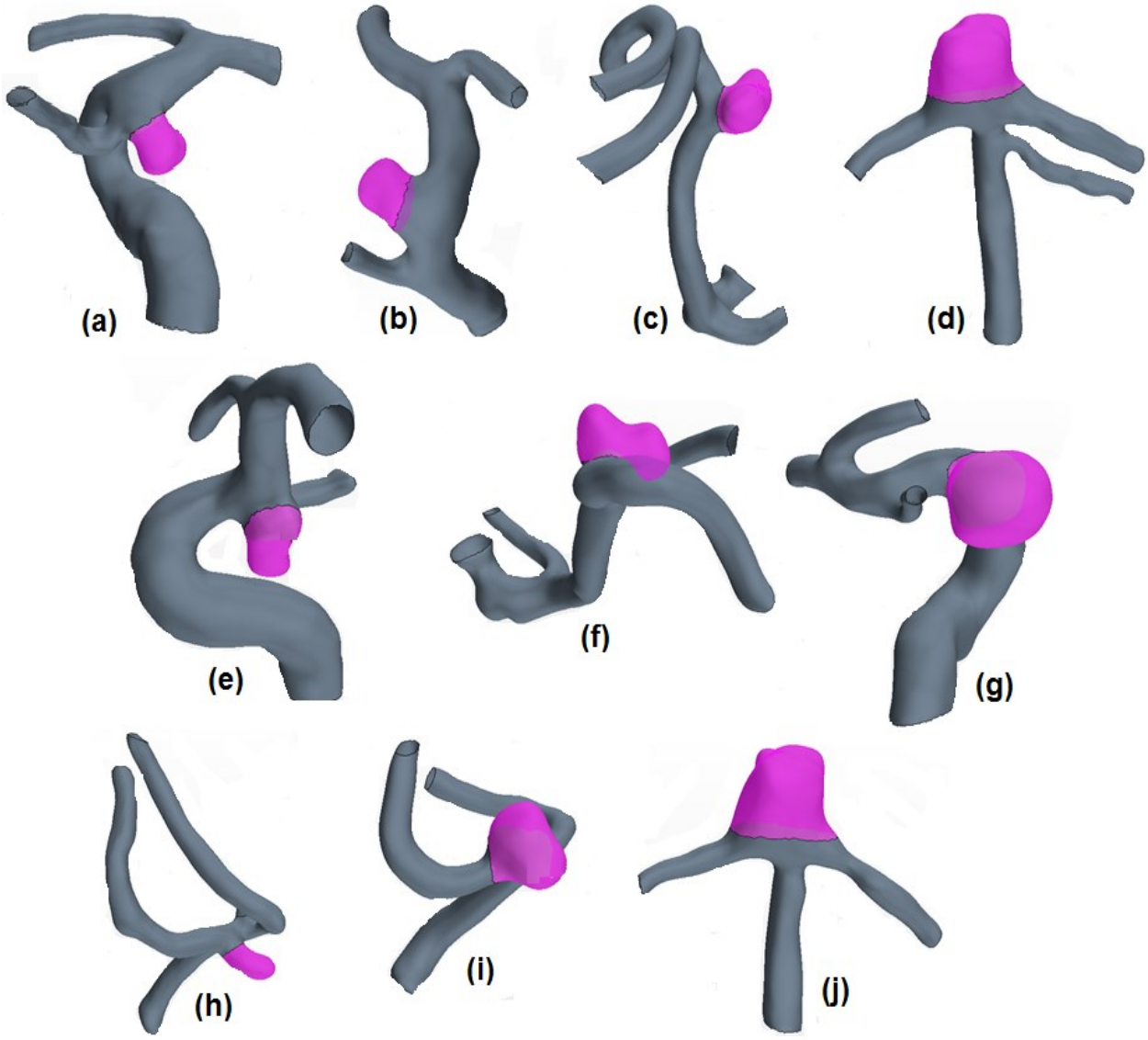

Fig. 2.6 Configuration of patient-specific aneurysms recontracted from clinical DSA images acquired at Department of Radiology, Osaka University Hospital. Regions with red and grey colors indicate the aneurysm region and non-aneurysms region respectively.

2.2.5.1 Pressure-fixed (*P*-fixed) approach

The basic framework with *Ad-hoc* pressure fixed (*P*-fixed) approach was presented. The outlet $i \in [1,I]$ was defined, where I is the total number of outlets, and corresponding outlet pressures $p^{(i)}$. In the *P*-fixed approach, all the outlet pressures was set to zero, i.e., $p^{(i)} = 0$ for $i \in [1,I]$.

2.2.5.2 Flow-rate control (*Q*-control) approach

Although pressure is generally used as outlet boundary condition in CFD analysis [9], it is difficult to acquire the pressure inside a blood vessel by measurement setting when there are multiple outlet boundaries. Therefore, the value of the pressure was proportionally controlled so as to coincide with the flow distribution ratio calculated from the PC-MRI image at a plurality of outlet boundaries.

By [38], the outlet flow rates control (*Q*-control) approach was introduced for the PC-MRI measurement and CFD as $Q^{(i)}$ and $q^{(i)}$ respectively, for the outlets $i \in [1,I]$. In the *Q*-control approach, the outlet pressure $p^{(i)}$ is modified by the flow rate difference $Q^{(i)} - q^{(i)}$, based on the proportional feedback control as follows.

$$ {}^{k+1}p^{(i)} = {}^{k}p^{(i)} + G({Q}^{(i)} - {}^{k}q^{(i)}), \qquad \text{for } i \in [2,I] \tag{2.6} $$

Here, the superscript k represents the iteration number in solving the time-dependent Navier-Stokes equations (2.4), (2.5) or feedback loop, and ${}^{k}p^{(i)}$ and ${}^{k}q^{(i)}$ are the outlet pressure and flow rate for the k-th iteration in the CFD analysis, respectively. The second-term in (2.6) represents the pressure increment modifying the outlet pressure at the next feedback loop k+1. In terms of the feedback control theory, it is interpreted that the PC-MRI flow rate $Q^{(i)}$ is the desired value, the CFD flow rate ${}^{k}q^{(i)}$ is the output, their difference $Q^{(i)} - {}^{k}q^{(i)}$ is the deviation, and the pressure increment of the second-term in (2.6) is the control variable. Here, G is the

dimensional proportional gain, which associates the flow rate difference between the CFD and PC-MRI with the outlet pressure (increment). In this study, instead of using the dimensional gain G, we employed a non-dimensional gain G^* to relax a problem dependency by introducing an inlet dynamic pressure ρU_{in}^2 and inlet flow rate Q_{in} so that $G = (\rho U_{in}^2/Q_{in})G^*$. We fix the pressure at outlet 1 to 0, i.e., $p^{(1)} = 0$ for all iterations, because, in incompressible flow simulation, the relative pressure works with the velocity inlet boundary condition.

It should be noted that the non-dimensional gain G^* behaves like a spring constant in the system and still depends on the analysis condition. In the feedback loop, a convergence speed becomes faster as G^* is increased. However, the system becomes oscillatory and unstable as G^* is much increased. Since its threshold is explored by trial and error, we had found the solutions are stable and reasonably accurate at $G^*=15$ from our preliminary numerical trials. Thus, we employed it for all our analyses by the Q-control approach. The flowchart of the Q-control approach is shown in the Fig. 2.7.

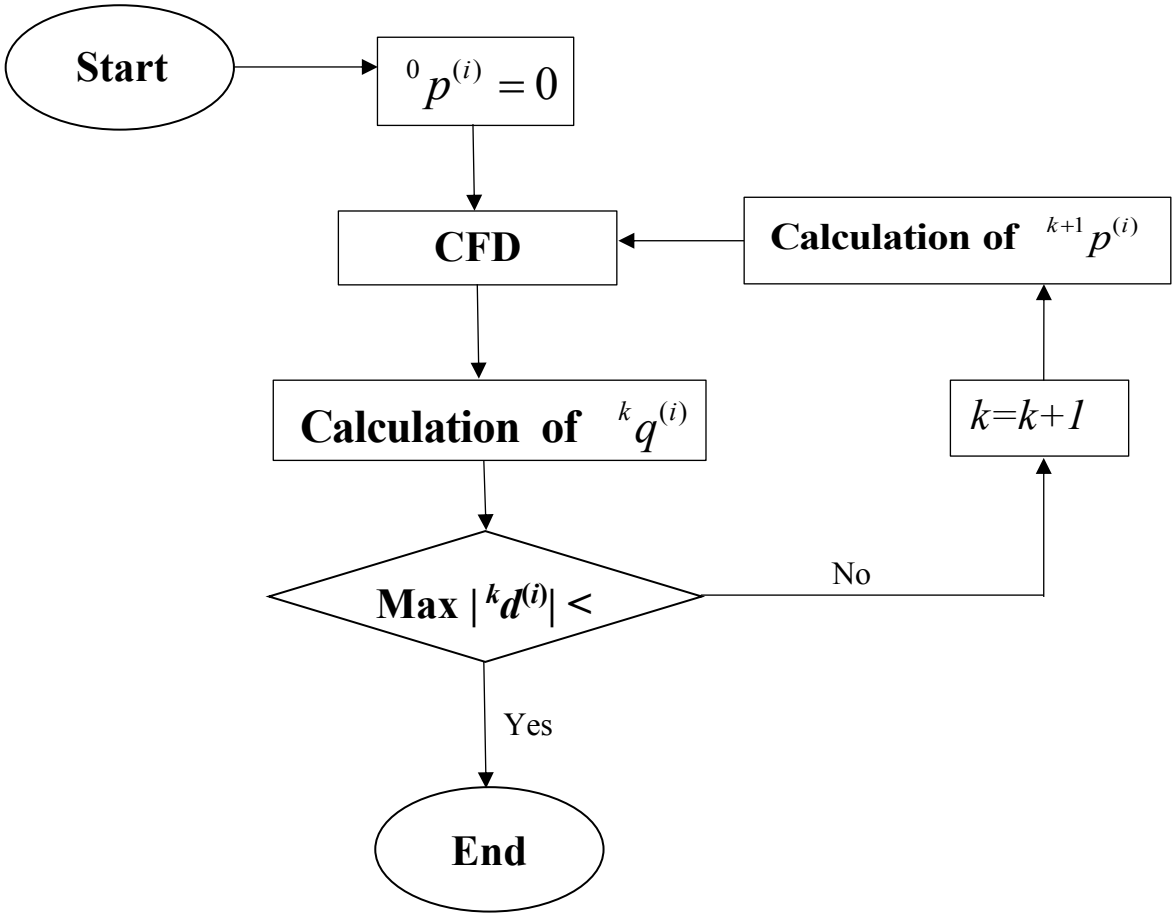

Fig. 2.7 Flowchart of algorithm in the *Q*-control approach.

2.2.6 Evaluation of the velocity difference

In order to compare the velocity difference between measurements and computations, the velocity field of CFD analysis is interpolated to the voxel-based data obtained from the low resolution of PC-MRI measurement. By combining Gaussian quadrature method and moving least squares approximation method, the average value in voxels from discrete element velocity vectors in CFD analysis was approximated. We calculated the discrete velocity difference as:

$$\mathbf{U}_m - \mathbf{u}_m \quad \text{for} \quad m \in [1, M] \tag{2.7}$$

where M is the total number of voxels or measurement points of the PC-MRI, and $\mathbf{U}_m$ and $\mathbf{u}_m$ are the m-th measurement and numerical velocities, respectively, at the measurement point $\mathbf{x}_m$. Note that the measurement velocity using the PC-MRI is not regarded as a pointwise value because of the relatively low resolution compared to the vessel size. The velocity value obtained from the PC-MRI was spatially averaged in each voxel of the PC-MRI, and thus the projection procedure was introduced to associate the CFD solutions with the PC-MRI measurements for the evaluation of velocity difference. The detailed procedure for evaluation of velocity difference was described in Appendix 3 and Fig. 2.8 shows the evaluation domain in all ten patients.

For the evaluation, the velocity difference norm, Eu has introduced as:

$$\mathrm{E_u} = \frac{1}{M}\sum_{m=1}^{M}\left|\mathbf{U}_m - \mathbf{u}_m\right| \tag{2.8}$$

In addition, the normalized norm is defined as

$$\mathrm{E_u^*} = \frac{\mathrm{E_u}}{U_{\mathrm{in}}} \tag{2.9}$$

where U_{in} is the inlet velocity shown in Table 2.2.

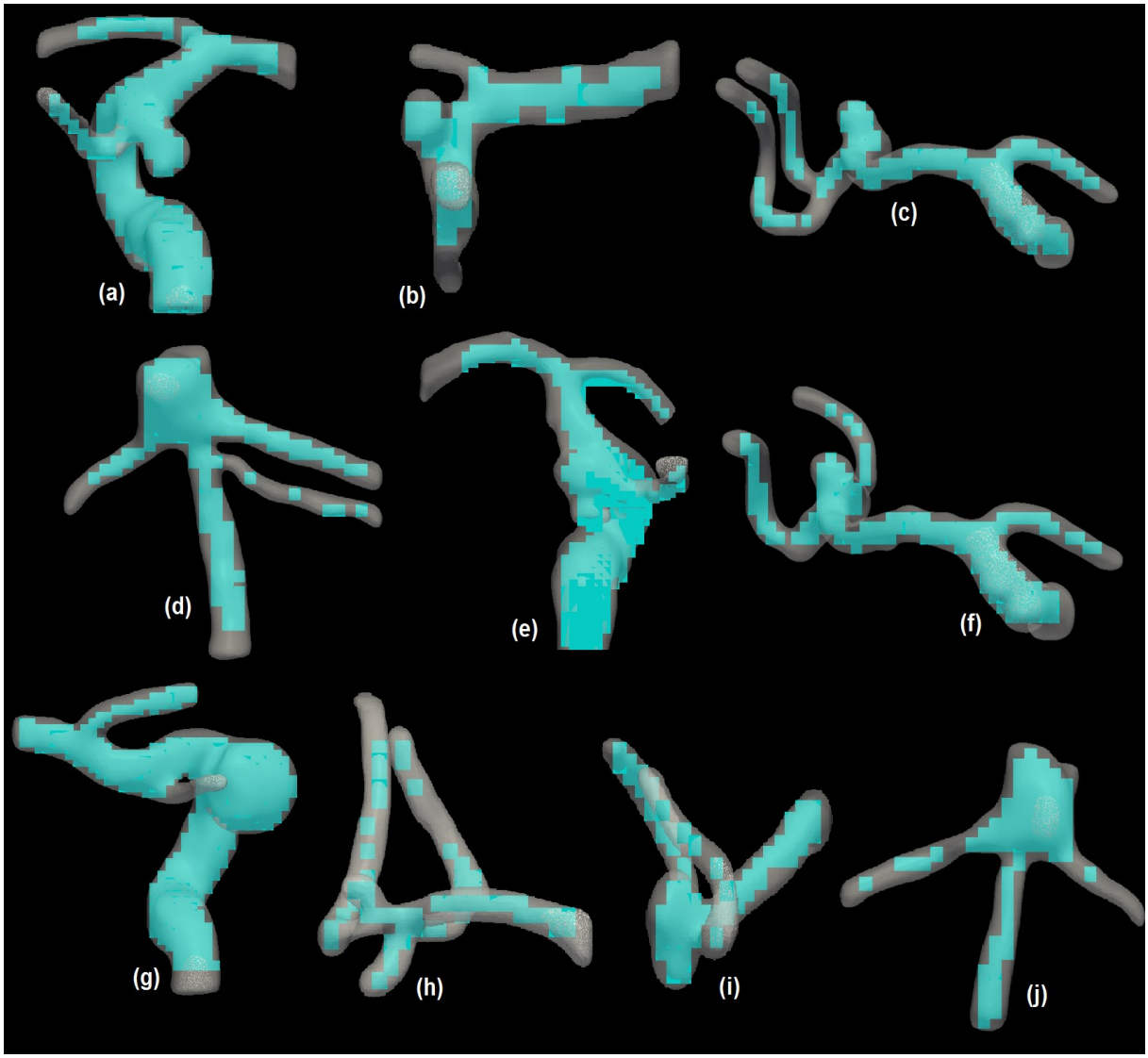

Fig. 2.8 Evaluation domain in all ten patients. (a) Patient 1, (b) Patient 2, (c) Patient 3, (d) Patient 4, (e) Patient 5, (f) Patient 6, (g) Patient 7, (h) Patient 8, (i) Patient 9 and (j) Patient 10.

2.3 Results and discussion

About fifty of cerebral aneurysm models were created base on five different C_{thres} values. In the determination of threshold image intensity, we obtained the highest and lowest values were (8572-11261) and (-4119-2698) respectively. The threshold image intensity value calculated to C_{thres} values of 0.2, 0.3, 0.4, 0.5 and 0.6 were (528-2109), (1125-1864), (1724-2659), (2322-3639) and (2839-4618) respectively.

2.3.1 Effect of C_{thres} on configuration of vascular models

The effect of extracted geometry in a patient-specific aneurysm was investigated using CFD studies. Fig. 2.9 shows the inlet area and volume of vascular models decreased as the C_{thres} value was increased. In the volume results, the C_{thres} value of 0.5 was significantly smaller than those obtained from C_{thres} values of 0.2 and 0.3 ($p < 0.001$) respectively and those, in the inlet area results, the C_{thres} value of 0.3 was significantly larger than those obtained from C_{thres} values of 0.5 and 0.6 ($p < 0.001$) respectively. The configuration of the vascular model gives the high impact on intra-aneurysmal hemodynamics and potentially useful in predicting the aneurysm rupture [39]. Early studies investigated hemodynamics and blood flow characteristics strongly depend on vessel configuration [28]. Therefore, the extracted geometry of these parts must be accurately [40], [41]. The incidence of disconnection artery (see Fig. 2.10) or the creation of holes in the vascular vessel increases when the threshold image intensity becomes higher. This disconnection of artery especially large branches associated with the aneurysm cannot be negligible because it may have a major effect on cerebral aneurysm hemodynamics. Thus, the effect of C_{thres} was evident from the fact that the blood flow characteristic strongly depends on vessel configuration and all the subsequent results were obtained at C_{thres}=0.3.

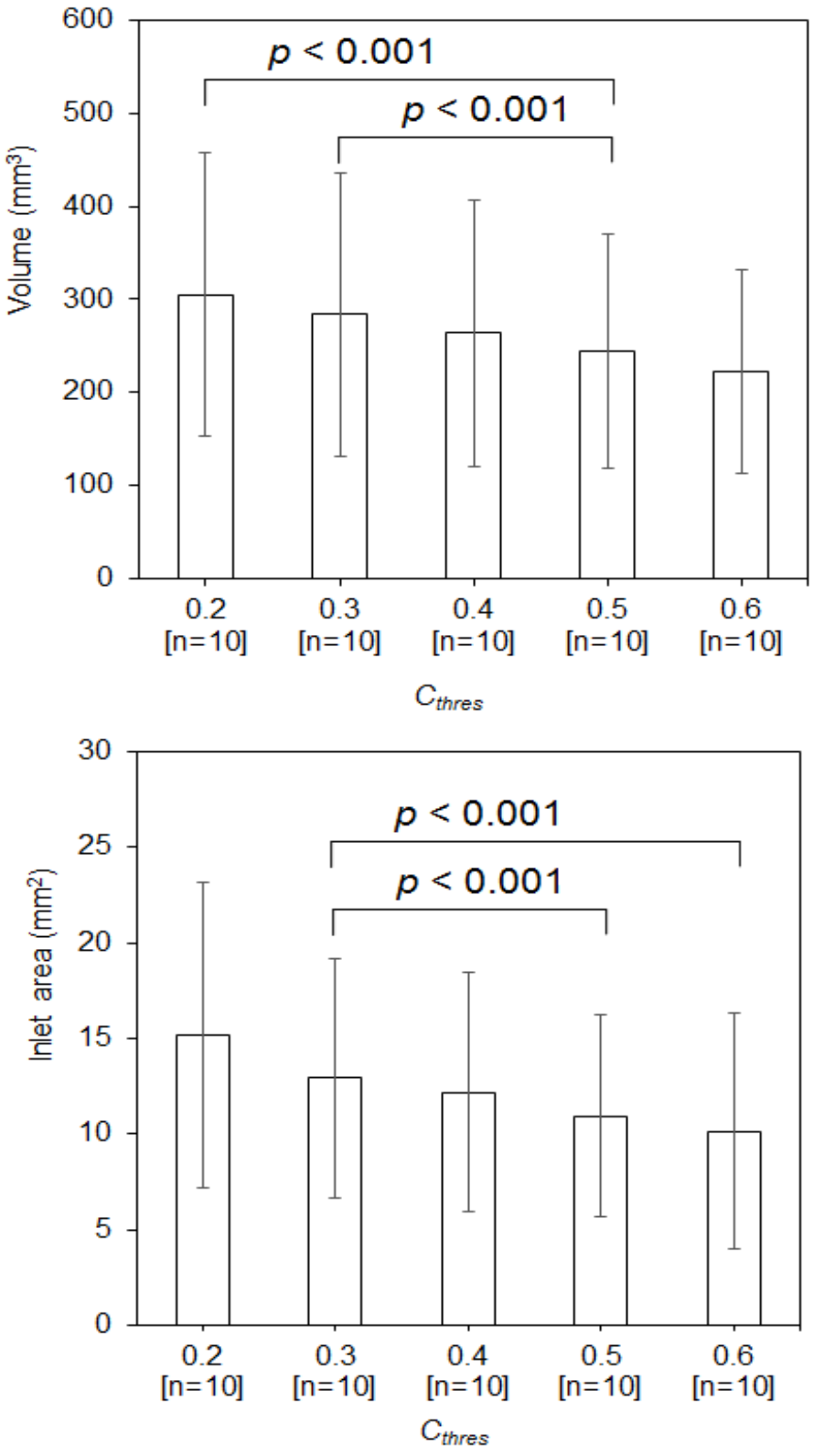

Fig. 2.9 Effect of threshold coefficient (C_{thres}) values on vascular model configuration. The comparison between five different C_{thres} values for the volume (*top)* and inlet area (*bottom*) of the vascular model respectively. These values decrease as the C_{thres} values increase.

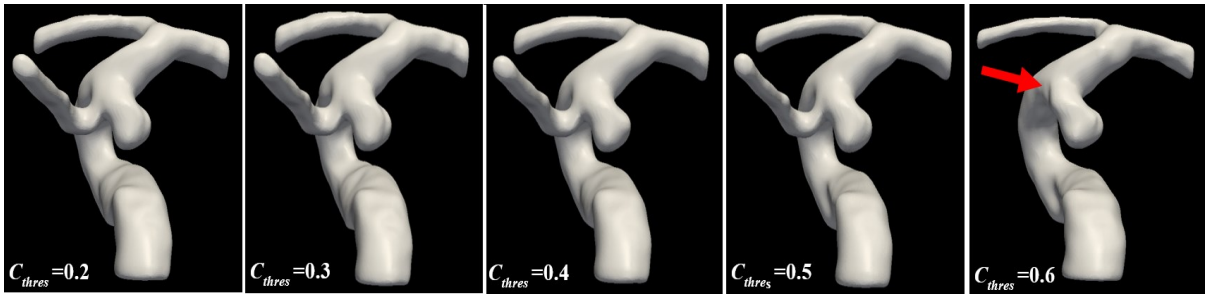

Fig. 2.10 Representative vascular models reconstructed from patient 1 using five threshold coefficient (C_{thres}). The posterior connecting artery was removed at C_{thres} 0.6 (red arrow) because of the disconnection artery during extracted geometry process.

2.3.2 Effect of C_{thres} on WSS of vascular models

The highest WSS region was located at the neck area in all 10 patient-specific aneurysms and the Fig. 2.11 shows, the value of WSS distribution increased when the C_{thres} value increased. The average WSS distribution of the entire vascular model with a C_{thres} value of 0.2 was significantly lower than those obtained with C_{thres} values of 0.5 and 0.6 ($p < 0.001$) respectively. However, the C_{thres} value of 0.5 was significantly higher than those obtained with C_{thres} values of 0.2 and 0.3 ($p < 0.001$ and $p < 0.01$) respectively. The highest WSS distribution was observed at the neck area and the lowest WSS distribution detected at the body/dome area of the vascular model. The remarkably changed WSS distribution was obtained when the C_{thres} value increased especially at C_{thres} values of 0.5 and 0.6 as shown in Fig. 2.12.

Addition, we observed the WSS distribution was considerably changed due to volume change. Fig. 2.13 shows a negative non-linear correlation between volume and the average of WSS distribution. Therefore, the extracted geometry based on threshold determination method should be performed carefully especially for vascular models with small volumes in order to neglect the extreme changes in the WSS distribution of the patient-specific geometry.

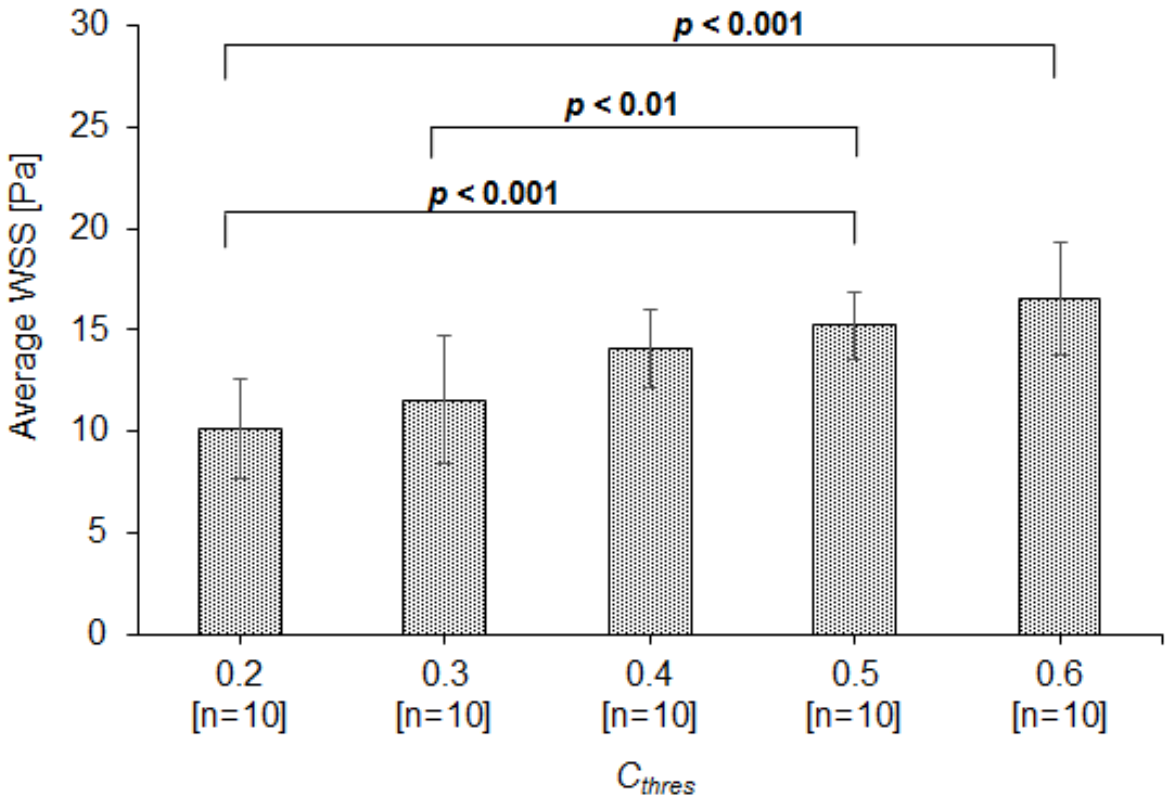

Fig. 2.11 Effect of threshold coefficient (C_{thres}) values differences on wall shear stress (WSS) distribution of a vascular model. The WSS distribution at the highest region increases when the C_{thres} values increase.

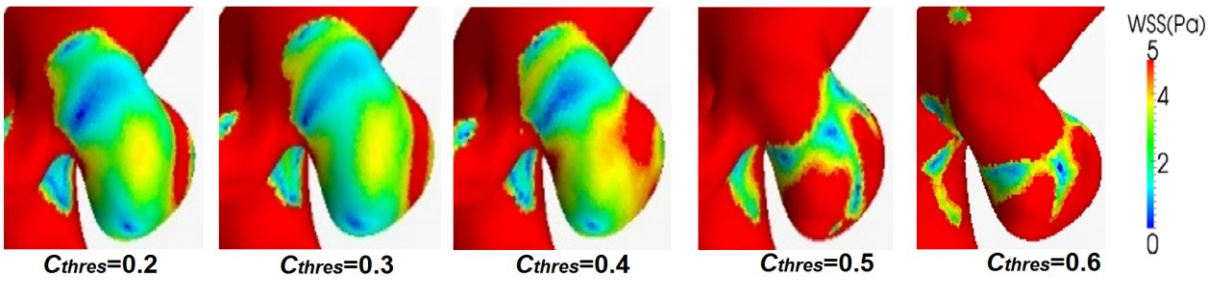

Fig. 2.12 Remarkable change wall shear stress (WSS) distribution when the C_{thres} values increase near to cerebral aneurysms region.

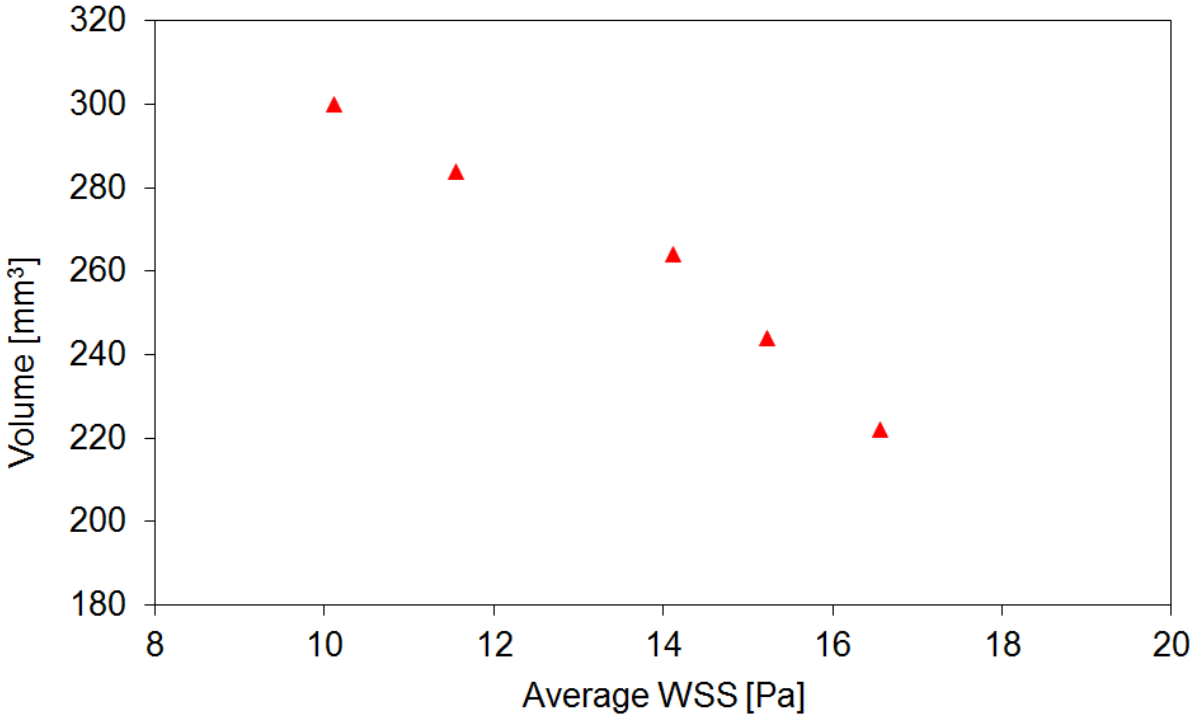

Fig. 2.13 A non-linear negative correlation between volume and average WSS distribution of a patient-specific aneurysm based on different threshold coefficient (C_{thres}) values.

2.3.3 Effect of C_{thres} on the flow-field solution

The variation of the velocity differences between measurement and numerical solution, with different C_{thre} values using a *P*-fixed approach and a *Q*-control approach, is shown in Fig. 2.14. Comparison of these two approaches indicates the minimum velocity difference was obtained at a C_{thres} value of 0.3, which decreased the difference between the measurement and numerical solution from 40% in the *P*-fixed approach to 32% in the *Q*-control approach. After a C_{thres} value of 0.3, the differences increased as the C_{thres} values increased for both approaches. In the box-and-whisker plot, the velocity differences between PC-MRI measurement and CFD simulation with a C_{thres} value of 0.3 were significantly lower than those obtained with C_{thres} values of 0.4, 0.5 and 0.6 ($p < 0.001$) respectively but not significant when compared with C_{thres} values of 0.2.

Normally, the velocity difference and WSS error are predominantly due to image processing and model construction steps because the error from finite element discretization is fairly small. Therefore, the effect of C_{thres} on flow-field solution was evident from the fact that the hemodynamics and blood flow characteristic strongly depend on vessel configuration.

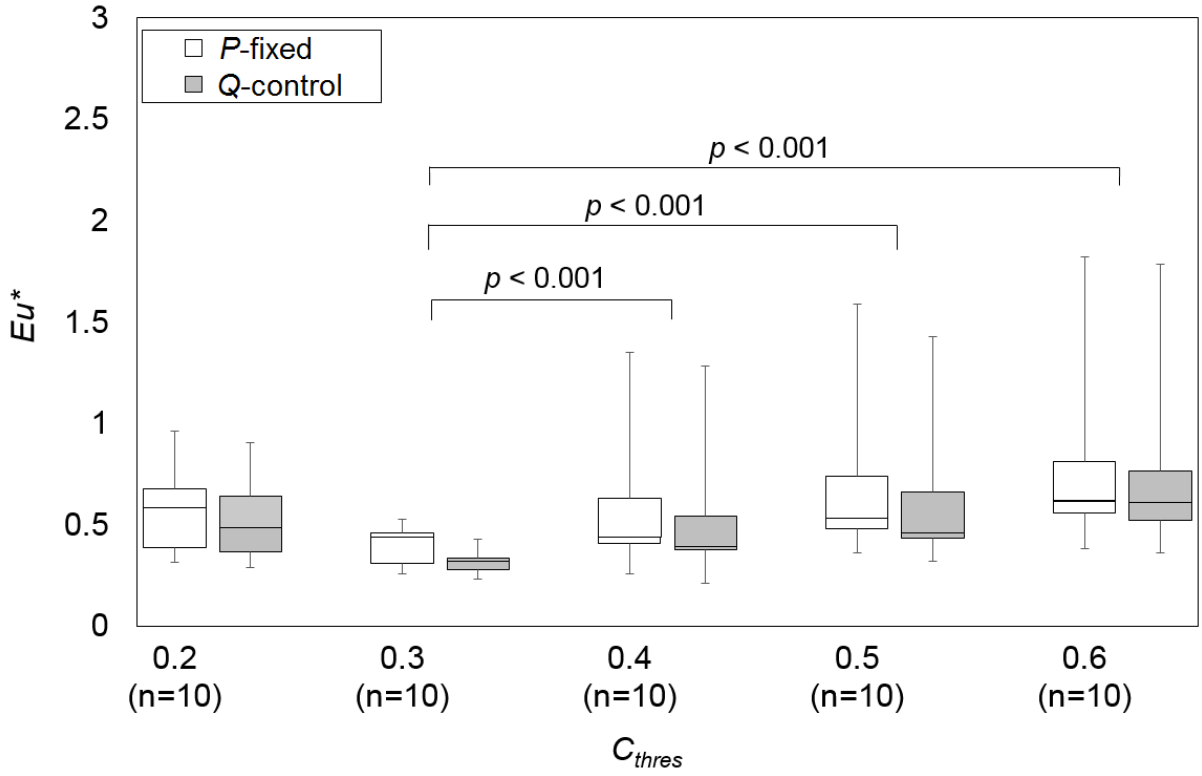

Fig. 2.14 Box-and-whisker plot showing the C_{thres} values in the vessel geometry reconstruction for ten patient-specific aneurysms versus the normalized velocity differences between the measurements and numerical solutions in the *P*-fixed approach and the *Q*-control approach.

2.4 Summary

This chapter investigated the influence of extracted geometry on velocity difference between PC-MRI measurement and CFD simulation for patient-specific blood flow fields. The CFD results exhibited excellent agreement with the previous study that the hemodynamics and blood flow characteristic strongly depend on vessel configuration.

Further detailed development on extensive analysis of the numerical simulation may help to reduce the effect of the reconstructed geometry on the flow-field solution and to verify this beneficial knowledge for clinical application in order to observe the hemodynamic in each patient based on the patient-specific flow characteristics of the blood flow in the aneurysm.

Chapter 3

Minimizing the blood velocity difference between PC-MRI and CFD simulation in cerebral arteries and aneurysms

3.1 Introduction

Since the flow characteristic in the patient-specific aneurysms highly depends on its geometry as Chapter 2, it is still not enough to identify the factor affecting the blood flow fields and hemodynamics factor. Thus, to complete the study, it would be important to further investigate the effect of boundary treatment on patient-specific blood flow fields.

In recent years, remarkable progress has been made in numerical simulation of blood flow in realistic boundary condition constructed between CFD simulation and PC-MRI measurement. It has reported, the numerical simulations can encounter problems relating to the specification of realistic boundary conditions [42]-[45]; inaccurate boundary conditions can introduce unphysical modeling errors. However, little information is available in the literature about the accuracy of the approach and quantitative differences between PC-MRI measurement and CFD simulation, especially on boundary condition and vessel configuration as discussed in Chapter 2.

In order to obtain a more realistic comprehension of blood flow alteration, a combinatorial boundary condition was implemented in the hemodynamic simulation. A way to avoid the incorrect specification of boundary conditions is to use velocity profiles obtained from PC-MRI. In [20], [46], [47], blood flow simulation of carotid bifurcations was performed, and the results were compared with PC-MRI measurements. These studies indicated that CFD

combined with PC-MRI could be useful for obtaining the blood flow field. However, the velocity profile was poorly resolved in space and time, and included measurement noise; so it is not clear that the measured velocity can be used directly as the boundary condition in CFD analysis.

In this chapter, we have proposed a novel basic framework, called velocity-field optimized (*V*-optimized) approach, to couple the velocity fields in the measurement and computation, in which a set of pressure values on outlet boundary (outlet pressure) is determined based on an optimization problem. The present approach solves the direct problem iteratively. Moreover, it enables the use of commercial software to solve the fluid system without any modifications. To show the effectiveness of the present approach, we have compared this boundary treatment of outlet pressures, with previous approaches in Chapter 2; *P*-fixed approach and *Q*-control approach.

3.2 Methodology

3.2.1 Patient-specific aneurysms

Ten patient-specific aneurysms were acquired from clinical digital subtraction angiology (DSA) at Osaka University hospital. The aneurysms formed in the internal carotid artery (ICA), anterior cerebral artery (ACA), middle cerebral artery (MCA) and basilar artery (BA). The longest diameter was approximately 9.13 mm (see Table 2.1 in Chapter 2).

3.2.2 Blood flow analysis

The blood flow is assumed to be an incompressible Newtonian fluid, and its flow is steady. The blood flow analysis was conducted using the steady incompressible Navier-Stoke equation given in eq. (2.4) and (2.5). The following conditions were imposed on the boundaries of the artery and aneurysm; a uniform velocity (see Table 2.2) at the inlet and no-slip condition at the fixed walls. Then, for the outlet boundaries, we have applied the velocity field (V-optimized) approach as discussed in the next section.

3.2.2.1 Velocity-field optimized (V-optimized) approach

In the previous chapter 2, the Q-control approach in (2.6) reduces the flow rate difference between the CFD and PC-MRI at each outlet. However, in the PC-MRI measurement, the spatial resolutions at the outlets are coarse compared with the inlet, and thus the estimation accuracy of the outlet flow rate is low because of the observation noise. Thus, in the Q-control approach, the computational velocity field in the entire domain is not reliable because the entire velocity field is affected by the outlet flow rate distribution. Meanwhile, the full velocity information obtained from the PC-MRI is used for the CFD.

In this chapter, a basic framework for imposing a pressure condition on the outlet boundary was proposed and so-called velocity-field optimized (V-optimized) approach, which minimizes a velocity difference between the CFD velocity $\mathbf{u}$ and PC-MRI velocity $\mathbf{U}$ over the entire domain, i.e., reduces L^p norm of the velocity difference, $\|\mathbf{U}-\mathbf{u}\|_p$, by changing the outlet pressure at each branch. In the V-optimized approach, we solve the following combinatorial optimization problem:

$$\begin{aligned} &\min \left\| \mathbf{U} - \mathbf{u} \right\|_p \\ &\text{w.r.t.} \quad p^{(i)} \in \mathbf{H} \ \text{ for } \ i \in [1, I] \\ &\text{s.t.} \quad \text{Eqs. (2.4) and (2.5).} \end{aligned} \tag{3.1}$$

Here, the CFD velocity **u** is determined through the governing equations by giving the outlet pressure $p^{(i)}$, and thus, eqs. (2.4) and (2.5) are taken as constraints in the optimization problem. **H** is the set of discrete pressures defined as:

$$\mathbf{H} = \{ P_n \mid n \in [1, N] \} \tag{3.2}$$

where

$$P_n = \frac{P_{\max} - P_{\min}}{N - 1}(n - 1) + P_{\min} \tag{3.3}$$

Here, P_n is the discrete pressure, $P_{\min}$ and $P_{\max}$ are the minimal and maximal pressures, respectively, and N is the total number of discrete pressures as shown in Fig. 3.1. We set $p^{(1)} = 0$, while we find the outlet pressure $p^{(i)}$ for $i \in [2,I]$ in **H**.

In this study, we minimize the L^1 norm of velocity difference, $\|\mathbf{U}\text{-}\mathbf{u}\|_1$, in (2.7), by applying the exhaustive search technique for finding the optimal solution. In this regard, the number of outlet branches is 2 or 3 in this study, and thus the degree of freedoms of the set of all the outlet pressures is N or N^2 at most. The following is a brief summary of the V-optimized approach.

1. Define the set of discrete pressure **H** by giving the minimum and maximum pressures $P_{\min}$ and $P_{\max}$ and the total number of discrete pressures N. In this study, we set N=6.
2. Fix the outlet pressure as $p^{(1)}$=0 for the outlet 1.
3. Set i=2 for the loop of outlet pressure index, and introduce the minimum cost function $J_{\min}$, which is set large enough here.
4. Initialize the outlet pressures as $p^{(j)}=P_{\min}$ for $j \in [2,I]$ and set n=1 for the loop of discrete pressure index.

5. Solve the incompressible Navier-Stokes equations using the outlet pressure set $p^{(i)}$ until the convergence solution is obtained.
6. Evaluate a L^1 norm of velocity difference, $\|\mathbf{U}\text{-}\mathbf{u}\|_1$ as J. If $J < J_{\min}$, $J_{\min} \rightarrow J$ and keep the solution sets $\mathbf{u}_{\min}$, $p_{\min}$.
7. Go to step 8 if $n=N$, otherwise update the outlet pressure as $p^{(i)}=P_{n+1}$ and go to step 5 with $n \rightarrow n+1$.
8. Go to step 9 if $i=I$, otherwise go to step 4 with $i \rightarrow i+1$.

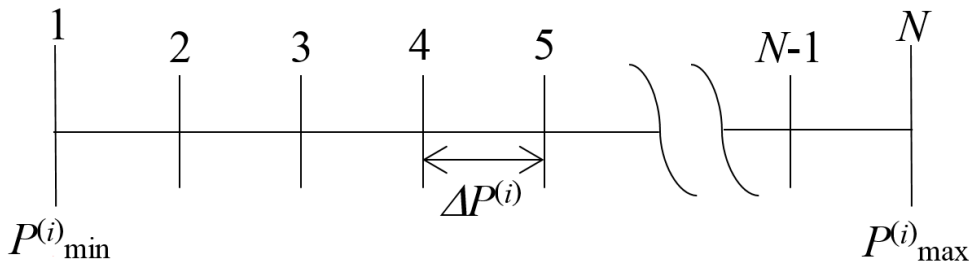

Fig. 3.1 Schematic of the discrete pressure field $P^{(i)}$.

3.3 Results and discussion

In a computational fluid dynamics (CFD) analysis of blood flows using biomedical images, assumptions are often made that can adversely affect the numerical results. One is the boundary conditions**,** and the other is the reconstruction of the vessel geometries through the image analysis.

3.3.1 Effect of boundary treatments on the velocity difference

The distributions of velocity difference magnitude $|\mathbf{U}_m - \mathbf{u}_m|$ in (2.7) for the ten patient-specific aneurysms are presented in Fig. 3.2. The differences were distributed within the domain, and the highest velocity change was observed at a different location for each model. In patients 1, 7, and 10, the areas of relatively high-velocity difference were concentrated around the aneurysmal neck and dome. About 50% of the patients presented large velocity differences at the wall and close to arterial bifurcations. For patients 2 and 4, the large differences were found around both an aneurysm and the wall. These locational differences for the velocity change were attributed to the flow patterns and the relationship between the measurement voxel size and the vessel size. The effects of voxel evaluation can be seen in patients 2, 4, 8, and 9. This is even more evident in smaller vessels, which can have only two or three voxels across their lumen. Nevertheless, in all of the patients, the velocity differences were dramatically decreased when the *V*-optimized approach was employed.

Next, we investigated the quantitative relationship of the velocity difference in the boundary treatments. Both the velocity difference norms defined in (2.8) and (2.9) for the ten patient specific data are shown in Fig. 3.3. All the differences with the *Q*-control approach were slightly improved over those with the *P*-fixed approach. Moreover, the differences with *V*-

optimized approach were significantly reduced; they were approximately 19.8%, 19.1%, 19.2%, 17.8%, 19.9%, 18.1%, 15.2% 24.7%, 21.6%, and 17.6% for patients 1–10 respectively; 80% (8/10) of patients had a reduced velocity difference of less than 20%. A high reduction of velocity difference (>30%) was shown for patients 1 and 4–7, whereas a small reduction (6.3–25%) was found for the other patients in Fig. 3.3. The smaller reduction in velocity difference could be attributed to the relative size of the spatial measurement resolution, to the vessel diameter (shown in Fig. 3.2 (b, c, h-j)), where the measurement voxel occupied the vessel wall, and the velocity information in the voxel was not reliable for the blood velocity. The detailed contour maps of E_u (*norm velocity difference*) distribution on discrete pressure fields presented in *V*-optimized approach for ten patient-specific aneurysms shown in Fig. 3.4. In the circumstance of three branches, for example *Q*-control approach and *V*-optimized approach presented, the pressure at P_{out2} and P_{out3} acquired similar range were (0-250Pa : 0-260Pa), (250-500Pa : 0-500Pa), (0-150Pa : 100-250Pa), (-200-0Pa : 0-400Pa), (-50-50Pa : 50-150Pa), (0-200Pa : 100-300Pa) and (50-200Pa : -100-200Pa) from patient 1 to patient 7 respectively. However, the result indicated the huge range of outlet boundary in case of the real application but given the significant prediction on CFD analysis. On the other hand, the repetition process and the computational time were frequently increased.

The normalized velocity differences shown in Fig. 3.3 are statistically summarized using the box-and-whisker plot in Fig. 3.5. In addition, we evaluated the mean for the normalized velocity differences in respective boundary treatments. It was found they were 40.3% in the *P*-fixed approach, 32.1% in the *Q*-control approach, and 19.3% in the *V*-optimized approach, respectively. The normalized norm of velocity difference with the *V*-optimized approach was significantly lower than that obtained with the *P*-fixed approach ($p < 0.001$) and the *Q*-control approach ($p < 0.001$).

P-fixed	*Q*-control	*V*-optimized

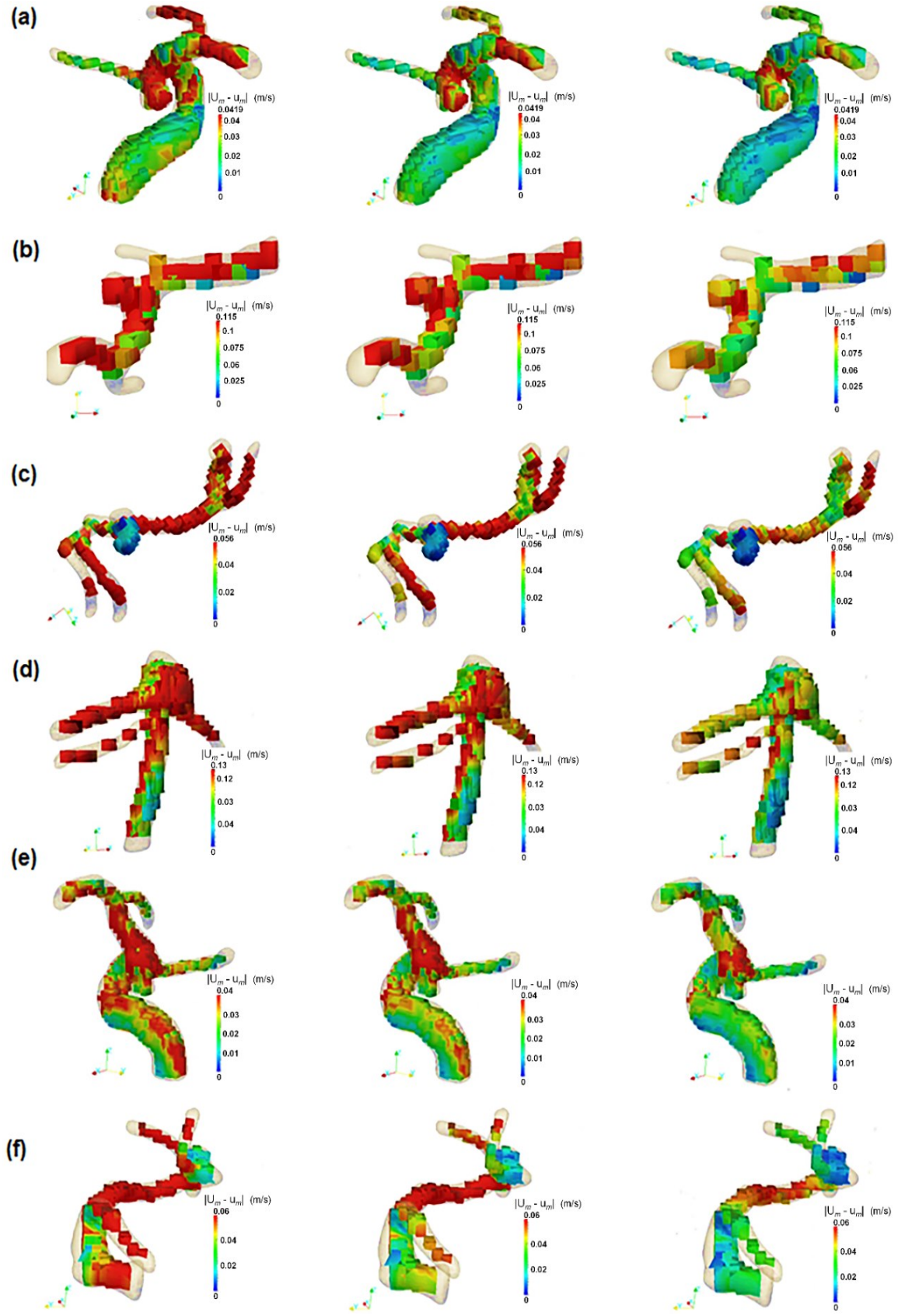

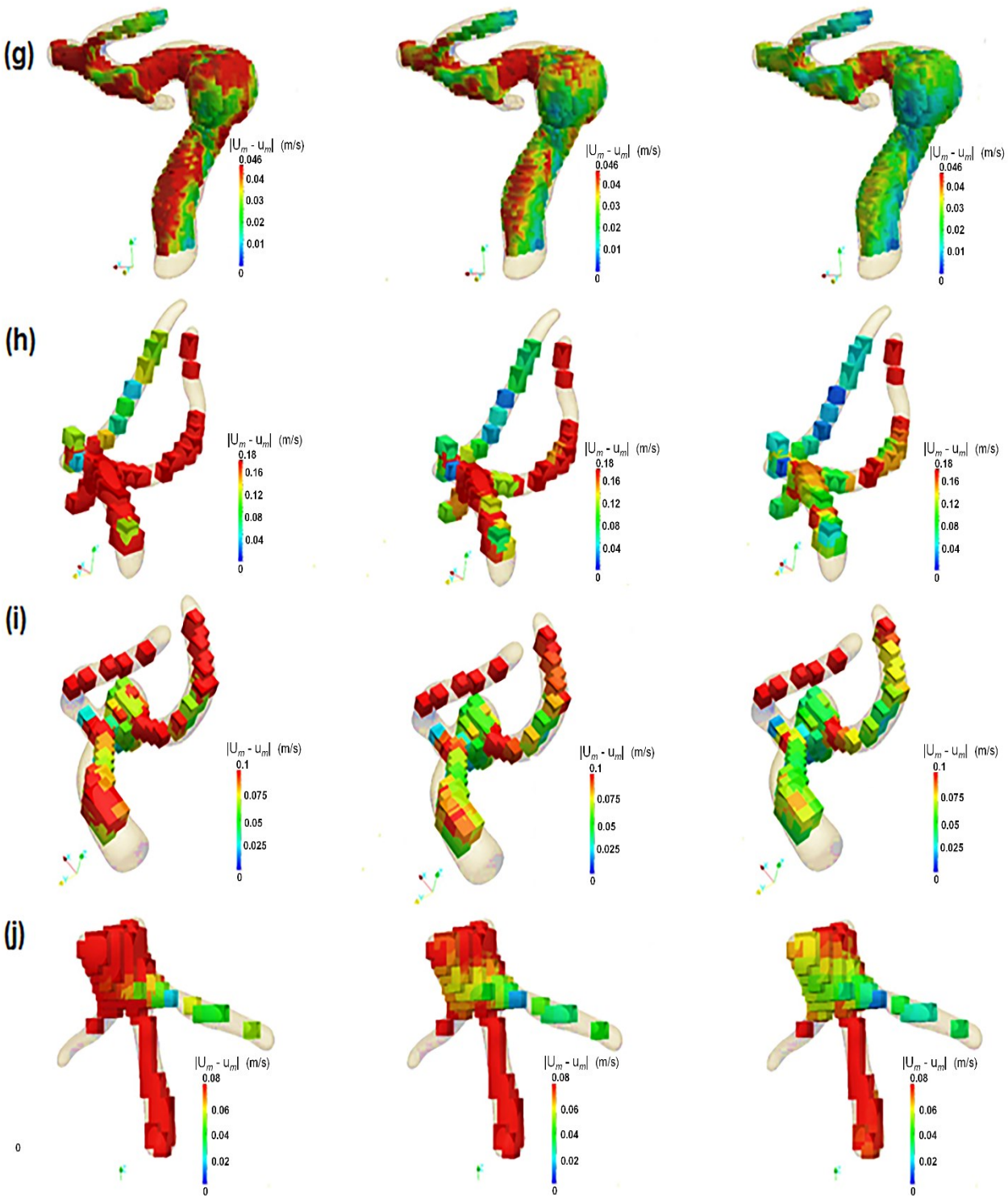

Fig. 3.2 Comparisons of velocity difference [unit: m/s] distribution on ten patient-specific aneurysms (a) patient 1, (b) patient 2, (c) patient 3, (d) patient 4, (e) patient 5, (f) patient 6, (g) patient 7, (h) patient 8, (i) patient 9, and (j) patient 10, for different boundary treatments, the *P*-fixed approach (*left column*), the *Q*-control approach (*middle column*), and the *V*-optimized approach (*right column*).

For a C_{thres} value of 0.3, the quantitative comparison shows that the lowest and highest velocity differences were obtained using the *V*-optimized approach and *P*-fixed approach with median values of 19.2% and 44.1%, respectively. However, the velocity differences remained when minimizing the velocity difference norm in the *V*-optimized approach. One possible reason is that of the measurement accuracy of the PC-MRI, including the relatively low spatial resolution regarding the vessel size. The other reason is because of the assumptions of a rigid wall, and a Newtonian viscous model in the CFD analysis.

In the present study, we investigate the velocity difference between PC-MRI and CFD simulation by using all the velocity data obtained from PC-MRI measurement and this *V*-optimized approach accurately performed the best when searching for the optimal solution. However, this present approach is tremendously expensive regarding computational cost because the grids are made of a large number of cells (up to millions of cells), and the simulation time increased due to a combinatorial optimization with an exhaustive search is applied to find the optimal solution deal with a real patient-specific geometry.

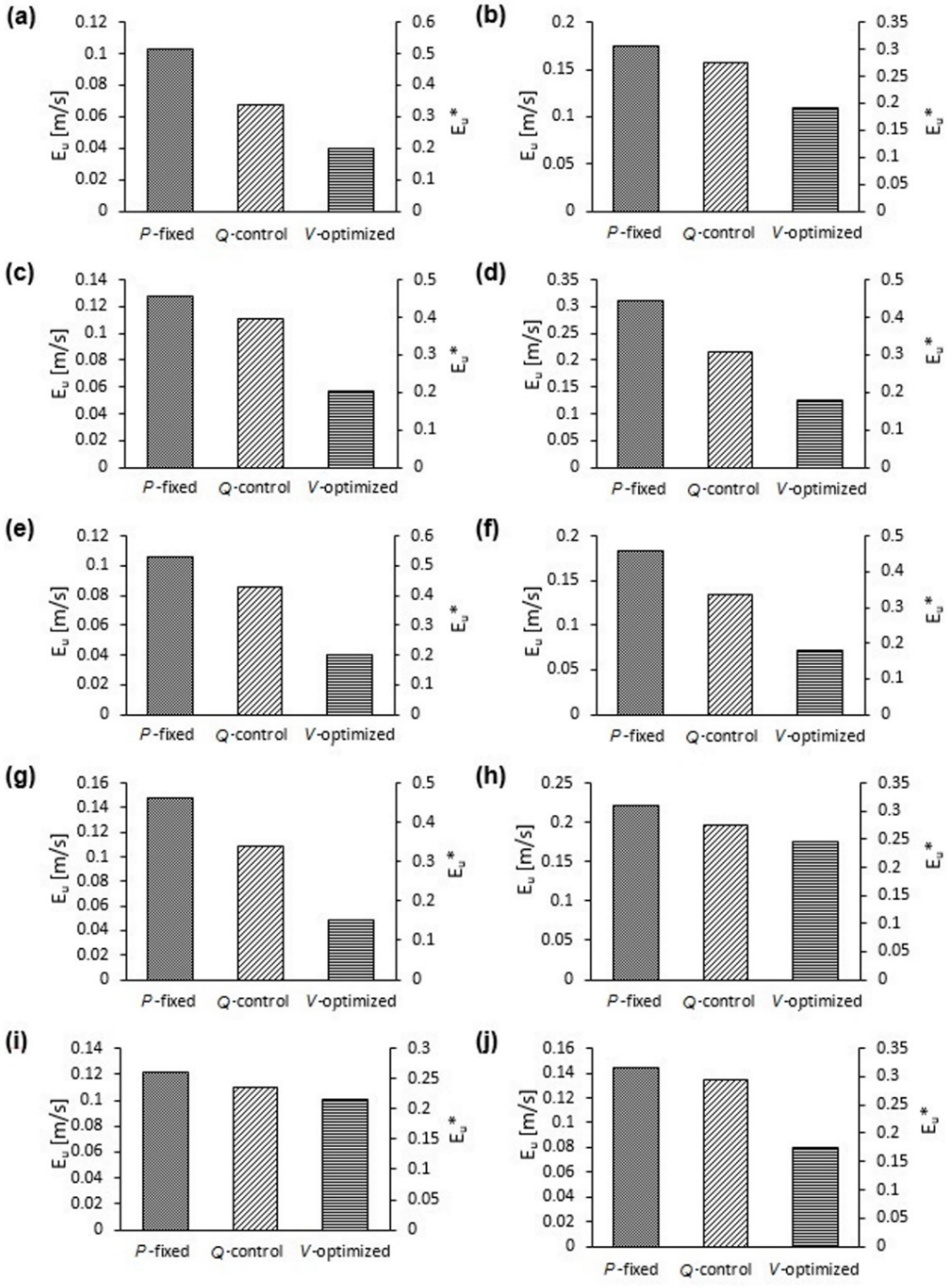

Fig. 3.3 Comparison of E_u (*norm of velocity difference*) and E_u* (*normalized norm of velocity difference*) for ten patient-specific aneurysms. (a) patient 1, (b) patient 2, (c) patient 3, (d) patient 4, (e) patient 5, (f) patient 6, (g) patient 7, (h) patient 8, (i) patient 9, and (j) patient 10, in terms of different boundary treatments, the *P*-fixed approach, the *Q*-control approach, and the *V*-optimized approach. The analysis was investigated at C_{thres} value of 0.3.

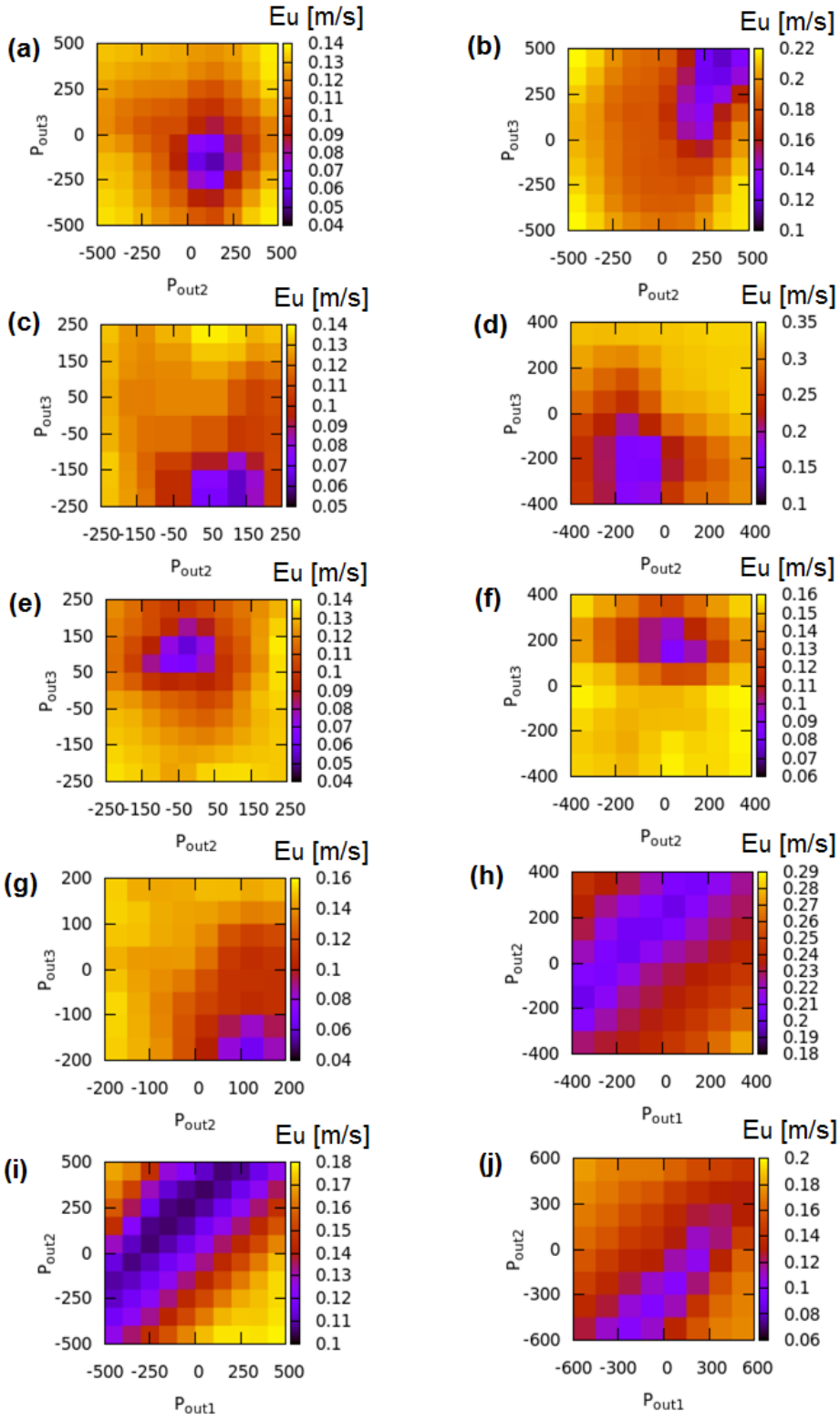

Fig. 3.4 Contour maps of E_u (*norm of velocity difference*) on discrete pressure fields presented in *V*-optimized approach for ten patient-specific aneurysms. (a) patient 1, (b) patient 2, (c) patient 3, (d) patient 4, (e) patient 5, (f) patient 6, (g) patient 7, (h) patient 8, (i) patient 9, and (j) patient 10.

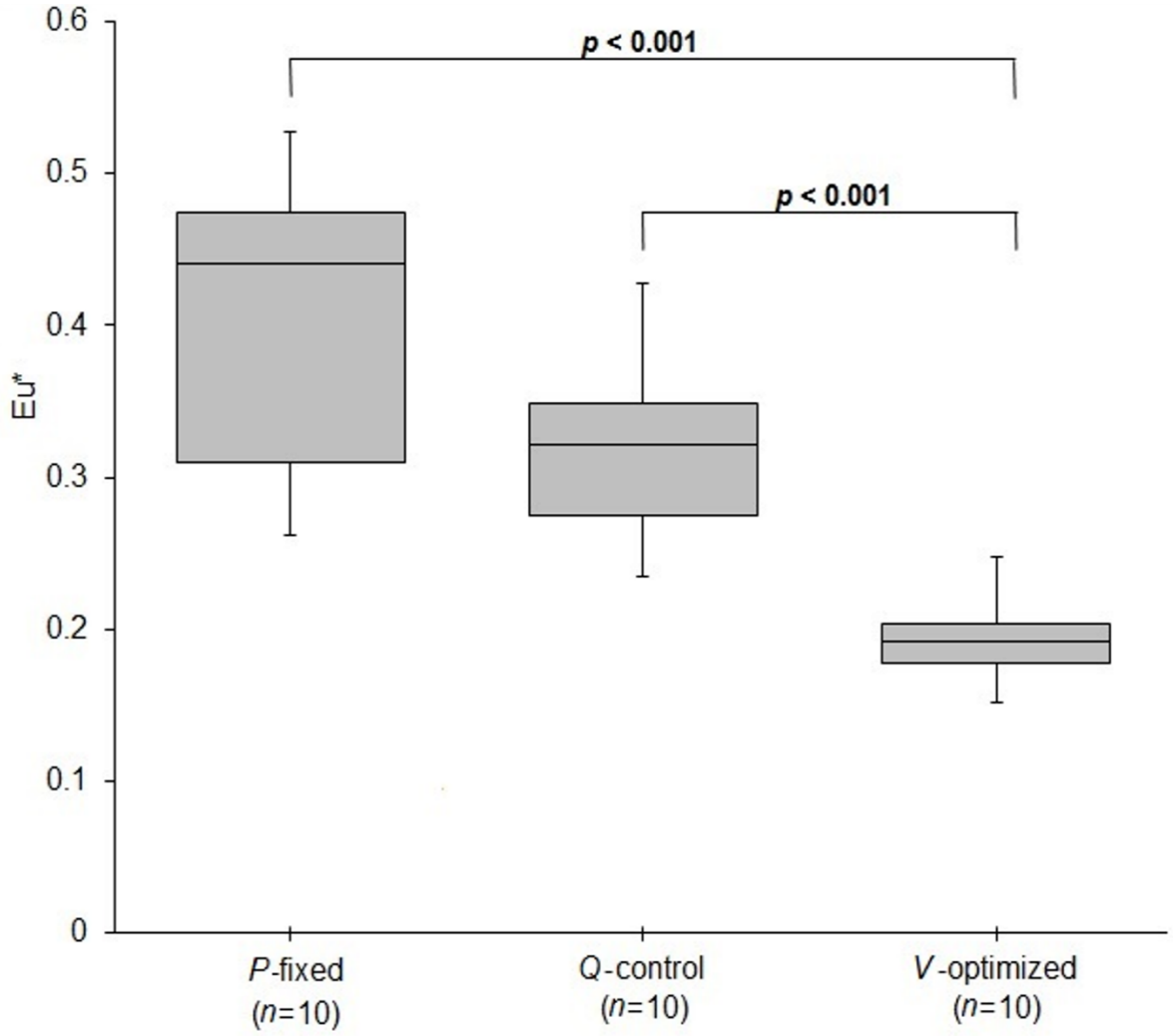

Fig. 3.5 Box-and-whisker plot showing the normalized norm of the velocity difference between the measurement and numerical simulation for the ten patient-specific aneurysms with different boundary treatments. The highest values of velocity difference were for the *P*-fixed approach (*right*), the second-highest for the *Q*-control approach (*middle*), and the lowest for the *V*-optimized approach (*left*).

3.3.2 Local velocity difference in aneurysm and non-aneurysm parts

The *V*-optimized model showed good improvement in decreasing the velocity difference in the overall domain. One of the important issues in the present analysis is how the flow field is represented by the aneurysm part when compared with the full geometry. Here, we evaluate local velocity differences in the aneurysm and non-aneurysm parts separately. The normalized norm defined in (2.9) was used for the evaluation of the local velocity differences, where the summations in (2.8) were used for the aneurysm and non-aneurysm parts, respectively. The results are shown in Fig. 3.6. Analogous to the overall velocity difference, the *V*-optimized model showed the smallest different in both the mean and standard deviation for the aneurysm and non-aneurysm parts, which was approximately half of those with the *P*-fixed and the *Q*-control. In the present *V*-optimized model, the evaluation function (2.7) adopted the overall norm over the whole domain, and thus the reduction of velocity difference when compared with the *Q*-control model was roughly uniform in both the aneurysm and non-aneurysm parts, as shown in Fig. 3.6.

However, as mentioned in the previous subsection, the measurement velocity in the low-resolution part compared with the vessel diameter was not reliable because of measurement noise. This suggests that the local velocity difference in the aneurysm part is improved when we adopt a weight function depending on the measurement resolution or position; for example, we can use a high weight for the norm evaluation in (2.8) around an aneurysm or large vessel part. Nevertheless, even in the simple evaluation with the uniform weight used in this study, the present *V*-optimized model is capable of reducing the velocity differences in the aneurysm part by approximately 19%.

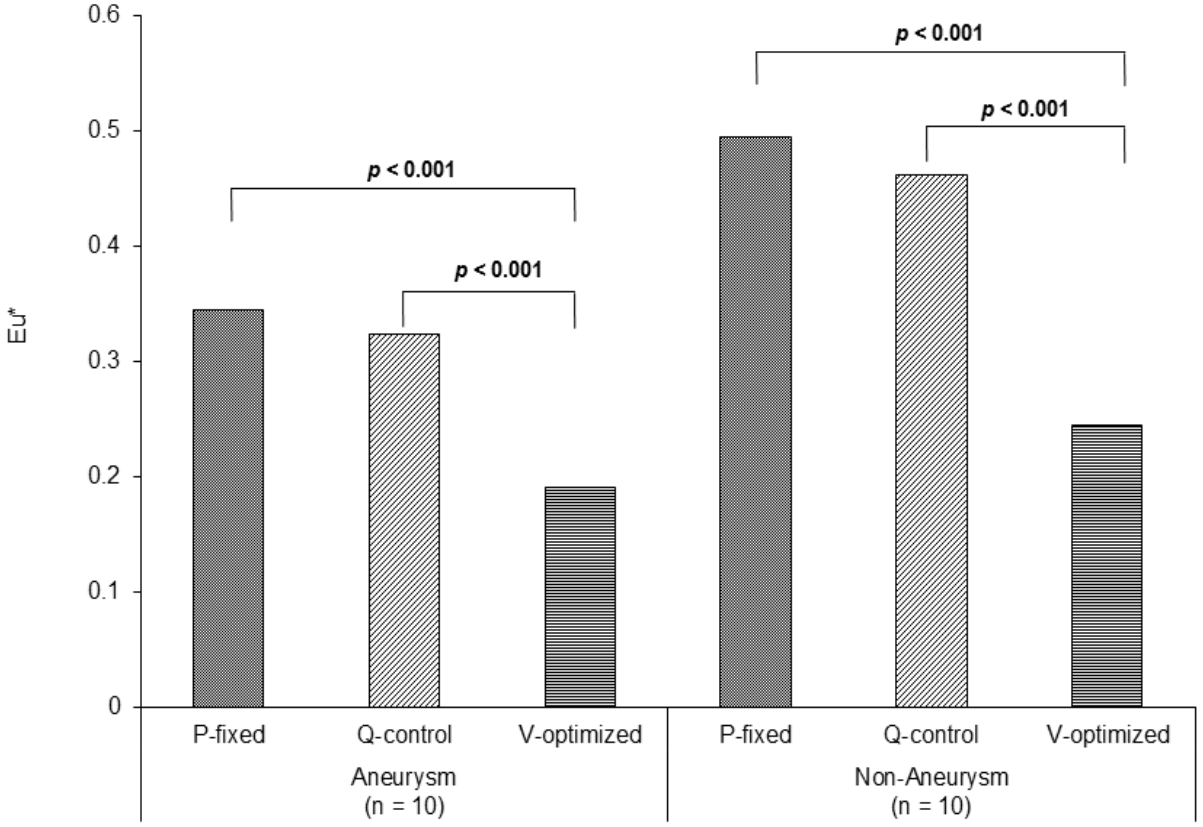

Fig. 3.6 Normalized norms of the local velocity difference in the aneurysm and non-aneurysm parts for the ten patients, with different boundary treatments, *P*-fixed, *Q*-control, and *V*-optimized approaches.

3.3.3 Effect of boundary treatments on WSS

Hemodynamic values such as wall shear stress (WSS) are important factors in the growth and rupture of a cerebral aneurysm [23], [48]. However, these factors are strongly attributed to the flow pattern, and thus a flow analysis with poorly posed boundary conditions may lead to an incorrect hemodynamic model.

Here, we investigate how the different boundary treatments used in this study affected the computation of the WSS around the aneurysm and non-aneurysm parts. Fig. 3.7 shows the WSS obtained from the flow velocity in the CFD model with the various boundary conditions for the ten patients. Significant decreases in the value of the WSS were observed in the different boundary conditions for both the aneurysm and non-aneurysm parts. The highest value of WSS was obtained in the *P*-fixed approach, and the second-highest value was obtained in the *Q*-control approach. Meanwhile, the *V*-optimized model showed the lowest value of WSS. In the *P*-fixed and *Q*-control approaches, no significant change of WSS values was observed because of the inaccurate boundary conditions. In contrast, for the *V*-optimized approach, Fig. 3.7 shows the WSS value obtained for the aneurysm and non-aneurysm parts was significantly reduced in comparison with the *P*-fixed ($p < 0.001$) approach. However, the WSS value obtained in the *V*-optimized approach was significantly lower than the *Q*-control approach ($p < 0.001$), but only in the aneurysm part.

In other aneurysm study, the higher WSS distribution for aneurysm and non-aneurysm depends not only on the boundary condition used but also on the way the blood flows from the parent vessel into the aneurysm, which in turn is influenced by the geometry of the cerebral artery [34]. In some aneurysms cases, the blood flows from the parent vessel directly into the aneurysm, resulting in a concentrated inflow jet [29] that impacts the aneurysm wall, producing a region of locally higher WSS distribution.

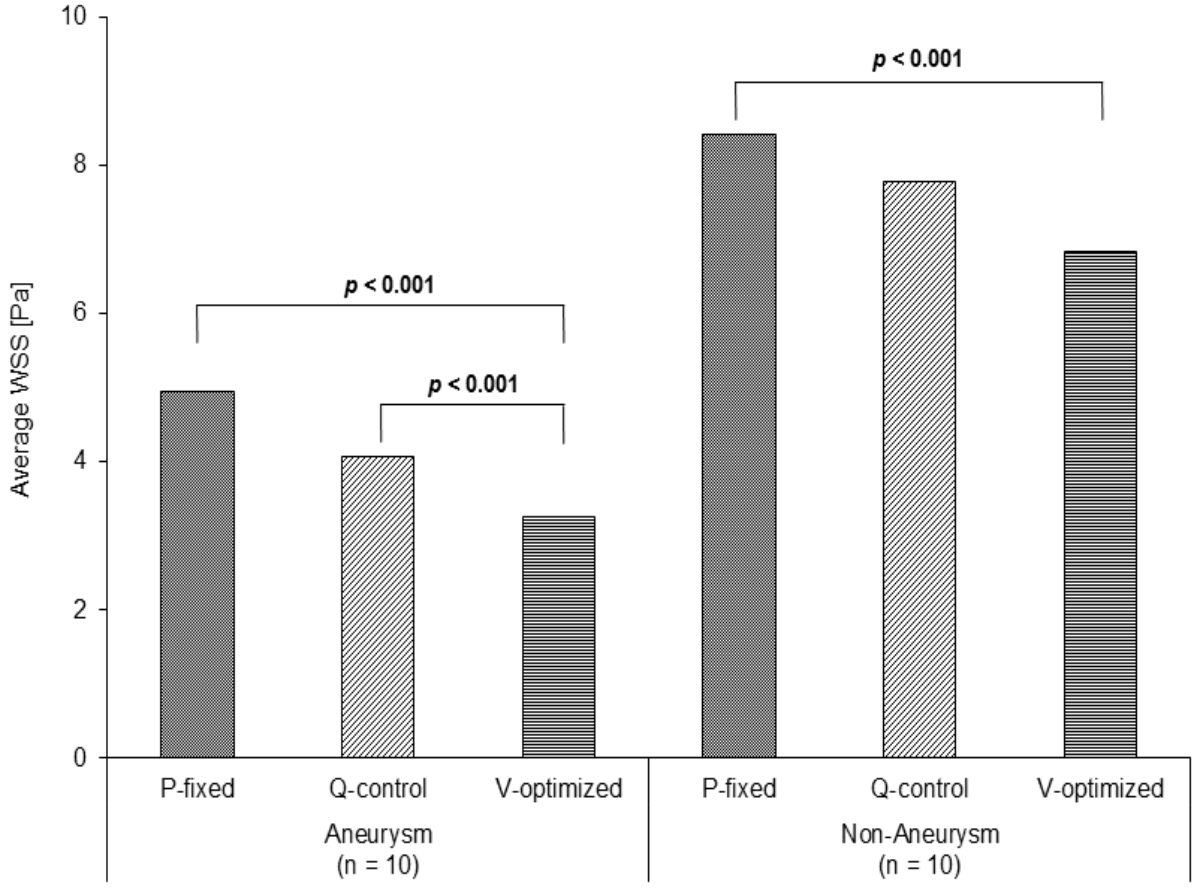

Fig. 3.7 Comparison of wall shear stress (WSS) for the three different boundary treatments. The average WSS region of the aneurysm (*right*) and non-aneurysm (*left*) parts at the peak systole for the ten patient-specific aneurysms.

In other patient-specific aneurysm studies, the higher WSS distribution depends not only on the boundary condition but also on the blood flow stream from the parent vessel into the aneurysm, which in turn is influenced by the geometry of the cerebral artery. In some aneurysm cases, the blood flows from the parent vessel directly enter into the aneurysm, resulting in a concentrated inflow that impacts the aneurysm wall, producing a region of locally higher WSS distribution. Other aneurysms have a more diffuse inflow that produces a slower aneurysm flow pattern and a more uniform WSS distribution than the non-aneurysm parts [34].

Fig. 3.8 (*top*) shows the velocity vectors of PC-MRI and CFD with different boundary treatments at PC-MRI measurement points around the daughter and aneurysm part for patients 7. The large differences in the magnitude of velocity vector between PC-MRI measurement and CFD simulation are perceived inside an aneurysm. In the *V*-optimized, Fig. 3.8 (*top-right*) shows the magnitude of the velocity vector differences between CFD and PC-MRI in an aneurysm are significantly reduced in comparison with those of *P*-fixed and *Q*-control approaches. By estimating the realistic pressure boundary based on the *V*-optimized approach, the flow pattern was completely changed along with the reference (PC-MRI measurement) velocity field even inside the aneurysm.

Next, we investigate how these flow pattern changes affect the WSSs in the CFD solution. Fig. 3.8 (*bottom*) shows the WSSs obtained from the flow velocity in the CFD with different boundary treatments for same patients. These results show the WSS was changed in the Fig. 3.8 (*bottom*) in different boundary treatments. The highest value of WSS is obtained in the *P*-fixed approach, and the second-highest value is obtained in the *Q*-control approach. Meanwhile, the *V*-optimized shows the lowest value of WSS. The present results show that a flow analysis with poor boundary conditions gives an unrealistic flow distribution that compares badly with the actual flow (measurement), and incorrectly estimates the WSS around an aneurysm.

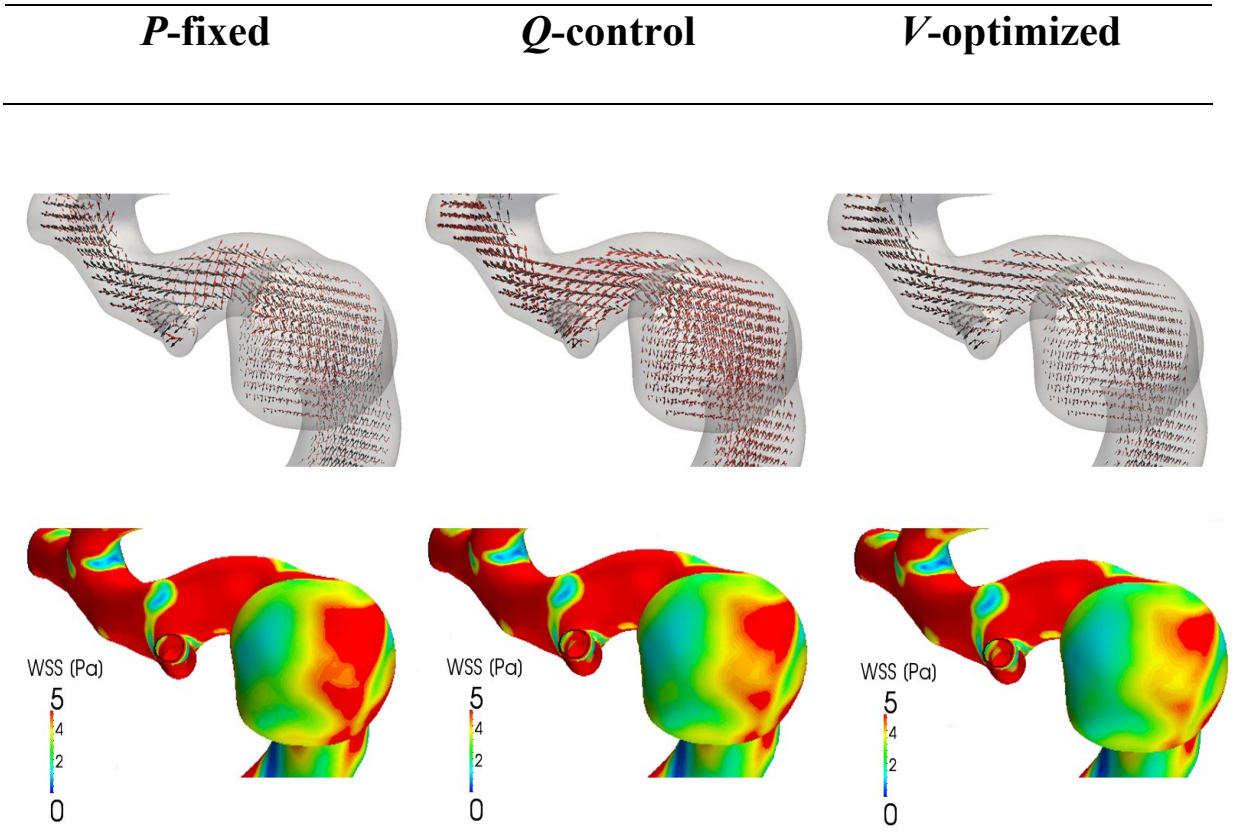

Fig. 3.8 Comparison of velocity fields (*top*); red and black arrow indicates the CFD and PC-MRI velocity respectively, and wall shear stress distribution (*bottom*) for patient 7, in terms of different boundary treatments, the *P*-fixed approach, the *Q*-control approach, and the *V*-optimized approach.

3.4 Summary

In this chapter, the minimizing of velocity difference between PC-MRI measurement and CFD simulation was investigated and discussed the effects of difference boundary treatment on flow field solution for patient-specific aneurysms. The basic strategy was proposed, namely, the *V*-optimized approach to impose the boundary condition (outlet pressure boundaries) with couple the velocity fields in the measurement and computation, based on an optimization problem.

In the *V*-optimized approach, because the outlet pressure was determined such that the norm of velocity difference was minimized based on the combinatorial optimization strategy, the normalized norms of the velocity difference for all ten patients were significantly reduced to 19.3% in the mean, which was much less than those of 40.3% in the *P*-fixed approach and 32.1% in the *Q*-control approach. This was also established in the local domain of the blood vessel and confirmed that the differences in the boundary treatments affect the WSS values in both the aneurysm and non-aneurysm parts.

This chapter exhibits that the boundary condition setup (outlet boundaries) plays an important role in the flow field solution between measurement and simulation, which may be a key issue for the treatment effectiveness on the patient-specific aneurysm.

Chapter 4

The feasibility study of physically consistent feedback control based data assimilation (PFC-DA) method on patient-specific aneurysms

4.1 Introduction

Previous chapters revealed the effects of vessel configuration (Chapter 2) and the effects of boundary treatment (Chapter 3) on flow field solution between PC-MRI measurement and CFD simulation for a patient-specific aneurysm. Although the previous studies have a potential to obtain the "optimal solution" in each patient, the solution is vain due to the high computational cost when conducted an exhaustive search technique in *V*-optimized approach.

An alternative data assimilation method based on the optimal control [49], [25], [50] have been applied in blood flow analysis. A comprehensive understanding of the relationship between the variational and statistical (Bayesian) approaches has been also attempted [27]. In optimal control based approaches, the formulation is mathematically clear. However, the analysis usually requires a large computational cost and is still under development for practical time-dependent problems.

In the current study by [26], data assimilation approach has been developed based on feedback control theory. This approach introduces a body force attributed to the residual velocity term, which is the difference between the reference and numerical data, to drive the flow. Although the body force naturally fits in the momentum equation that maintains mass conservation, an unphysical pressure field appears due to this momentum source. Ideally, this

would be remedied in a post-procedure on the obtained pressure field [26]. However, it is still unclear that the body force would bring an unphysical acceleration or rotation in the flow around the location where the body force is imposed. As compared with optimal control-based approaches [25], [27], [49], [50], the conventional feedback control-based approach is not guaranteed to provide the optimal solution. However, the computational cost is generally low because the velocity residual between the reference and numerical data is incorporated into the system as a kind of penalty term.

In this chapter, a physically-consistent feedback control based data assimilation (PFC-DA) method was proposed and discussed in terms of the feasibility and accuracy.

4.2 Methodology

4.2.1 Patient-specific analysis on cerebral aneurysms

The patient-specific geometries of the cerebral aneurysms were reconstructed through image analysis using a commercial software AMIRA 5.4.2 (Visage Imaging, Berlin, Germany), with DSA images with a pixel/slice resolution of 0.1 mm. The patient-specific models remain same with previous Chapter 2 and Chapter 3. However, the geometry extension was applied due to the setting of domain size in Cartesian mesh. Detail geometries for all ten patients were showed in Fig. 4.1.

The spatial resolution of the PC-MRI measurement data were 0.72, 0.72 and 0.5 mm for the *x, y, z* directions, respectively. In this analysis, the CFL number was approximately 0.1 base on the setting of mesh resolution and the time increment.

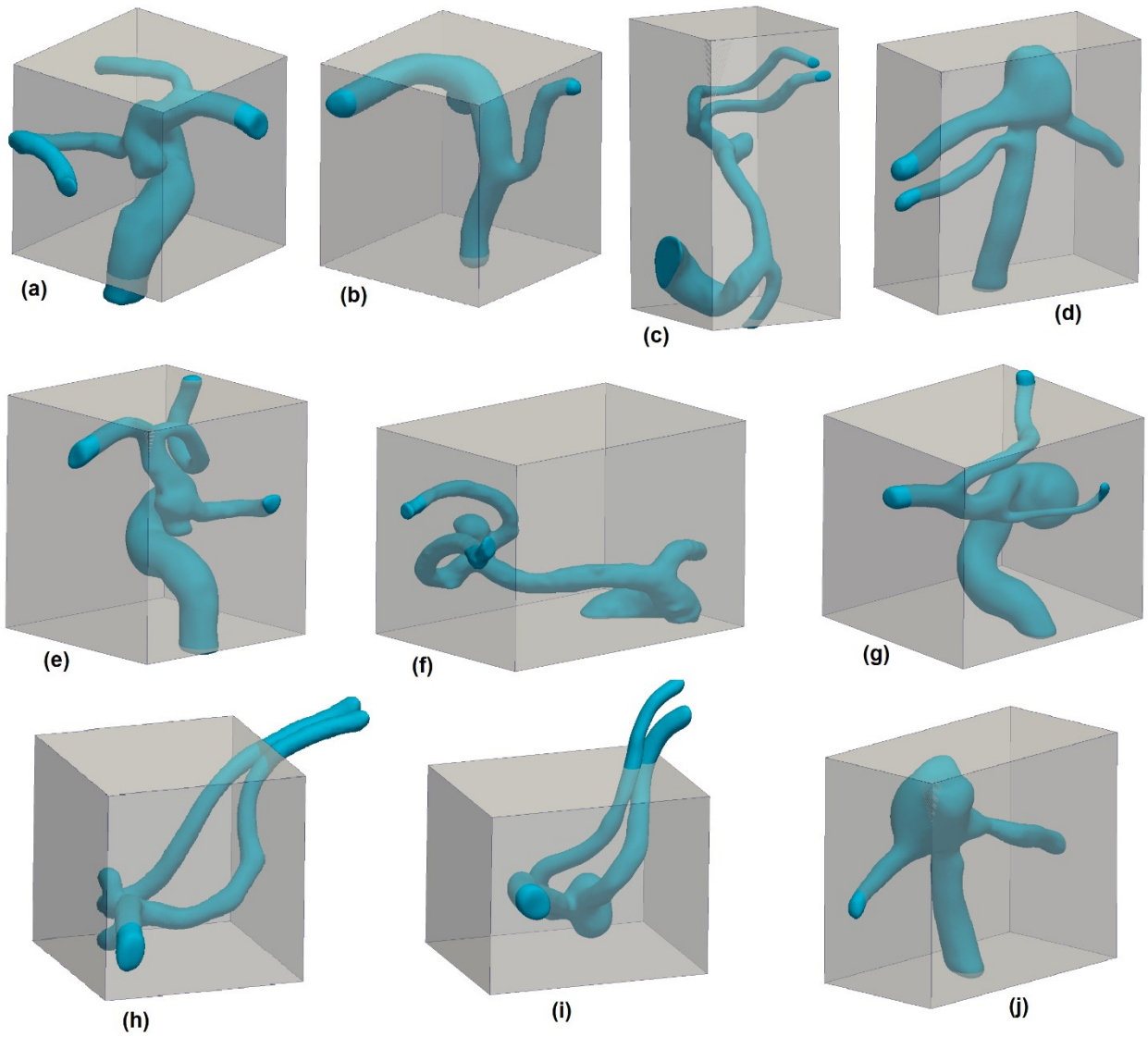

Fig. 4.1 Extension of the geometries for all ten patient based on domain size in Cartesian mesh system. (a) patient 1, (b) patient 2, (c) patient 3, (d) patient 4, (e) patient 5, (f) patient 6, (g) patient 7, (h) patient 8, (i) patient 9, and (j) patient 10.

4.2.2 Basic idea of the PFC-DA method

The governing equations are the incompressible Navier-Stokes equations (4.1) and continuity equation (4.2) as follows

$$\rho\,(\partial_t\,\mathbf{u} + \mathbf{u}\cdot\nabla\,\mathbf{u}) = -\nabla p + \mu\nabla^2\,\mathbf{u} \tag{4.1}$$

$$\nabla\cdot\mathbf{u} = 0 \tag{4.2}$$

where $\mathbf{u}$ is the velocity vector, ρ is the density and μ is the dynamic viscosity. The pressure driven system with a set of boundary conditions is given by

$$\begin{aligned} \mathbf{u} &= 0, && \text{on } \Gamma_w \\ -pn + \mu\partial_n\,\mathbf{u} &= -\phi_n && \text{on } \Gamma_{in},\ \Gamma_{out} \end{aligned} \tag{4.4}$$

where Γ_w, Γ_{in}, Γ_{out} are the wall, inlet and outlet boundaries and ϕ is the boundary pressures including both inlet and outlet. A basic idea of the present approach is to determine the boundary pressure ϕ based on the feedback control theory (*proportional control*). Since we regard the solved velocity $\mathbf{u}$ as an output from the system and the reference velocity $\mathbf{U}$ as the desired output, we derive a general form of the feedback control system as

$$\mathbf{f} = K\,(\mathbf{U} - \mathbf{u}) \tag{4.4}$$

where $\mathbf{f}$ is the control signal sent to the system or body force, and K is the feedback gain. To incorporate the signal $\mathbf{f}$ into the system, Funamoto and Hayase [26] impose it into the momentum equation (4.1) as a body force. However, it is still an open question whether the body force would bring an unphysical flow acceleration and rotation. In a pressure-driven system with a bounded domain, the flow field could be reproduced by giving a set of adequate boundary pressures. Therefore, we do not need to include spatially distributed body forces within the domain into the momentum equations. According to this idea, we cast the signal $\mathbf{f}$ into the analysis system as the pressure boundary condition.

When the pressure difference was dominant to driven the flow, we assume the body force represented by a scalar potential field ϕ

$$\mathbf{f} = -\nabla\phi \tag{4.5}$$

Using a vector calculus identity, the scalar potential field satisfies the following Poisson equation

$$\nabla^2\phi = -\nabla \cdot \mathbf{f} \tag{4.6}$$

with the Neumann boundary condition

$$\partial_n\phi = 0, \qquad \text{on } \Gamma_w, \Gamma_{in}, \Gamma_{out} \tag{4.7}$$

Note that, when a pointwise signal **f** exists, the scalar potential field by ϕ plays a role in driving the flow due to a difference of the measurement velocity **U** and CFD velocity **u**. Therefore, the expected new pressure field is reproduced when the boundary value of ϕ is prescribed as the boundary pressure for Γ_{in} and Γ_{out}.

Consequently, our final system consists of incompressible NS equations (4.1), (4.2) and Poisson equation for scalar potential (4.6) with a set of boundary condition (4.7). The detailed description about the numerical discretization on fixed Cartesian mesh, please refer to Appendix 4.

4.2.3 Calculation of volume fraction (*VOF*) data

The partial differential equations are spatially discretized by a finite difference method in a Cartesian mesh system. To deal with the flow in an arbitrary geometry of the vessels, the boundary data immersion (BDIM) method was introduced [51], in which both the fluid governing equations and no-slip wall condition for a rigid are mixture using a smoothed phase function. The phase functions were calculated by averaging an exact phase indicator function which corresponding to volume fraction, so-called *VOF* function [52]. The *VOF* data on each voxel are calculated based on the extracted vessel geometry represented by a set of surface polygons through the SDFlib library (RIKEN, Japan), where a domain size and the mesh number (nx, ny, nz) for each ten patient shows in Table 4.1.The isosurface of *VOF*=0.5 is shown in Fig. 4.2.

Table 4.1 Spatial discretization parameter for each ten patient-specific aneurysms.

Patient	Domain size [mm]	Number of Mesh (nx,ny,nz)
1	20 x 20 x 20	(80, 80, 80)
2	15 x 15 x 15	(80, 80, 90)
3	25 x 25 x 25	(120, 90, 80)
4	12 x 12 x 12	(160, 80, 170)
5	32 x 32 x 32	(80, 80, 90)
6	27 x 27 x 27	(115, 80, 80)
7	30 x 30 x 30	(90, 80, 80)
8	23 x 23 x 23	(80, 80, 80)
9	18 x 18 x 18	(80, 100, 80)
10	12 x 12 x 12	(150, 80, 130)

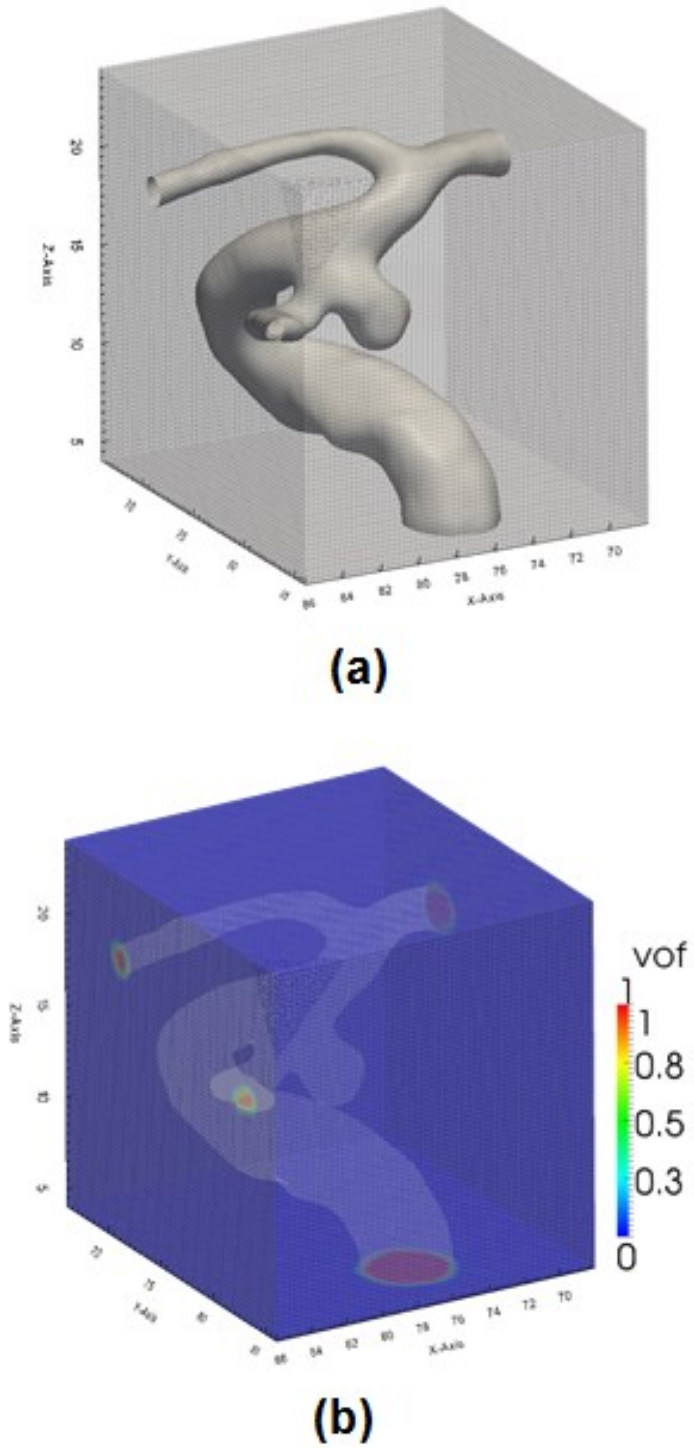

Fig. 4.2 (a) 'Cut'-geometry in a domain. (b) Calculated *VOF* function. The surface represented as *VOF*=0.5. The domain size of 20mm x 20mm x 20mm with the number of meshes for (nx, ny, nz) = (80, 80, 80). The illustration model shows patient 1.

4.3 Results and discussion

The present PFC-DA method was applied to the blood flow on real patient-specific cerebral aneurysm. In order to investigate the accuracy and the feasibility of this present PFC-DA method, first, we have checked the effects of the proportional gain, *Kp*, on flow field solution. Next, we have observed the effects on pressure distribution at the inlet and outlet. Then, we have shown the overall behavior of flow field. Finally, we have presented the detailed information on hemodynamics for all ten patient-specific aneurysms.

4.3.1 Effects of proportional gain (K_p) on flow field solution

In order to investigate the ability of the present PFC-DA method, the test with difference proportional gain K_p values for ten patient-specific aneurysms was conducted. A temporal change of the normalized velocity difference E_u^* between PC-MRI measurement and CFD simulation with difference proportional gain, K_p for each ten patient-specific was shown in Fig. 4.3. As the proportional gain K_p was increased, velocity difference E_u^* becomes smaller, and the convergence speed becomes faster. However, in Fig. 4.3 (e), (f), and (i), E_u^* becomes oscillatory in time by incresing K_p, where the velocity difference E_u^* were approximately 0.25, 0.24 and 0.21 at K_p of 100, 1000 and 1000 respectively. Based on this, the K_p values of 50, 100 and 100 were applied in these three patients and run up the analysis to t = 1 s. The velocity difference E_u^* was gradually decreased over time and converged to a constant approximately 17.1%, 19.5%, 19.7%, 19.0%, 19.4% and 16.9% for patient 1, patient 3, patient 4, patient 5, patient 6 and patient 7 respectively. However, for patient 2, patient 8, patient 9 and patient 10, the velocity difference remain higher were 24.1%, 20.8%, 21.2% and 23.6% respectively. One

possible reason giving such a large velocity difference (> 20%) was assumed that the measurement data are pointwise and that the singular source was used in the evaluation of the scalar potential field. However, because the PC-MRI data were spatially smeared out over its measurement resolution, rather than pointwise [53], and was reformulated it to incorporate the signal as a source into the scalar potential field by using spatial filtering.

As compared to others figure the value of K_p giving a minimal velocity difference E_u^* is gradually shifted to smaller values as the K_p value increases. These results for the relationships of E_u^* with K_p imply that the good assimilated solution was obtained when the behavior of E_u^* was investigated and find the optimal K_p depends on the analysis conditions. Note that, velocity difference E_u^* was strongly affected by K_p .

The main pitfalls of PC-MRI, as compared with DSA is the possibility of overestimation of the voxel size. This undesirable effect may occur if the voxel size is too large related to the diameter of the vessel. Fig. 4.4 shows the influence of inlet diameter of the vessel on the flow solution. These values of normalized velocity difference E_u^* decrease as the inlet diameter of the vessel increases. As well-known, the low spatial resolutions or the use of large voxel will introduce the error and lead to a decrease in total noise. In this sense, the vascular vessel can not only be overestimated but in some cases may even be underestimated if the voxel size is so large that the partial volume effect becomes important.

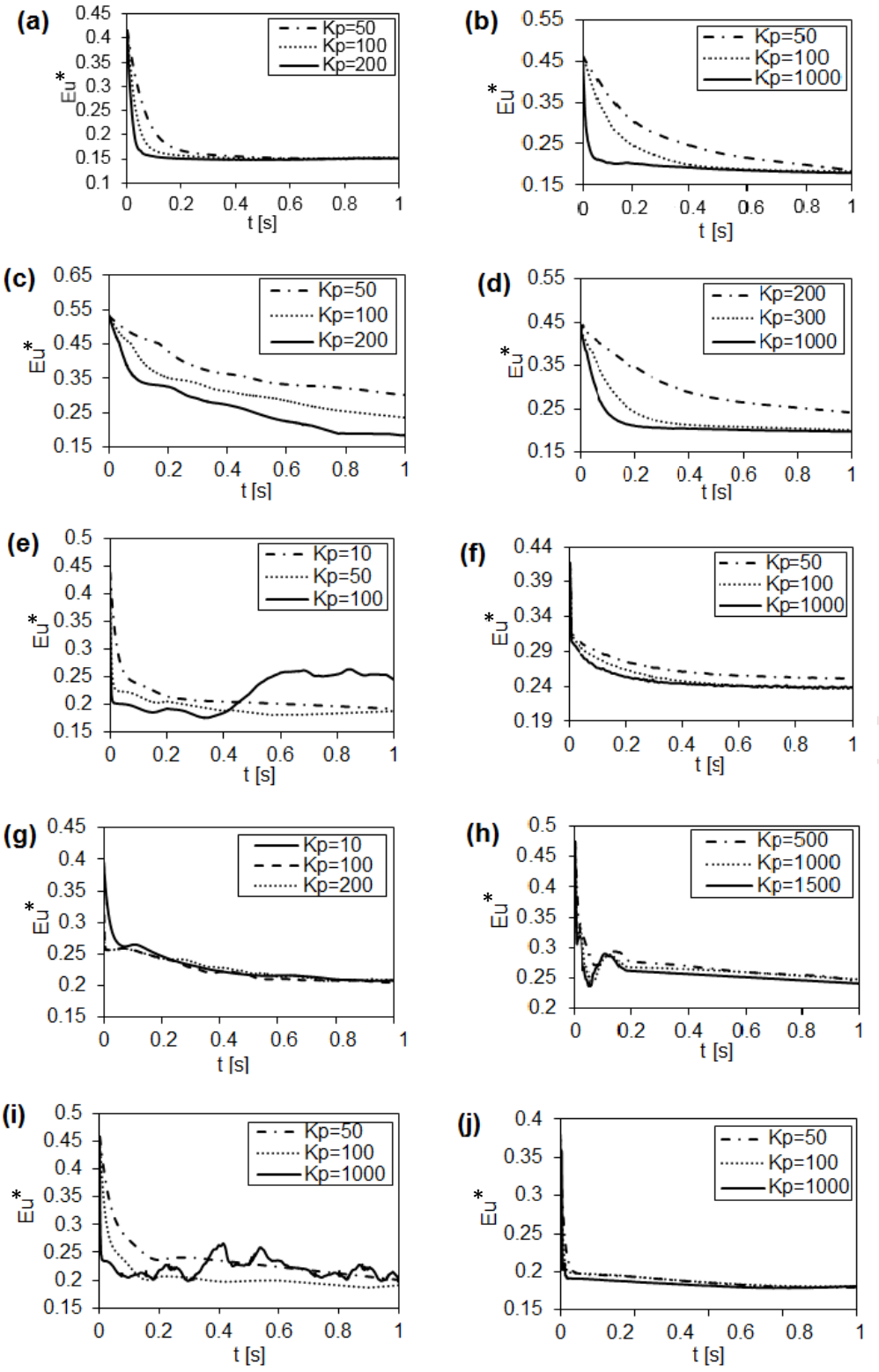

Fig. 4.3 Temporal changes of normalized velocity difference, E_u^* between PC-MRI measurement and CFD simulation with different proportional gain, K_p for each ten patient-specific aneurysms. (a) patient 1, (b) patient 2, (c) patient 3, (d) patient 4, (e) patient 5, (f) patient 6, (g) patient 7, (h) patient 8, (i) patient 9, and (j) patient 10.

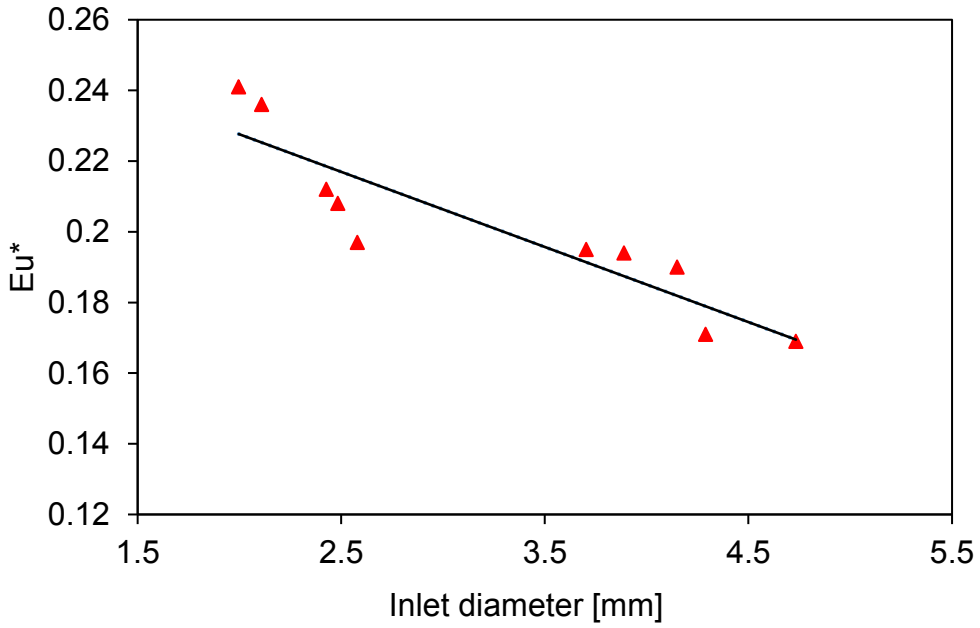

Fig. 4.4 Influence of vessel diameter on flow solution. These values of velocity difference E_u^* decreases as the inlet diameter of the vessel increases.

4.3.2 Effects of voxel meshes on pressure distribution

The pressure distribution on the voxel meshes at all discrete points of the interior domain of the vessels (for $VOF > 0.5$) was shown in Fig. 4.5. It was seen that a smoothed distribution without any unphysical acceleration was calculated even if the Cartesian type approach was used. The boundary pressure varies in each daughter branches that are shown at patient 2, patient 3, patient 6 and patient 8. However, the constant pressure distribution was obtained at patient 1, patient 4, patient 5, patient 7, patient 9 and patient 10 respectively. Usually, it was impossible to properly determine the boundary conditions only using the geometric information especially for an abnormal case such as a cerebral aneurysm because the physiological conditions might be changed from those of a normal case. In this regard, the present PFC-DA method automatically gives the boundary pressures.

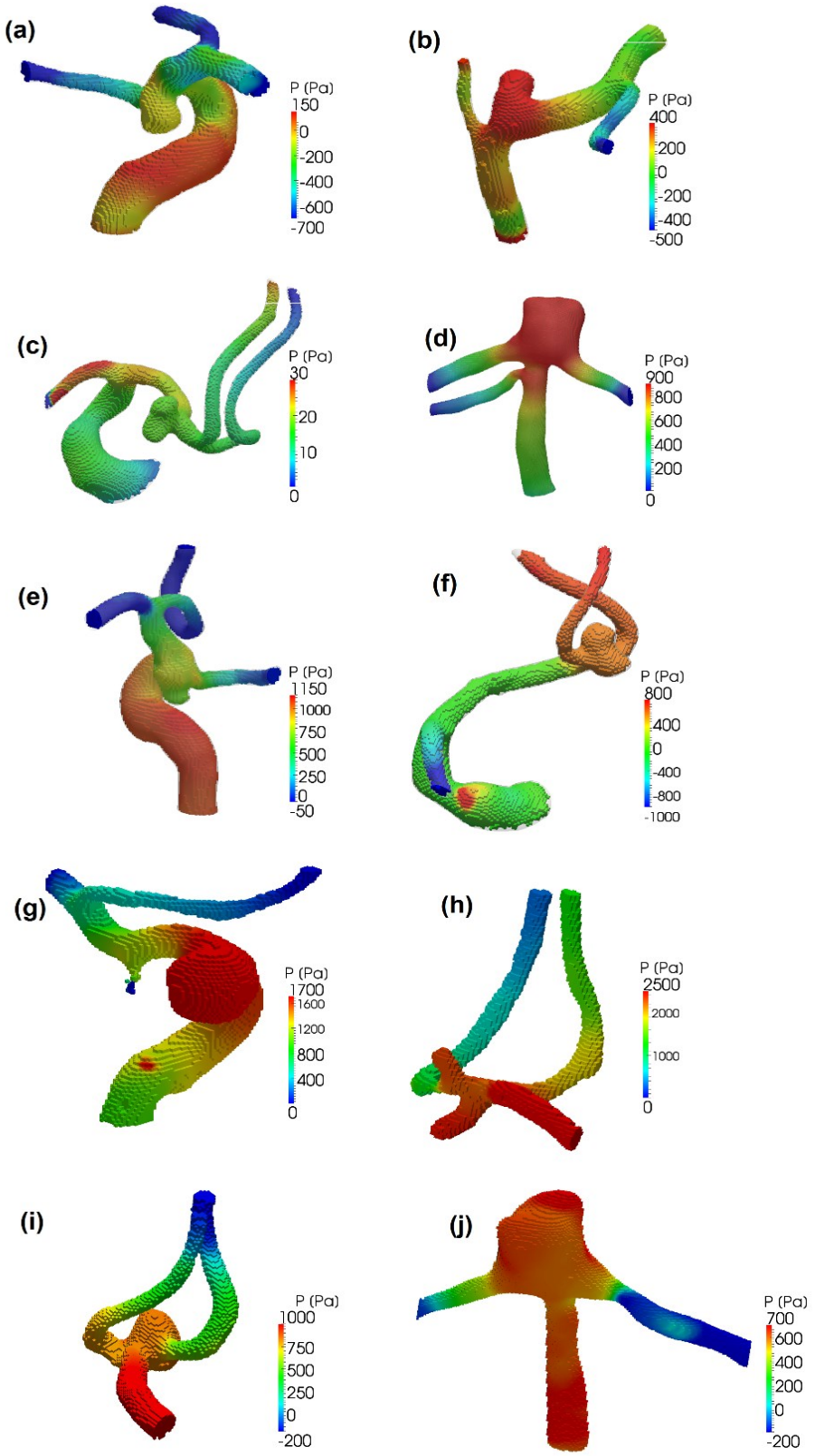

Fig. 4.5 Numerical solutions for the pressure distribution at every discrete points for *VOF* > 0.5 with ten patient-specific aneurysms. (a) patient 1, (b) patient 2, (c) patient 3, (d) patient 4, (e) patient 5, (f) patient 6, (g) patient 7, (h) patient 8, (i) patient 9, and (j) patient 10.

4.3.3 Overall behaviour of flow fields

Fig. 4.6 shows the velocity fields at the discrete points of the assimilated solution for all ten patient-specific aneurysms. It was seen that an overall behaviour of the assimilated velocity field at discrete points was shown that the smooth velocity profiles in the mother and daughter branches, including the aneurysm, where the flow was automatically separated into daughter branches by the estimated boundary pressures. These shows that the flow rate of the inlet vessel is well reproduced and properly divided into outlet branches. Since the CFD analysis can use higher resolution meshes than the measurement resolution, more detailed information on the flow field was obtained.

4.3.4 Detail information on wall shear stress (WSS)

In additional, we can evaluate the continuous WSS profile by using the velocity distribution obtained using the higher resolution computational meshes. Fig. 4.7 shows the WSS distribution, where it is constructed by the least-squares method using a surrounding set of the flow velocity on the Cartesian meshes. Again, it was confirmed that a smoothed profile was obtained even in the Cartesian mesh systems. In all patients, the WSS values inside the aneurysm were much smaller than that of the mother branch. However, a bit higher value was observed around the neck region of the aneurysm at patient 2, patient 5, patient 8, patient 9 and patient 10. The highest WSS was seen around a bifurcation area, especially distributed in the small artery that was attributed to the flow separation on the corner of outlet branches.

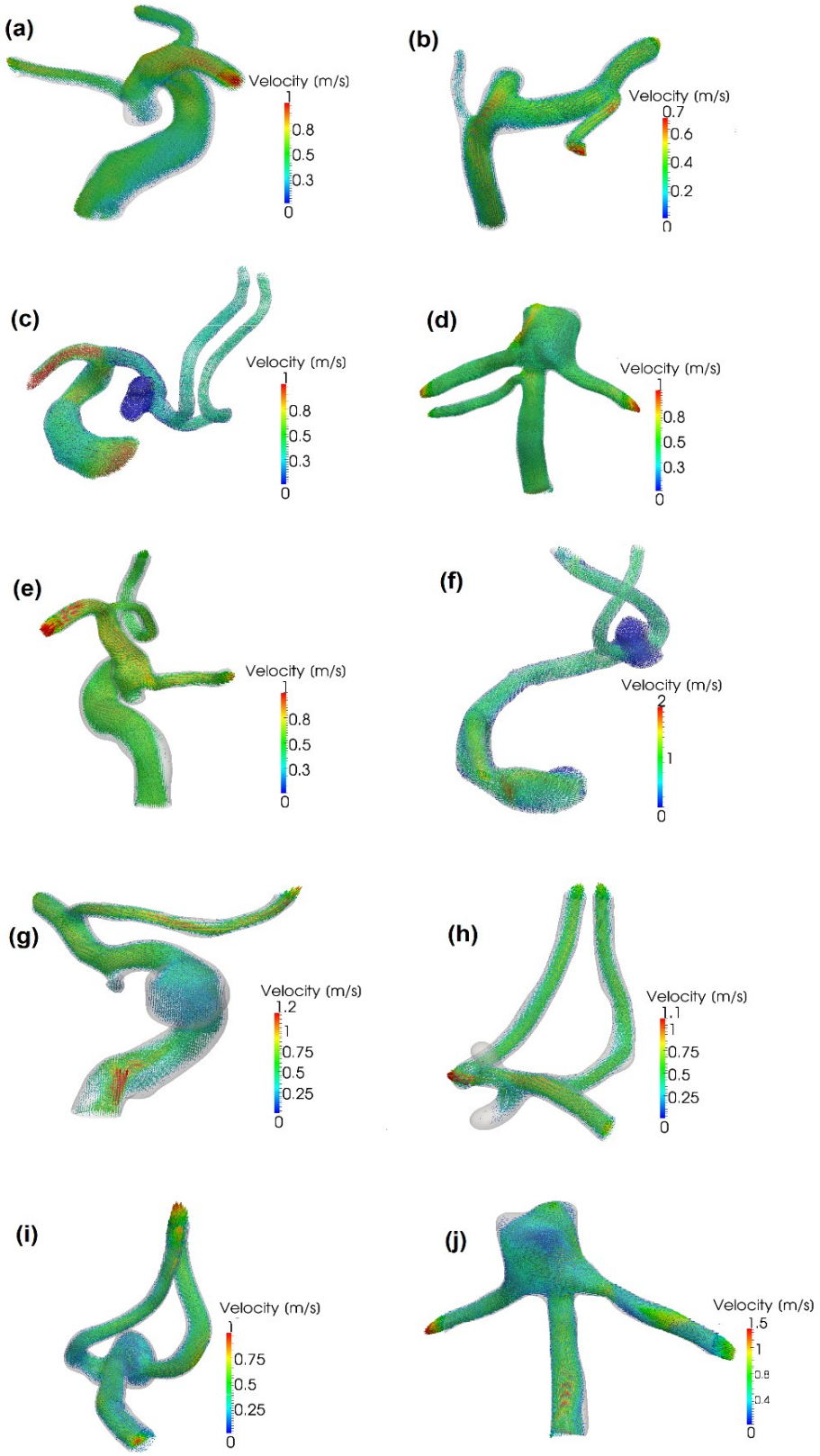

Fig. 4.6 Numerical solutions for the velocity at every discrete points for $VOF > 0.5$ with ten patient-specific aneurysms. (a) patient 1, (b) patient 2, (c) patient 3, (d) patient 4, (e) patient 5, (f) patient 6, (g) patient 7, (h) patient 8, (i) patient 9, and (j) patient 10.

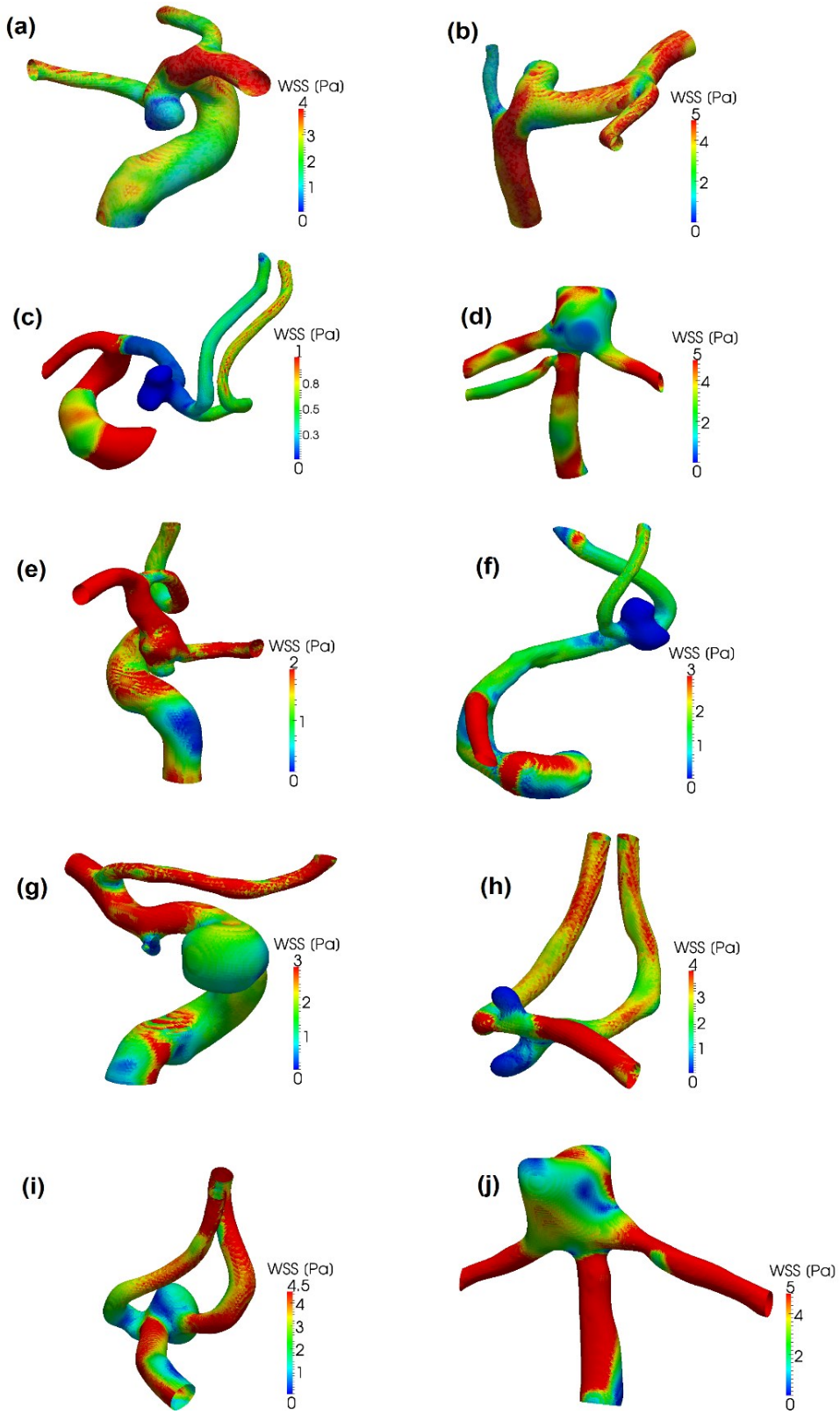

Fig. 4.7 The WSS values are evaluated based on the velocity distribution at each discrete points for ten patient-specific aneurysms. (a) patient 1, (b) patient 2, (c) patient 3, (d) patient 4, (e) patient 5, (f) patient 6, (g) patient 7, (h) patient 8, (i) patient 9, and (j) patient 10.

4.4 Summary

This chapter investigated the feasibility of the present PFC-DA method on patient-specific blood flow analysis for a cerebral aneurysm, using the PC-MRI velocity data. The feedback control approach was extended, with satisfying the physical consistency through the pressure boundary condition, which was evaluated by relaxing a misfit of velocity field between measurement and simulation.

In the investigation with a patient-specific aneurysm model, the assimilated flow field was in good agreement with the measurement flow field, where the velocity difference between measurement and simulation was reduced to less than 20% in systole condition. Moreover, a reasonable WSS distribution was reproduced. The information on hemodynamics (wall shear stress) and pressure field and also blood flow dynamics enables a better understanding of blood flow and would provide novel indices for diagnosis of cerebral diseases. In conclusion, this chapter clearly shows a feasibility of the present PFC-DA method for the simulation based patient-specific blood flow analyses on the cerebral aneurysm.

Chapter 5

Conclusions

This thesis presented a new concept of data assimilation method for reproducing an exact flow field by reducing the velocity difference between measurement and simulation with using all the velocity data obtained from PC-MRI measurement for patient-specific cerebral aneurysms. The effects of extracted geometry on blood flow field were evaluated to investigate the velocity difference between PC-MRI measurement and CFD simulation for patient-specific geometries in Chapter 2. The effects of boundary condition (outlet boundary) setup on flow solution were revealed in Chapter 3 through the investigation of the three difference boundary treatments; namely *P*-fixed approach, *Q*-control approach and *V*-optimized approach in minimizing the velocity difference between PC-MRI measurement and CFD simulation. Finally, toward the consideration to improve the *V*-optimized approach, Chapter 4 proposed the physically consistent feedback control based data assimilation (PFC-DA) method and investigated the feasibility of this method using patient-specific aneurysms. In the following context, this chapter provides a brief summary of each chapter, future works and emphasize the potential of the outcomes in this thesis.

In Chapter 2, the effects of extracted geometry on patient-specific aneurysm were examined by using the threshold determination method. These results demonstrated the volume and inlet area decrease as the C_{thres} value increases, and the WSS increases as the C_{thres} value increases. Interestingly, the minimum value of velocity difference between PC-MRI measurement and CFD simulation was obtained at C_{thres} value of 0.3 for both boundary

treatments; *P*-fixed and *Q*-control approach. According to this, the reconstructed vessel configuration strongly affects the flow characteristics.

To focus deeply on this relationship, Chapter 3 re-examined the CFD studies on minimizing the velocity difference between PC-MRI measurement and CFD simulation by introducing the basic framework; so-called velocity-field optimized (*V*-optimized) approach. The methodology remains same as Chapter 2. The results were compared with the *P*-fixed approach and *Q*-control approach and exhibited the significant reduction of velocity difference to 19.3% in *V*-optimized approach. The finding clearly confirmed that the differences in boundary treatments affected WSS value. However, this approach is tremendously expensive regarding computational cost because due to a combinatorial optimization with an exhaustive search is applied to find the optimal solution.

Chapter 4 proposed the novel physically consistent feedback control based data assimilation (PFC-DA) method to improve the *V*-optimized approach. The detail information of flow was successfully expressed through the feasibility study on this PFC-DA method. Through the numerical simulation for the 3D exact flow fields, along with a blood flow analysis on the real patient-specific cerebral aneurysm with actual PC-MRI velocity data, the results confirmed that the flow automatically separated into respective branches and with the higher resolution in the computational mesh provides the WSS profile.

The main achievement of this thesis is to develop a basic strategy to investigate the optimal solution of velocity difference between PC-MRI measurement and CFD simulation by using *V*-optimized approach and then improve it with the novel physically consistent feedback control based data assimilation (PFC-DA) method in order to reduce the computational cost. The understanding of the effects of extracted geometry on flow field solution for a patient-specific aneurysm also has a huge potential to innovate the clinical assessment of the hemodynamics. **Fig. 5.1** illustrates a schematic of framework developed in this thesis.

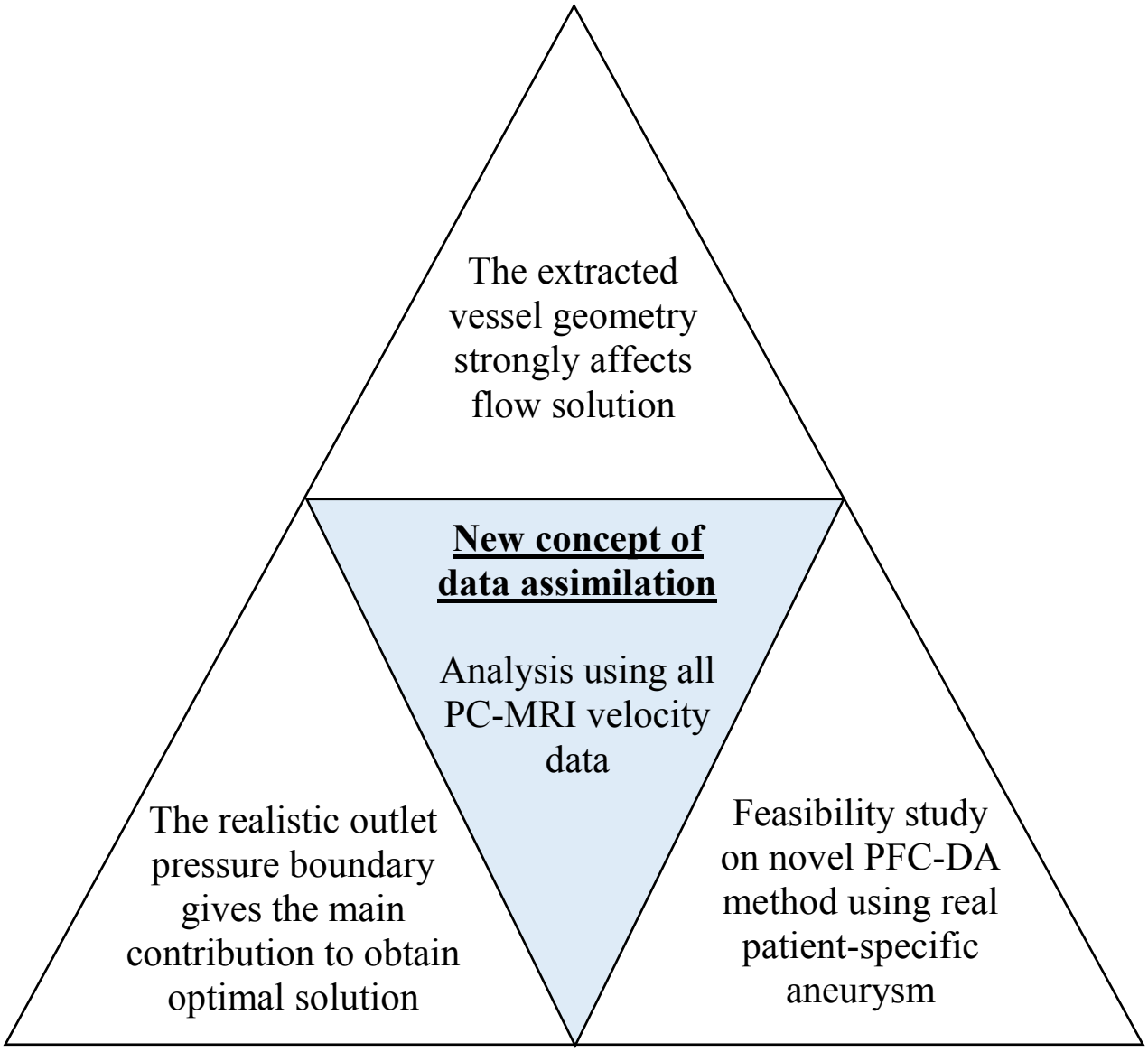

Fig. 5.1 Schematic of the new concept of data assimilation method framework for patient-specific aneurysm.

Patient-specific blood flow field was measurable by using medical imaging (PC-MRI), and then the flow characteristics can be evaluated with using correct vessel configuration and boundary condition (Chapter 2&3). However, due to the lack of measurement spatial resolution, the large of velocity difference was introduced. For further improvement on the *V*-optimized method in chapter 3, the novel data assimilation called PFC-DA method was introduced in Chapter 4.

This thesis not only revealed to reduce the velocity difference between PC-MRI measurement and CFD simulation on the global and local blood flow fields in the patient-specific cerebral aneurysm but also developed the new concept in computational mechanics analysis by using all the PC-MRI velocity data. These achievements clearly exhibit a huge potential of the computational mechanics approach.

Appendix 1

Smoothing process for vascular geometry

The three-dimensional (3D) reconstruction of the patient-specific geometry was done using the AMIRA 5.4.2 (Visage Imaging, Berlin, Germany). The vessel surface was given by 3-D triangle meshes based on the unconstrained smoothing function of AMIRA 5.4.2. To reduce the remain spatial irregularity in the obtained surface meshes, a physics-based surface smoothing process was carried out, in which the stretching and bending resistance expressed by a spring network model [54] was applied to each edge of the mesh and pair of the adjacent meshes, respectively. The volume and surface area of the whole aneurysm geometries between the vessel geometries prior and after smoothing process were evaluated and confirmed that both changes were less than 2 %.

The conceptual diagram of the spring network is shown in Fig. A1.1. A linear spring was defined on each side of the triangle, a bending spring was defined between adjacent elements, potential energy was obtained for each, and the force applied to each node was calculated according to the principle of energy minimization. By solving the equation of motion at each node positively, we deformed the shape dynamically to an optimum shape. The elastic energy of each side of the triangular element constituting the shape

$$W_D = \sum_{l=1}^{N_l} \frac{1}{2} k_d (L_l - L_{l0})^2 \tag{A1.1}$$

Here, N_l is the total number of sides, L_{l0} is the initial length of the spring, L_l is the spring length after deformation, and k_d is the spring constant. The bending elastic energy stored in the entire shape due to the angular change between the adjacent elements is defined as 0^0,

$$W_B = \sum_{b=1}^{N_b} \frac{1}{2} k_B L_B \tan^2\left(\frac{\theta_b}{2}\right) \tag{A1.2}$$

Here, N_b is the total number of bending springs, k_B is the bending spring constant, L_B is the length of the side connecting adjacent elements, and θ_b is the angle between the elements. In addition, the force applied to an arbitrary node by the internal pressure is defined as the sum of the pressures applied to the element including the node,

$$\mathbf{F}_B = \sum_{j=1}^{N_j} \frac{PA_j}{3} \mathbf{n}_j \tag{A1.3}$$

j is the element containing the node, P is the pressure, A is the area of the element, and **n** is the normal vector of the element.

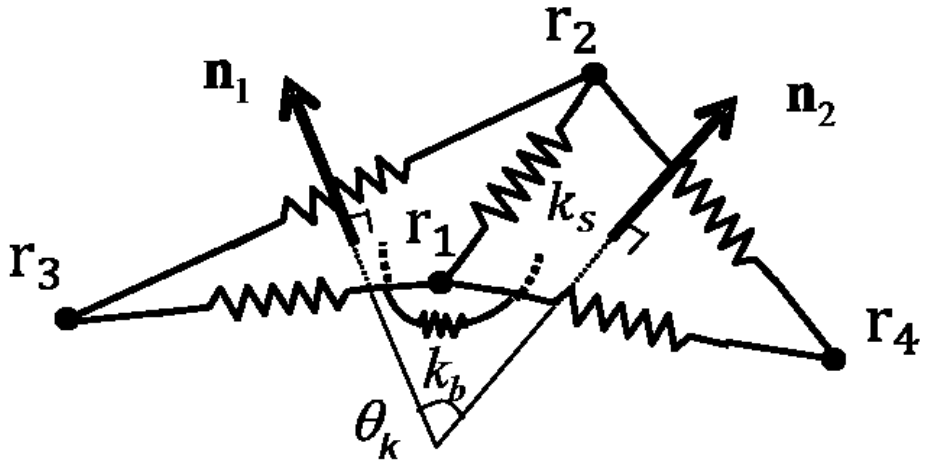

Fig. A1.1 Schematic of spring network model.

From the principle of energy minimization, the equation of motion of the node is

$$m\ddot{\mathbf{r}} + \eta\dot{\mathbf{r}} = -\frac{\partial(W_D + W_B)}{\partial \mathbf{r}} + \mathbf{F}_B \tag{A1.3}$$

By explicitly solving this equation and evolving time, we changed it to a dynamically optimal shape. Fig. A1.2 shows the mesh of 10 actual patient-specific aneurysm model with three-dimensional construction from DSA image and smoothing process.

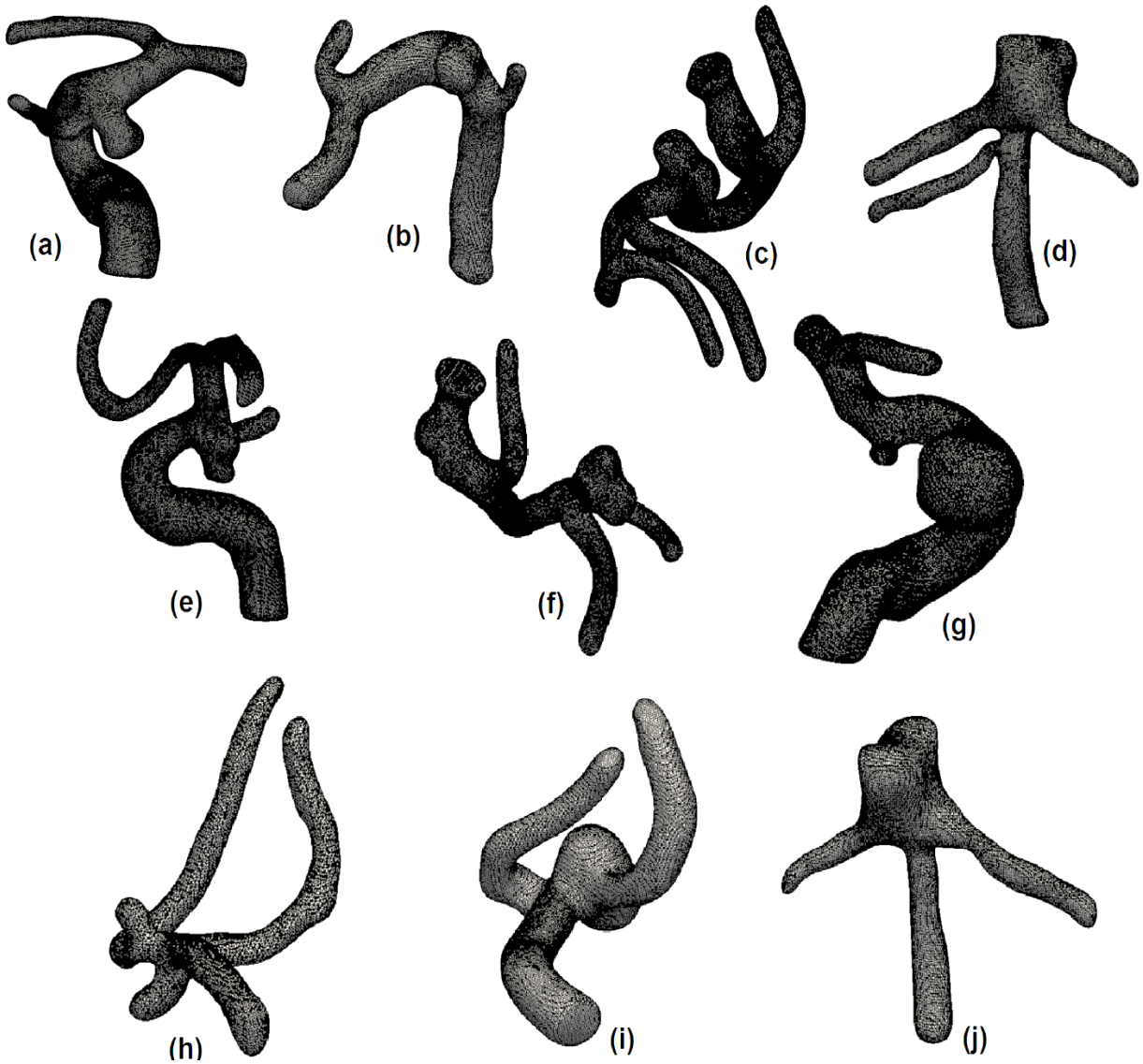

Fig. A1.2 Geometry of patient-specific aneurysm models after smoothing process. (a) Patient 1, (b) Patient 2, (c) Patient 3, (d) Patient 4, (e) Patient 5, (f) Patient 6, (g) Patient 7, (h) Patient 8, (i) Patient 9 and (j) Patient 10.

Appendix 2

Registration of three-dimensional shape between DSA and PC-MRI models

A2.1 Introduction

In order to investigate the velocity field obtained in the CFD analysis and the PC-MR image, two different 3D shapes of vessel model used in the CFD analysis are corresponded from the voxels acquired from the PC-MR image. Therefore, two different 3D models are registered by using an Iterative Closest Point (ICP) algorithm [35] which is widely used as a basic method of alignment between two models.

A2.2 Methodology

The DSA model used in the CFD analysis is aligned to PC-MRI model by using the ICP algorithm. For the convenience of formulation, the surface of each DSA model is divided by mesh. The PC-MRI model extracts only the outermost voxel and places a point on the surface of the outer voxel. Fig. A2.1 (*left*) shows the initial position relationship between DSA model and PC-MRI model. For example, the number of nodes in DSA model is N_P = 40, 511, and the number of nodes in the PC- MRI model is N_X = 1,692. The geometric transformation estimated by the ICP algorithm is a three-dimensional rigid body transformation belonging to the 3D special SE group [55]. In the ICP algorithm, the rotation is set to the q unit,

$$\vec{q}_R = [q_0\ q_1\ q_2\ q_3]^{\mathrm{t}}\ (q_0 \geq 0,\ \ q_0^2 + q_1^2 + q_2^2 + q_3^2 = 1) \qquad \text{(A2.1)}$$

We used the seven-dimensional variable $\vec{q}_T = [q_4\ q_5\ q_6\ ]^{\mathrm{t}}$ combined with the translation vector $\vec{q} = [\vec{q}_R \mid \vec{q}_T]^{\mathrm{t}}$. The ICP algorithm estimates the three-dimensional rigid body motion transformation and aligns the DSA model to the PC-MRI model by iterative computation and alternates the correspondence by the nearest neighbor point and the estimation process of the geometric transformation from the corresponding point (see Fig. A2.1 (*right*)).

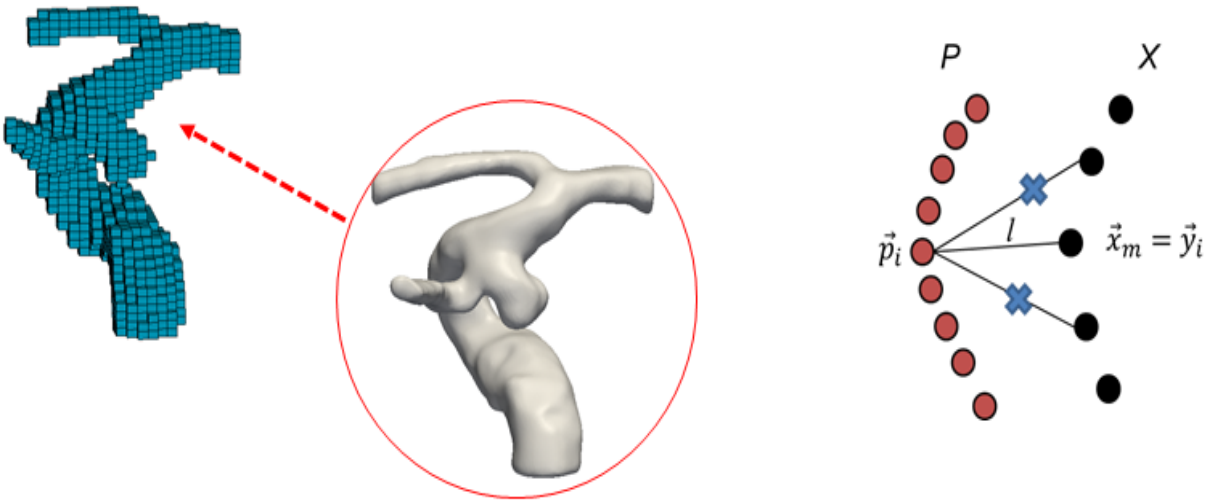

Fig. A2.1 *Left:* Initial position between DSA vessel model (white) and PC-MRI model (blue). *Right*: Diagram of determination of the nearest point. Both DSA and PC-MRI model shows patient 1.

A2.2.1 Mapping by nearest neighbor

A point closest to the PC-MRI (set as *X*) model is associated with the data point belonging to the DSA model. A conceptual diagram of correspondence by the nearest neighbor is shown in Fig. A2.1 (*right*). The distance, *x* from the point p_i to the PC-MRI model is set as

$$l(\vec{p},\ X) = \min_{\vec{x}\in X}\|\vec{x} - \vec{p}_i\| \tag{A2.2}$$

points in the PC-MRI model which are closest to the point of the DSA model,

$$\vec{y}_i = \operatorname{argmin}_{\vec{x}\in X}\|\vec{x} - \vec{p}_i\| \tag{A2.3}$$

Let set of *Y*, then found for each point in *P*. This processing was performed by using the operator *C* for obtaining the nearest neighbor point,

$$Y = C(P,\ X) \tag{A2.4}$$

A2.2.2 Estimation of geometry transformation to corresponding points

It is possible to solve the rigid body motion conversion that minimizes the square error of the sets *P* and *Y* in the correspondence relationship. The least squares solution $\vec{q}$ of the geometry transformation was performed to pairs the point of *P* and *Y*. Then it was minimized the square error *d,* where obtained by using the operator *Q*,

$$(\vec{q},\ d) = Q(P,\ Y) \tag{A2.5}$$

for center vectors $\vec{\mu}_p$, $\vec{\mu}_y$ *y* for sets *P* and *Y* correspondence to

$$\vec{\mu}_p = \frac{1}{N}\sum_{i=1}^{N}\vec{p}_i\ ,\quad \vec{\mu}_y = \frac{1}{N}\sum_{i=1}^{N}\vec{y}_i \tag{A2.6}$$

where *N* was the number of points *P* and *Y*, $N = N_P = 40, 511$. Next, the covariance matrix as

$$\sum = \frac{1}{N}\sum_{i=1}^{N}\left[(\vec{p}_i - \vec{\mu}_p)(\vec{y}_i - \vec{\mu}_y)^{\mathrm{t}}\right] \tag{A2.7}$$

An antisymmetric component of this covariance matrix was expressed by

$$A_{ij} = (\sum_{ij} - \sum_{ij}^{\mathrm{t}}) \tag{A2.8}$$

The vector Δ was calculated using this antisymmetric component,

$$\Delta = [A_{23}, A_{31}, A_{12}]^{\mathrm{t}} \tag{A2.9}$$

the 4×4 matrix **Q** was obtained,

$$\mathbf{Q} = \begin{bmatrix} tr(\sum) & \Delta^{\mathrm{t}} \\ \Delta & \sum + \sum^{\mathrm{t}} - tr(\sum)\mathbf{I}_3 \end{bmatrix} \tag{A2.10}$$

Here, $\mathbf{I}_3$ was a 3×3 identity transform. The eigenvector of the largest eigenvalue matrix **Q** was $\vec{q}_R = [q_0\ q_1\ q_2\ q_3]^{\mathrm{t}}$ representing the optimal rotation, the rotation matrix $\mathbf{R}(\vec{q}_R)$

$$\mathbf{R}(\vec{q}_R) = \begin{bmatrix} q_0^2 + q_1^2 - q_2^2 - q_3^2 & 2(q_1q_2 - q_0q_3) & 2(q_1q_3 + q_0q_2) \\ 2(q_1q_2 + q_0q_3) & q_0^2 - q_1^2 + q_2^2 - q_3^2 & 2(q_2q_3 - q_0q_1) \\ 2(q_1q_3 - q_0q_2) & 2(q_2q_3 + q_0q_1) & q_0^2 - q_1^2 - q_2^2 + q_3^2 \end{bmatrix} \tag{A2.11}$$

From the rotation matrix and the center of gravity, the optimal translation vector

$$\vec{q}_T = \vec{\mu}_y - \mathbf{R}(\vec{q}_R)\vec{\mu}_p \tag{A2.12}$$

The least squares solution of geometric transformation was obtained as $\vec{q} = [\vec{q}_R \mid \vec{q}_T]^{\mathrm{t}}$. By applying the geometric transformation obtained here, the point $\vec{p}_i^{\,k}$ of the vessel model shape at the *k* step was obtained at the $k+1$ step,

$$\vec{p}_i^{\,k+1} = \mathbf{R}(\vec{q}_R)\vec{p}_i^{\,k} + \vec{q}_T \tag{A2.13}$$

The minimized squared error d^k

$$d^k = \frac{1}{N}\sum_{i=1}^{N}\left\|\vec{y}_i^{\,k} - \vec{p}_i^{\,k+1}\right\|^2 \tag{A2.14}$$

A2.2.3 Overall composition

In the ICP algorithm, it converges to the minimum solution which minimizes the squared error from the initially aligned model. However, in the case of having the local minimum solution, it does not necessarily converge to the optimal solution, so initial position matching is important. For the convergence judgment, the threshold value τ set to 1.0×10^{-8}, and the ICP algorithm is terminated when $d^k - d^{k+1} < \tau$. A flowchart of the ICP algorithm is shown in Fig. A2.2.

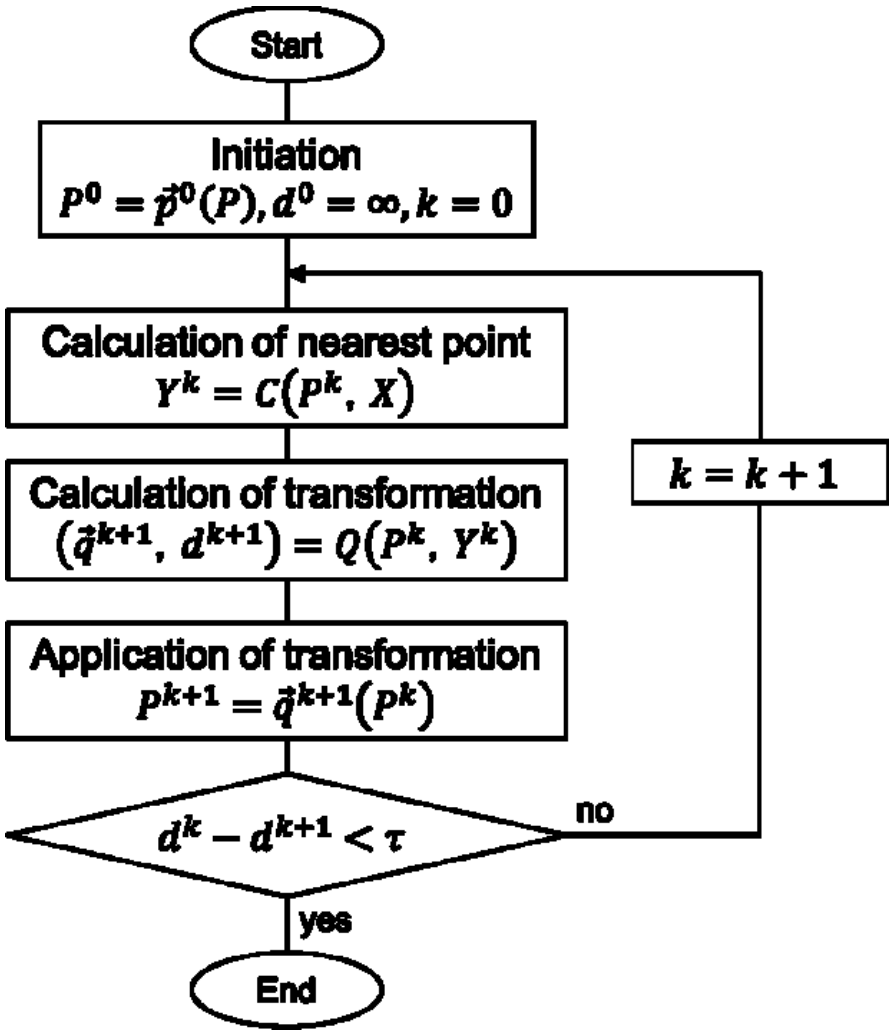

Fig. A2.2 Flowchart of the ICP algorithm.

A2.3 Results and discussion

Fig. A2.3 shows the positional relationship between the DSA blood vessel model and the PC-MRI model after paring using ICP algorithm. We know that, although the approximate position of the two model matches after the initial alignment, a few overlapping parts were still remained. As shown in Fig. A2.3 (b), after executing the ICP algorithm, there are more overlapping parts than before execution. Fig. A2.4 shows the transition of the square error d when the ICP algorithm is executed after the initial position. It is found that the square error monotonously decreases as the step number k increases and converges.

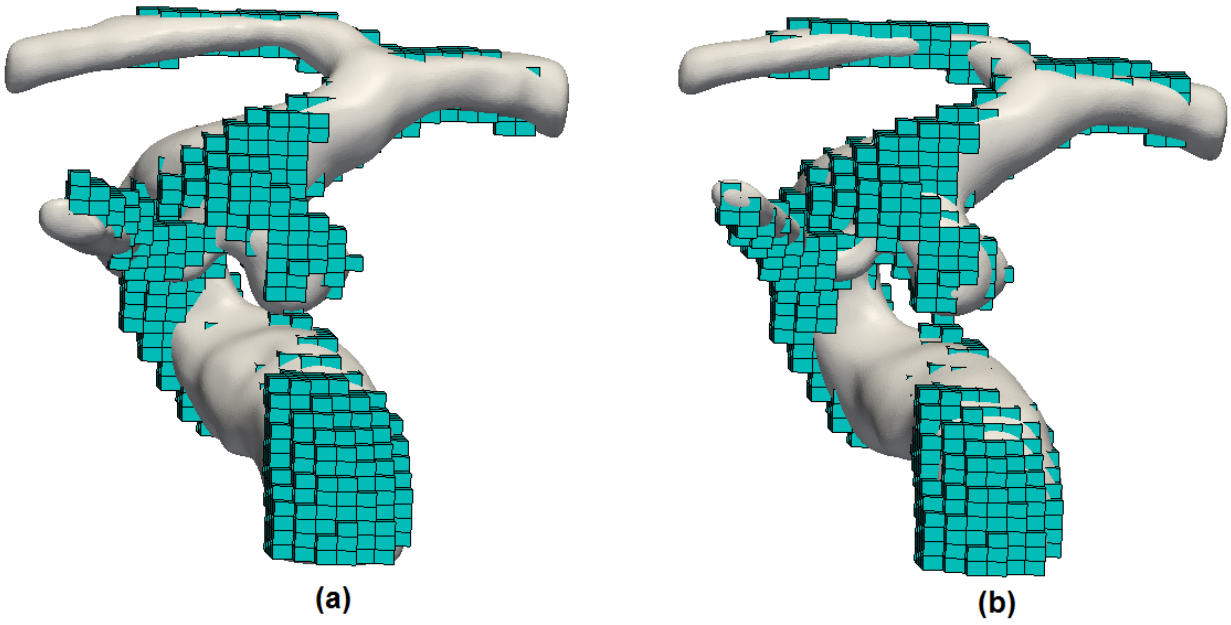

Fig. A2.3 (a) Position relation between the vessel model (blue) and the PC-MR model (white) with initial alignment. (b) Position relation between the vessel model (blue) and the PC-MRI model (white) after ICP algorithm with initial alignment.

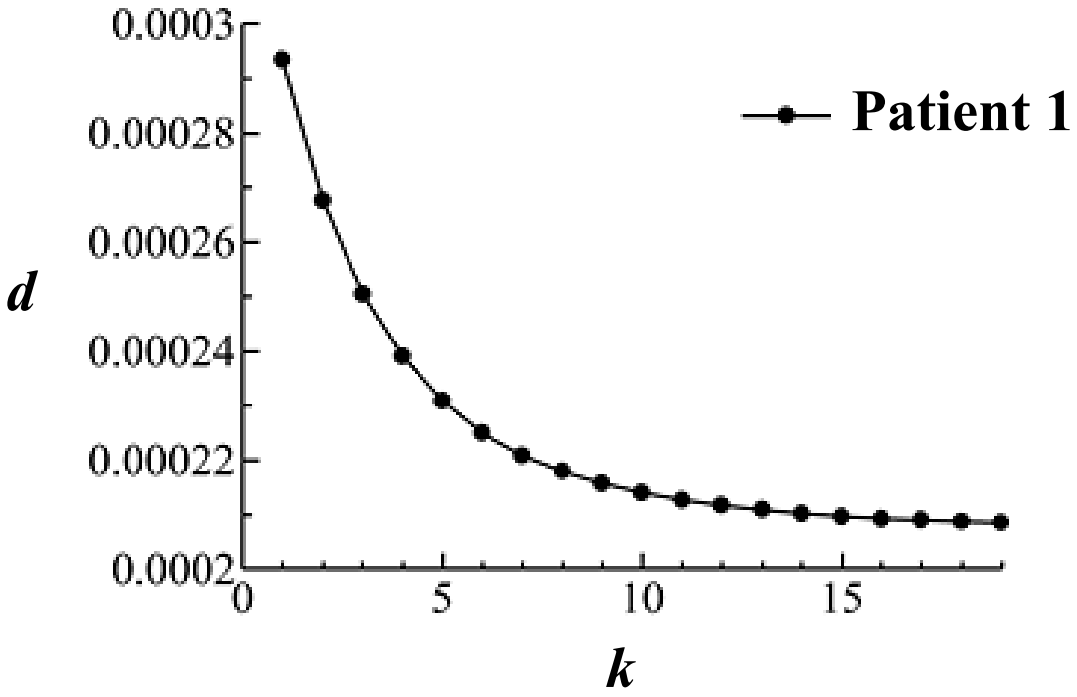

Fig. A2.4 Variation of the square error d. The result shows patient 1.

Appendix 3

Evaluation of velocity difference between CFD simulation and PC-MRI measurement

An average value of voxel mesh was obtained from PC-MRI by the Gauss quadrature method, in which the voxel center is inside the vessel, located far from the vessel surface. Then, define the coordinates of 8 Gaussian points (see Fig. A3.1 (a)) for the 4th-order Gaussian quadrature in each selected voxel, and obtain the velocity value from the CFD solutions using a quadratic interpolation with the moving least-squares method.

Fig. A3.1 (b) shows a diagram that schematically shows the relationship between measurement points and calculation points that fall within the influence radius. The approximate value $\mathbf{v}(x_j, y_j, z_j) = \mathbf{v}(x_0 + \tilde{x}_j, y_0 + \tilde{y}_j, z_0 + \tilde{z}_j)$ of the velocity vector at the point *j* falling within the influence radius satisfies, the velocity vector $\mathbf{v}_0$ at the measurement point (x_0, y_0, z_0). By using the second-order Taylor expansion

$$\begin{aligned}\mathbf{v}(x_j, y_j, z_j) &= \mathbf{v}(x_0 + \tilde{x}_j, y_0 + \tilde{y}_j, z_0 + \tilde{z}_j) \\ &= \mathbf{v}_0 + \mathbf{v}_{x0}\tilde{x}_j + \mathbf{v}_{y0}\tilde{y}_j + \mathbf{v}_{z0}\tilde{z}_j + \frac{1}{2}\mathbf{v}_{xx0}\tilde{x}_j^2 + \frac{1}{2}\mathbf{v}_{yy0}\tilde{y}_j^2 \\ &+ \frac{1}{2}\mathbf{v}_{zz0}\tilde{y}_j^2 + \mathbf{v}_{xy0}\tilde{x}_j\tilde{y}_j + \mathbf{v}_{yz}\tilde{y}_j\tilde{z}_j + \mathbf{v}_{zx0}\tilde{z}_j\tilde{x}_j\end{aligned} \tag{A3.7}$$

v is the velocity vector at Cartesian coordinates *(x, y, z).* The lower right *j* is the index of the element falling within the influence radius, and the lower right of $\mathbf{v}_0$ represents the partial differentiate variable. Generally,

$$\mathbf{v}_{n0} = \left.\frac{\partial \mathbf{v}}{\partial n}\right|_0, \quad \mathbf{v}_{mn0} = \left.\frac{\partial^2 \mathbf{v}}{\partial m \partial n}\right|_0, \quad (n, m = x, y, z) \tag{A3.8}$$

Also, $\tilde{x}_j, \tilde{y}_j, \tilde{z}_j$ are the difference in *x*, *y, z* coordinate from the point of interest. To make the weighting function bigger near to the point of interest and smaller at the distant position,

$$w(r_j) = \begin{cases} \dfrac{1}{2r_e}\left\{1 + \cos\left(\dfrac{\pi r_j}{r_e}\right)\right\} & (r_j \le r_e) \\ 0 & (r_j > r_e) \end{cases} \tag{A3.9}$$

Here, r_e is the influence radius, and r_j is the distance between the point of interest. We assumed the number of points *j* falling within the influence radius is N_{in}, where the evaluation function obtained by multiplying the approximate value of the velocity vector and weighting function,

$$\begin{aligned} E(\mathbf{v}_0, \mathbf{v}_{x0}, \mathbf{v}_{y0}, \mathbf{v}_{z0}\mathbf{v}_{xx0}, \mathbf{v}_{yy0}, \mathbf{v}_{zz0}, \mathbf{v}_{xy0}, \mathbf{v}_{yx0}, \mathbf{v}_{zx0}) &= \frac{1}{2}\sum_{j=1}^{N_{in}} w(r_j)\left(\mathbf{v}(x_j, y_j, z_j) - \mathbf{v}_j\right)^2 \\ = \frac{1}{2}\sum_{j=1}^{N_{in}} w(r_j)\Big(\mathbf{v}_0 + \mathbf{v}_{x0}\tilde{x}_j + \mathbf{v}_{y0}\tilde{y}_j + \mathbf{v}_{z0}\tilde{z}_j + \frac{1}{2}\mathbf{v}_{xx0}\tilde{x}_j^2 + \frac{1}{2}\mathbf{v}_{yy0}\tilde{y}_j^2 + \frac{1}{2}\mathbf{v}_{zz0}\tilde{y}_j^2 + \mathbf{v}_{xy0}\tilde{x}_j\tilde{y}_j \\ + \mathbf{v}_{yz}\tilde{y}_j\tilde{z}_j + \mathbf{v}_{zx0}\tilde{z}_j\tilde{x}_j - \mathbf{v}_j\Big)^2 \end{aligned} \tag{A3.10}$$

Then, as a condition for minimizing the evaluation function *E*, we partially differentiated *E* becomes zero. For simplicity, we described the following based on the Einstein summary convention,

$$\begin{aligned} \frac{\partial E}{\partial \mathbf{v}_0} = w_j\mathbf{s}_j = 0\,, \quad \frac{\partial E}{\partial \mathbf{v}_{x0}} = w_j\tilde{x}_j\mathbf{s}_j = 0 \\ \frac{\partial E}{\partial \mathbf{v}_{y0}} = w_j\tilde{y}_j\mathbf{s}_j = 0\,, \quad \frac{\partial E}{\partial \mathbf{v}_{z0}} = w_j\tilde{z}_j\mathbf{s}_j = 0 \\ \frac{\partial E}{\partial \mathbf{v}_{xx0}} = \frac{1}{2}w_j\tilde{x}_j^2\mathbf{s}_j = 0\,, \quad \frac{\partial E}{\partial \mathbf{v}_{yy0}} = \frac{1}{2}w_j\tilde{y}_j^2\mathbf{s}_j = 0 \\ \frac{\partial E}{\partial \mathbf{v}_{zz0}} = \frac{1}{2}w_j\tilde{z}_j^2\mathbf{s}_j = 0\,, \quad \frac{\partial E}{\partial \mathbf{v}_{xy0}} = w_j\tilde{x}_j\tilde{y}_j\mathbf{s}_j = 0 \end{aligned} \tag{A3.11}$$

$$\frac{\partial E}{\partial \mathbf{v}_{yz0}} = w_j \tilde{y}_j \tilde{z}_j \mathbf{s}_j = 0\,, \quad \frac{\partial E}{\partial \mathbf{v}_{zx0}} = w_j \tilde{z}_j \tilde{x}_j \mathbf{s}_j = 0$$

$$\mathbf{s}_j = \mathbf{v}_0 + \mathbf{v}_{x0}\tilde{x}_j + \mathbf{v}_{y0}\tilde{y}_j + \mathbf{v}_{z0}\tilde{z}_j + \frac{1}{2}\mathbf{v}_{xx0}\tilde{x}_j^2 + \frac{1}{2}\mathbf{v}_{yy0}\tilde{y}_j^2 + \frac{1}{2}\mathbf{v}_{zz0}\tilde{y}_j^2$$

$$+\mathbf{v}_{xy0}\tilde{x}_j\tilde{y}_j + \mathbf{v}_{yz}\tilde{y}_j\tilde{z}_j + \mathbf{v}_{zx0}\tilde{z}_j\tilde{x}_j - \mathbf{v}_j$$

Then calculated the matrix as,

$$\mathbf{AB} = \mathbf{C} \tag{A3.12}$$

$$\mathbf{B} = \begin{pmatrix} \mathbf{v}_0 \\ \mathbf{v}_{x0} \\ \mathbf{v}_{y0} \\ \mathbf{v}_{z0} \\ \mathbf{v}_{xx0} \\ \mathbf{v}_{yy0} \\ \mathbf{v}_{zz0} \\ \mathbf{v}_{xy0} \\ \mathbf{v}_{yx0} \\ \mathbf{v}_{zx0} \end{pmatrix}, \quad \mathbf{C} = \begin{pmatrix} w_j\mathbf{v}_j \\ w_j\tilde{x}_j\mathbf{v}_j \\ w_j\tilde{y}_j\mathbf{v}_j \\ w_j\tilde{z}_j\mathbf{v}_j \\ w_j\tilde{x}_j^2\mathbf{v}_j/2 \\ w_j\tilde{y}_j^2\mathbf{v}_j/2 \\ w_j\tilde{z}_j^2\mathbf{v}_j/2 \\ \tilde{x}_j\tilde{y}_j\mathbf{v}_j \\ \tilde{y}_j\tilde{z}_j\mathbf{v}_j \\ \tilde{z}_j\tilde{x}_j\mathbf{v}_j \end{pmatrix} \tag{A3.13}$$

Here,

$$d_1 = 1,\ \ d_2 = \tilde{x}_j,\ \ d_3 = \tilde{y}_j,\ \ d_4 = \tilde{z}_j,\ \ d_5 = \frac{1}{2}\tilde{x}_j^2,$$

$$d_6 = \frac{1}{2}\tilde{y}_j^2,\ \ d_7 = \frac{1}{2}\tilde{z}_j^2,\ \ d_8 = \tilde{x}_j\tilde{y}_j,\ \ d_9 = \tilde{y}_j\tilde{z}_j,\ \ d_{10} = \tilde{z}_j\tilde{x}_j \tag{A3.14}$$

The component of matrix **A** is expressed as [**A**] $k_l = w_j\, d_k\, d_l$. The velocity vector $\mathbf{v}_0$ at the point of interest is obtained by multiplying **C** by the inverse matrix of **A**.

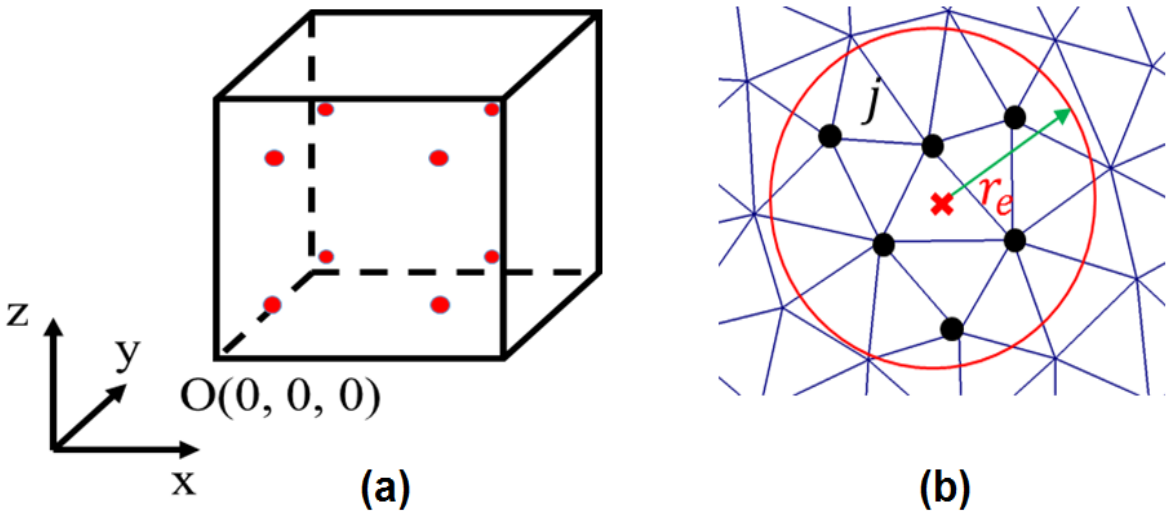

Fig. A3.1 (a) Gauss quadrature points with n=2 in a 3-dimesional voxel cell. (b) Schematic of the interpolation with the moving least-squares method, where the blue square, cross point and filled-circle indicate measurement points, the edge of voxel cell used in the PC-MRI measurement and discretization point in the CFD. j denotes an index of the measurement point and r_e denotes the influence radius of the interpolation.

The stencils for the interpolation are chosen to be in a radius approximately four times larger than the representative mesh size around the evaluation point in the CFD model. Finally, we calculated the average velocity in the CFD simulation on each voxel as **v** by for 4th-order Gaussian quadrature, using the below obtained discrete velocities at 8 Gaussian points as

$$
\begin{aligned}
(x_1, y_1, z_1) &= \left(\frac{L}{2}(1+1/\sqrt{3}), \frac{L}{2}(1+1/\sqrt{3}), \frac{H}{2}(1+1/\sqrt{3})\right), \\
(x_2, y_2, z_2) &= \left(\frac{L}{2}(1+1/\sqrt{3}), \frac{L}{2}(1+1/\sqrt{3}), \frac{H}{2}(1-1/\sqrt{3})\right), \\
(x_3, y_3, z_3) &= \left(\frac{L}{2}(1+1/\sqrt{3}), \frac{L}{2}(1-1/\sqrt{3}), \frac{H}{2}(1+1/\sqrt{3})\right),
\end{aligned}
\tag{A3.15}
$$

$$(x_4, y_4, z_4) = \left(\frac{L}{2}(1 + 1/\sqrt{3}), \frac{L}{2}(1 - 1/\sqrt{3}), \frac{H}{2}(1 - 1/\sqrt{3})\right),$$

$$(x_5, y_5, z_5) = \left(\frac{L}{2}(1 - 1/\sqrt{3}), \frac{L}{2}(1 + 1/\sqrt{3}), \frac{H}{2}(1 + 1/\sqrt{3})\right),$$

$$(x_6, y_6, z_6) = \left(\frac{L}{2}(1 - 1/\sqrt{3}), \frac{L}{2}(1 + 1/\sqrt{3}), \frac{H}{2}(1 - 1/\sqrt{3})\right),$$

$$(x_7, y_7, z_7) = \left(\frac{L}{2}(1 - 1/\sqrt{3}), \frac{L}{2}(1 - 1/\sqrt{3}), \frac{H}{2}(1 + 1/\sqrt{3})\right),$$

$$(x_8, y_8, z_8) = \left(\frac{L}{2}(1 - 1/\sqrt{3}), \frac{L}{2}(1 - 1/\sqrt{3}), \frac{H}{2}(1 - 1/\sqrt{3})\right)$$

where L is the vertical, and horizontal lengths of the voxel and H is the height of the voxel. Given that the velocity vector of the blood flow can be represented by the function $\mathbf{v}(x,y,z)$. The spatial average value of the voxel of $\mathbf{v}(x,y,z)$ is obtained from the velocity vector at the Gauss point of 8 points,

$$\frac{1}{L^2 H}\int_0^H \int_0^L \int_0^L \mathbf{v}(x,y,z)dxdydz \approx \frac{1}{8}\sum_{i=1}^{8} \mathbf{v}(x_i, y_i, z_i) \tag{A3.16}$$

Therefore, approximate values of velocity vectors in voxels can be obtained by the velocity vector $\mathbf{v}(x_i,y_i,z_i)$ at 8 Gauss points using the moving least squares approximation.

Appendix 4

PFC-DA method: numerical discretization based on projection type algorithm on fixed Cartesian mesh

The PDEs are spatially discretized by the finite difference method in a Cartesian mesh system. For coupling the velocity and pressure, we apply the fractional step method. In order to deal with an arbitrary geometry, we apply the *boundary data immersion method* (BDIM) with a few modifications. In the BDIM, the smoothed phase (or indicator) function is introduced to represent both the fluid and solid phases as

$$\chi(\mathrm{x}) = \begin{cases} 0, & \text{in solid domain } \Omega_s, \\ \epsilon(0,1), & \text{on transition layer } \Gamma_t, \\ 1, & \text{in fluid domain } \Omega_f, \end{cases} \tag{A4.1}$$

The governing equations hold in both the domains as

$$\begin{gathered} \rho(\partial_t \mathbf{v} + \mathbf{v} \cdot \nabla \mathbf{v}) = -\nabla p + \mu \nabla^2 \mathbf{v} \\ \nabla \cdot \mathbf{v} = 0 \end{gathered} \tag{A4.2}$$

The original BDIM integrates the momentum equation over time and derives a mixture form in the full domain by means of the phase mixing with the phase function χ. However, in this formula, a temporal discretization of the right-hand-side term is not reflected on the mixture, and thus a steady state solution includes a contribution of a discrete time increment Δt. Instead, we first derive a discrete form in time and then derive the mixture form. By applying the SMAC algorithm to (A4.2), we obtain semi-discrete equations in prediction phase:

$$\begin{cases} \rho\left(\dfrac{\mathbf{v}^* - \mathbf{v}^{\mathrm{n}}}{\Delta t} + \mathcal{A}^n(\mathrm{v})\right) = -\nabla p^n + \eta \nabla^2 \left(\dfrac{\mathbf{v}^{\mathrm{n}} + \mathbf{v}^*}{2}\right) & \text{in } \Omega_f, \\ \mathbf{v}^* = 0 & \text{in } \Omega_s, \end{cases} \tag{A4.3}$$

and in the projection phase:

$$\begin{cases} \rho \dfrac{\mathbf{v}^{n+1} - \mathbf{v}^*}{\Delta t} = -\nabla \delta p^{n+1} & \text{in } \Omega_f, \\ \mathbf{v}^{n+1} = \mathbf{v}^* & \text{in } \Omega_s, \end{cases} \tag{A4.4}$$

for $t \in [t^n, t^{n+1}]$ where $t^{n+1} = t^n + \Delta t$ and Δt is the time increment. Here, $\mathbf{v}^*$is the predicted (temporal) velocity, and δp^{n+1} is the pressure increment following

$$p^{n+1} = p^n + \delta p^{n+1} \tag{A4.5}$$

We apply the BDIM formulation in both the prediction and projection phases, respectively.

A4.1 Prediction phase

In (A4.3), we apply the second-order Adams-Bashforth method for the advection term $\mathcal{A}^n(\mathbf{v}) = (3\mathbf{v}^n \cdot \nabla \mathbf{v}^n - \mathbf{v}^{n-1} \cdot \nabla \mathbf{v}^{n-1})/2$ and the Crank-Nicolson method for the viscous term. Instead of updating the predicted velocity $\mathbf{v}^*$, we update the velocity increment $\delta \mathbf{v}^*$ satisfying

$$\mathbf{v}^* = \mathbf{v}^n + \delta \mathbf{v}^* \tag{A4.6}$$

Substituting (A4.6) into (A4.3), we obtain

$$\begin{cases} \mathcal{F}_{pre}(\delta \mathbf{v}^*): \delta \mathbf{v}^* = \left(\dfrac{\rho}{\Delta t} - \dfrac{\eta}{2}\nabla^2\right)^{-1} (-\rho \mathcal{A}^n(\mathbf{v}) - \nabla p^n + \eta \nabla^2 \mathbf{v}^n) & \text{in } \Omega_f \\ \mathcal{B}_{pre}(\delta \mathbf{v}^*): \delta \mathbf{v}^* = -\mathbf{v}^n & \text{in } \Omega_s \end{cases} \tag{A4.7}$$

In the BDIM method, the meta equation $\mathcal{M}_{pre}$ is derived by the phase mixing of the governing field equations, $\mathcal{F}_{pre}$ and $\mathcal{B}_{pre}$ with the phase function χ,

$$\mathcal{M}_{pre}(\delta \mathbf{v}^*) = \chi \mathcal{F}_{pre}(\delta \mathbf{v}^*) + (1 - \chi)\mathcal{B}_{pre}(\delta \mathbf{v}^*) \tag{A4.8}$$

From (A4.8) with (A4.7), we obtain

$$\delta \mathbf{v}^* = \chi \left(\frac{\rho}{\Delta t} - \frac{\eta}{2}\nabla^2\right)^{-1} (-\rho \mathcal{A}^n(\mathbf{v}) - \nabla p^n + \eta \nabla^2 \mathbf{v}^n) - (1 - \chi)\mathbf{v}^n \tag{A4.9}$$

$$\begin{cases} \delta\mathbf{v}^* = \chi\delta\mathbf{e} - (1-\chi)\mathbf{v}^n \\ \delta\mathbf{e} \equiv \left(\frac{\rho}{\Delta t} - \frac{\eta}{2}\nabla^2\right)^{-1}(-\rho\mathcal{A}^n(\mathbf{v}) - \nabla p^n + \eta\nabla^2\mathbf{v}^n) \end{cases} \tag{A4.10}$$

in the full domain Ω. Here δe is the auxiliary variable. Using the definition (A4.6), we finally obtain the system in the prediction phase as follows

$$\left(\frac{\rho}{\Delta t} - \frac{\eta}{2}\nabla^2\right)\delta\mathbf{e} = -\rho\mathcal{A}^n(\mathbf{v}) - \nabla p^n + \eta\nabla^2\mathbf{v}^n \tag{A4.11}$$

$$\mathbf{v}^* = \chi(\mathbf{v}^n + \delta\mathbf{e}) \tag{A4.12}$$

in Ω. Boundary conditions are given at a current time t^n and temporal time t^*, and thus, for the auxiliary variable $\delta\mathbf{e}$, they are evaluated by using the relation (A4.12). For the inlet/outlet pressure related to the scalar potential ϕ, we will describe later.

A4.2 Projection phase

From (A4.4), we also derive the meta equation by the phase mixing of the governing field equations defined in both the fluid and solid phases as follows

$$\begin{cases} \mathcal{F}_{pro}(\mathbf{v}^{n+1}) : \mathbf{v}^{n+1} = \mathbf{v}^* - \frac{\Delta t}{\rho}\nabla\delta p^{n+1} & \text{in } \Omega_f \\ \mathcal{B}_{pro}(\mathbf{v}^{n+1}) : \mathbf{v}^{n+1} = \mathbf{v}^* & \text{in } \Omega_s \end{cases} \tag{A4.13}$$

Analogously, we obtain the meta equation in the full domain $\mathcal{M}_{pro}(\mathbf{v}^{n+1}) = \chi\mathcal{F}_{pro}(\mathbf{v}^{n+1}) + (1-\chi)\mathcal{B}_{pro}(\mathbf{v}^{n+1})$ that offers

$$\mathbf{v}^{n+1} = \mathbf{v}^* - \frac{\Delta t}{\rho}\chi\nabla\delta p^{n+1} \tag{A4.14}$$

In order to satisfy the continuity equation at the next time t^{n+1}, i.e. $\nabla\cdot\mathbf{v}^{n+1} = 0$, we obtain the pressure increment δp^{n+1} by solving the following Poisson equation:

$$\nabla\cdot(\chi\nabla\delta p^{n+1}) = \frac{\rho}{\Delta t}\nabla\cdot\mathbf{v}^* \tag{A4.15}$$

with the boundary condition

$$\begin{cases} \partial_n \delta p^{n+1} = 0 & \text{on } \Gamma_w \\ \delta p^{n+1} = 0 & \text{on } \Gamma_{in}, \quad \Gamma_{out} \end{cases} \tag{A4.16}$$

A4.3 Scalar potential field

We suppose that the reference velocity set is discretely obtained in the domain, where the set of reference data consists of coordinate points $\mathbf{X}_m$ and point-wise velocity $\mathbf{U}_m$ for $m = \epsilon [1, M]$ (M is the total number of reference data). At current time step t^n for the discrete point $\mathbf{X}_m$, the discrete deviation $\mathbf{E}_m^n$ and signal $\mathbf{F}_m^n$ are evaluated by

$$\mathbf{E}_m^n = \mathbf{U}_m - \mathbf{V}_m^n \tag{A4.17}$$

$$\mathbf{F}_m^n = \mathbf{E}_m^n \tag{A4.18}$$

For $m = \epsilon [1, M]$, where $\mathbf{V}_m^n$ is the solved flow velocity $\mathbf{v}^n$ at reference points $\mathbf{X}_m$, i.e., $\mathbf{V}_m^n = \mathrm{v}^n(\mathbf{X}_m)$. Generally, since the reference points do not always correspond to the discrete points on the fluid meshes, we apply an interpolation technique with the smoothed delta function commonly used in the immersed boundary method:

$$\mathbf{V}_m^n = \int \delta^{(3)}(\mathbf{x} - \mathbf{X}_m)\, \mathbf{v}^n(\mathrm{x}) d\mathrm{x} \tag{A4.19}$$

Analogous to the interpolation, we need to extrapolate the continuous one $\mathbf{f}^n(\mathbf{x})$ from the discrete signal $\mathbf{F}_m^n$ in a fluid space. We again employ the smoothed delta function as a kernel to extrapolate the continuous signal, i.e.,

$$\mathbf{f}^n(\mathbf{x}) = h_x h_y h_z \sum_{m=1}^{M} \delta^{(3)}(\mathbf{x} - \mathbf{X}_m)\mathbf{F}_m^n \tag{A4.20}$$

Now the spatially continuous signal (or source) $\mathbf{f}^n$ at current time t^n is evaluated, we derive a mixture form for the poisson equation of the scalar potential ϕ. We take the phase mixing that leads to

$$\chi\nabla^2\phi^n = -\chi\nabla\cdot(\chi\mathbf{f}^n) \tag{A4.21}$$

Consequently, we can obtain the scalar potential field $\phi^n(\mathrm{x})$ by solving

$$\nabla\cdot(\chi\nabla\phi^n) = -\nabla\cdot(\chi\mathbf{f}^n) \tag{A4.22}$$

in the full domain with the Neumann boundary conditions. It should be noted that (A4.22) is solved with the Neumann boundary conditions, and thus the solution is allowed to have an indeterministic constant shift. In this study, we employ a constraint:

$$\frac{1}{\Omega}\int_\Omega \phi dx = 0 \tag{A4.23}$$

By using the scalar potential ϕ^n on the inlet and outlet boundaries, we can evaluate the inlet and outlet pressures (including the spatial distribution) to solve the equation (A4.11) in the prediction phase, that is

$$-p^n + \mu\partial_n\left(\frac{\mathbf{v}^n - \mathbf{v}^*}{2}\right) = -\phi^n \qquad \text{on } \Gamma_{in}, \Gamma_{out} \tag{A4.24}$$

Briefly summarize the solution algorithm for $t \in [t^n; t^{n+1}]$ as follows:

1. Interpolate the fluid velocity $\mathbf{V}^n_m$ at reference points using (A4.19)
2. Evaluate the discrete signal $\mathbf{F}^n_m$ using (A4.18) with (A4.17)
3. Extrapolate the continuous signal $\mathbf{f}^n$ using (A4.20)
4. Solve the Poisson equation for the scalar potential ϕ^n using (A4.22)
5. Solve the prediction equation for the predicted velocity **v*** using (A4.11) and (A4.12)
6. Solve the Poisson equation for the pressure increment $^{\delta}p^{n+1}$ using (A4.15)
7. Update the velocity $\mathbf{v}^{n+1}$ in the projection phase using (A4.14) and pressure $pn+1$ using (A4.5)

REFERENCES

[1] J.V. Gijn, G.J.E. Rinkel, "Subarachnoid hemorrhage: Diagnosis, causes and management," *Brain,* vol. 124, pp. 249-78, 2001.

[2] X. Liu, Z. Gao, H. Xiong, D. Ghista, L. Ren, H. Zhang, W. Wu, W. Huang, W.K. Hau, "Three-dimensional hemodynamics analysis of the circle of Willis in the patient-specific nonintegral arterial structures," *Biomech Model Mechanobiol.,* vol. 15, pp. 1439-1456, 2016.

[3] M.H.M. Vlak, A. Alga, R. Brandenburg, G.J.E. Rinkel, "Prevalence of unrupture intracranial aneurysms with emphasis on sex, age, comorbidity, country and time period; a systematic review and meta-analysis," *Lancet Neurol.,* vol. 7 pp. 626-36, 2011.

[4] J.P. Greving, J.H. Wermer, R.D. Broen, A. Morita, S. Juvela, M. Yonekura, T. Ishibashi, J.C. Toner, T. Nakayama, G.J.E. Rinkel, GJE, A. Algra, "Development of the PHASES score for prediction of risk of rupture of intracranial aneurysms: apooled analysis of six propective cohort studies," *Lancet Neurol.,* vol. 13, pp. 59-66, 2014.

[5] A. Morita, S. Fujiwara, K. Hashi, H. Ohtsu, T. Kirino, "Risk of rupture associated with intact cerebral aneurysms in the Japanese population: a systematic review of the literature from Japan," *J. Neurosurg.,* vol. 102, pp. 601-606, 2005.

[6] W. Stehbens, "Etiology of intracranial berry aneurysms," *J. Neurosurg.*, vol. 70, pp. 823-831, 1989.

[7] M.A. Castro, C.M. Putman, M.J. Sheridan, J.R. Cebral, "Hemodynamic patterns of anterior communicating artery aneurysms: A possible association with rupture," *Am. J. Neuroradiol.,* vol. 30, pp. 297–302, 2009.

[8] M. Shojima, M. Oshima, K. Takagi, R. Torii, M. Hayakawa, K. Katada, A. Morita, T. Kirino, "Magnitude and role of wall shear stress on cerebral aneurysm: Computational fluid dynamic study of 20 middle cerebral artery aneurysms," *Stroke*, vol. 35, pp. 2500-2505, 2004.

[9] P. Venugopal, D. Valentino, H. Schmitt, J. Villablanca, F. Vinuela, G. Duckwiler, "Sensitivity of patient-specific numerical simulation of cerebral aneurysm hemodynamics to inflow boundary conditions," *J. Neurosurg.*, vol. 106, pp. 1051–1060, 2007.

[10] P.R. Moran, "A flow velocity zeugmatographic interlace for NMR imaging in humans," *Magn. Reson. Imaging,* vol. 1, pp. 197-203, 1982.

[11] D.J. Bryant, J.A. Payne, D.N. Firmin, "Measurement of flow with NMR imaging using a gradient pulse and phase difference technique," *J. Comput. Assist. Tomogr.,* vol. 8, pp. 588-93, 1984.

[12] G.L. Nayler, D.N. Firmin, D.B. Longmore, "Blood flow imaging by cine magnetic resonance," *J. Comput. Assist. Tomogr.,* vol. 10, pp. 715-22, 1986.

[13] P.J. Kilner, G.Z. Yang, R.H Mohiaddin, "Helical and retrograde secondary flow patterns in the aortic arch studied by three-directional magnetic resonance velocity mapping," *Circulation,* vol. 88, pp. 2235-47, 1993.

[14] L. Wigstrom, T. Ebbers, A. Fyrenius, "Particle trace visualization of intracardiac flow using time-resolved 3D phase contrast MRI," *Magn. Reson. Med.* vol. 41, pp. 793-9, 1999.

[15] M. Markl, M.T. Draney, D.C. Miller, "Time-resolved three-dimensional magnetic resonance velocity mapping of aortic flow in healthy volunteers and patients after valve sparing aortic root replacement," *J. Thorac. Cardiovasc. Surg.,* vol. 130, pp. 456-63, 2005.

[16] H.J. Pelc, M.A. Bernstein, A. Shimakawa, "Encoding strategies for three-direction phase-contrast MR imaging of flow," *J. Magn. Reson. Imaging,* vol. 1, pp. 405-13, 1991.

[17] J.R. Cebral, C.M. Putman, M.T. Alley, T. Hope, R. Bammer, F. Calamante, "Hemodynamics in normal cerebral arteries: qualitative comparison of 4D phase-contrast magnetic resonance and image-based computational fluid dynamics," *J. Eng. Math.,* vol. 64, pp. 367-378, 2009.

[18] F.P. Glor, J.J.M. Westenberg, J. Vierendeels, M. Danilouchkine, P. Verdonck, "Validation of the coupling of magnetic resonance imaging velocity measurements with computational fluid dynamics in a U bend," *Artif. Organs.* vol. 26, pp. 622-635, 2002.

[19] V.L. Rayz, L. Boussel, B.G. Acevedo, A.J. Martin, W.L. Young, M.T. Lawton, R. Higashida, D. Saloner, "Numerical simulations of flow in cerebral aneurysms: Comparison of CFD results and in vivo MRI measurements," *J. Biomech. Eng.,* vol. 130, pp. 051011, 2008.

[20] L. Boussel, V. Rayz, A. Martin, G.A. Bolton, M.T. Lawton, R. Higashida, W.S. Smith, W.L. Young, D. Saloner, "Phase Contrast MRI measurements in intra-cranial aneurysms in-vivo of flow patterns, velocity fields and wall shear stress: A comparison with CFD," *Magn. Reson. Med.,* vol. 61 pp. 409-417, 2009.

[21] J.A. Moore, D.A. Steinman, D.W. Holdsworth, C.R. Ethier, "Accuracy of computational hemodynamics in complex arterial geometries reconstructed from magnetic resonance imaging," *Ann. Biomed. Eng.,* vol. 27, pp. 32-41, 1999.

[22] M. Zhao, H.S. Amin, S. Ruland, A.P. Curcio, L. Ostergren, F.T. Charbel, "Regional cerebral blood flow using quantitative MR angiography," *Am. J. Neuroradio.,* vol. 28, pp. 1470–1473, 2007.

[23] J.R. Cebral, M. Castro, J. Burgess, R. Pergolizzi, M. Sheridan, C.M. Putman, "Characterization of cerebral aneurysms for assessing risk of rupture by using patient-specific computational hemodynamics models," *Am. J. Neuroradiol.,* vol. 26, pp. 2550–2559, 2005.

[24] K. Funamoto, T. Hayase, A. Shirai, Y. Saijo, T. Yambe, "Fundamental study of ultrasonic-measurement-integrated simulation of real blood flow in the aorta," *Ann. Biomed. Eng.,* vol. 33, pp. 415-428, 2005.

[25] M. D'Elia, M. Perego, A. Veneziani, "A variational data assimilation procedure for the incompressible Navier-Stokes equations in hemodynamics," *J. Sci. Comput.,* vol. 52, pp. 340-359, 2012.

[26] K. Funamoto, T. Hayase, "Reproduction of pressure field in ultrasonic-measurement-integrated simulation of blood flow," *Int. J. Numer. Math. Biomed. Eng.,* vol. 29, pp. 726-740, 2013.

[27] M. D'Elia, A. Veneziani, "Uncertainty quantification for data assimilation in a steady incompressible navier-stokes problem," *ESAIM: M2AN,* vol. 47, pp. 1037-1057, 2013.

[28] J.R. Cebral, R. Lohner, "From medical images to anatomically accurate finite element grids," *Inter. Jour. Numer. Meth. Eng.,* vol. 51, pp. 985-1008, 2001.

[29] R.S. Danturthi, L.D. Partridge, V.T. Turitto, "Hemodynamics of intracranial aneurysms: Flow simulation studies*," Biomed. Eng. Conf. Proc.,* pp. 224-227, 1997.

[30] M. Oshima, T. Kobayashi, K. Takagi, "Biosimulation and visualization effect of cerebrovascular geometry on hemodynamics," *Ann. NY. Acad. of Science,* pp. 972:337-344, 2002.

[31] V.L. Rayz, L. Boussel, B.G. Acevedo, A.J. Martin, W.L. Young, M.T. Lawton, R. Higashida, D. Saloner, "Numerical simulations of flow in cerebral aneurysms: Comparison of CFD results and in vivo MRI measurements," *J. Biomech. Eng.,* vol. 130, pp. 051011, 2008.

[32] G. Paal, A. Ugron, I. Szikora, I. Bojtar, "Flow in simplified and real models of intracranial aneurysms," *Int. J. Heat and Fluid Flow,* vol. 28, pp. 653-664, 2007.

[33] I.C. Campbell, J. Ries, S.S. Dhawan, A.Q. Quyyumi, R.R. Taylor, J.N. Oshinski, "Effect of inlet velocity profiles on patient-specific computational fluid dynamics simulations of the carotid bifurcation," *J. Biomech. Eng.,* vol. 134, 2012.

[34] S. Omodaka, T. Inoue, K. Funamoto, S. Sugiyama, H. Shimizu, T. Hayase, A. Takahashi, T. Tominaga, "Influence of surface model extraction parameter on computational fluid dynamics modeling of cerebral aneurysms," *J. Biomech.,* vol. 45, pp. 2355-2361, 2012.

[35] J.B. Paul, "A method for registration of 3D shapes," *IEEE Trans. on Pattern Analy. Mach. Intelligence,* vol. 14, pp. 239-256, 1992.

[36] T. Ishikawa, Guimaraes, S. Oshima, R. Yamane, "Effect of non-Newtonian property of blood on flow through stenosed tube," *Fluid Dyn. Res.*, vol. 22, pp. 251-264, 1998.

[37] D.A. Steinman, J.S. Milner, C.J. Norley, S.P. Lownie, and D.W. Holdsworth, "Image-based computational simulation of flow dynamics in a giant intracranial aneurysm," *AJNR Am. J. Neuroradiol.,* vol.24, no. 4, pp.559-66, 2003.

[38] H. Amitani, T. Otani, Y. Watanabe, H. Miyazaki, S. Wada, "Analysis of cerebral blood flow fusion between PC-MRI measurement and CFD simulation," *Kansai Stud. Assoc. Grad. Reserch. Pres.,* Pp. 4-7, 2012.

[39] A. Sorteberg, D. Farhoudi, "The influence of aneurysm configuration on intra-aneurysmal pressure and flow," *Interventional Neuroradiology,* vol. 12, pp. 203-214, 2006.

[40] Y. Hoi, H. Meng, S.H. Woodward, B.R. Bendok, R.A. Hanel, L.R. Guterman, L.N. Hopkins, "Effects of arterial geometry on aneurysm growth: three- dimensional computational fluid dynamics study," *J. Neurosurg.,* vol. 101, pp. 676–681, 2004.

[41] Y. Hoi, S.H. Woodward, M. Kim, D.B. Taulbee, H. Meng, "Validation of CFD simulations of cerebral aneurysms with implication of geometric variations," *J. Biomech. Eng.,* vol. 128, pp. 844–851, 2006.

[42] A.C. Benim, A. Nahavandi, A. Assmann, D. Schubert, P. Feindt, S.H. Suh, "Simulation of blood flow in human aorta with emphasis on outlet boundary conditions," *App. Math. Modelling,* vol. 35, pp. 3175-3188, 2011.

[43] P. Bokov, P. Flaud, A. Bensalah, J.M. Fullana, M. Rossi, "Implementing boundary conditions in simulations of arterial flows," *J. Biomech. Eng.,* vol. 135, pp. 111004, 2013.

[44] A. Marzo, P. Singh, I. Larrabide, A. Radaelli, S. Coley, M. Gwilliam, I.D. Wilkinson, P. Lawford, P. Reymond, U. Patel, A. Frangi, D.R. Hose, "Computational hemodynamics in cerebral aneurysms: The effects of modeled versus measured boundary conditions," *Ann. Biomed. Eng.,* vol. 39, pp. 884-896, 2011.

[45] A. Ugron, G. Paal, "On the boundary conditions of cerebral aneurysm simulations," *Periodica Polytechnica Mech. Eng.,* vol. 58, pp. 37-45, 2014.

[46] I. Marshall, S.Z. Zhao, P. Papathanasoppilou, P. Hoskins, X.Y. Xu, "MRI and CFD studies of pulsatile flow in healthy and stenosed carotid bifurcation models," *J. Biomech.,* vol. 37, pp. 679-687, 2004.

[47] P. Papathanasopoulou, S.Z. Zhao, U. Kohler, M.B. Robertson, Q. Long, P. Hoskins, X.Y. Xu, I. Marshall, "MRI measurement of time-resolved wall shear stress vectors in a carotid bifurcation model, and comparison with CFD predictions," *J. Magn. Reson. Imag.,* vol. 17, pp. 153–162, 2003.

[48] S.M. Chitanvis, G. Hademenos, W.J. Powers, "Hemodynamic assessment of the development and rupture of intracranial aneurysms using computer simulation," *Neuro. Res.,* vol. 17, pp. 426-434, 1995.

[49] J.J. Heys, T.A. Manteuffel, S.F. McCormick, M. Milano, J. Westerdale, M. Belohlavek, "Weighted least-squares finite elements based on particle imaging velocimetry data," *J. Comput. Phys.,* vol. 229, pp. 107–118, 2010.

[50] J. Tiago, A. Gambaruto, A. Sequeira, “Patient-specific blood flow simulations: setting dirichlet boundary conditions for minimal error with respect to measured data,” *Math. Model. Nat. Phenom.* vol. 9, pp. 98–116, 2014.

[51] G.D. Weymouth, D.K.P. Yue, “Boundary data immersion method for cartesian-grid simulations of fluid-body interaction problems,” *J. Comput. Phys.* vol. 230, pp. 6233–6247, 2011.

[52] C.W. Hirt, B.D. Nichols, “Volume of fluid (VOF) method for the dynamics of free boundaries,” *J. Comput. Phys.,* vol. 39, pp. 201–225, 1981.

[53] J. Jiang, K. Johnson, S.K. Valen, K.A. Mardal, O. Wieben, C. Strother, “Flow characteristics in a canine aneurysm model: a comparison of 4d accelerated phase-contrast MR measurements and computational fluid dynamics simulations,” *Med. Phys.,* vol. 38, pp. 6300–6312, 2011.

[54] Y. Ujihara, M. Nakamura, H. Miyazaki, S. Wada, “Proposed spring network cell model based on a minimum energy concept”, *Ann. Biomed. Eng.,* vol. 38, pp. 1530-1538, 2010.

[55] R. Bergevin, M. Soucy, H. Gagnon, D. Laurendeau, “Towards a general multiview registration technique,” *IEEE Trans. on Pattern Anal. and Mach. Intelligence*, vol. 18, pp. 540-547, 1996.

LIST OF PUBLICATIONS

Journal Papers

1) Satoshi Ii, **Mohd Azrul Hisham Mohd Adib**, Yoshiyuki Watanabe, Shigeo Wada, "A feedback control based data assimilation method for a patient-specific blood flow analysis", International Journal for Numerical Methods in Biomedical Engineering (IJNMBE), ~ *Under Revision*.

2) **Mohd Azrul Hisham Mohd Adib**, Satoshi Ii, Yoshiyuki Watanabe, Shigeo Wada, "Minimizing the blood velocity differences between phase contrast magnetic resonance imaging and computational fluid dynamics simulations in cerebral arteries and aneurysms", Medical & Biological Engineering & Computing (MBEC), vol. 55, no.3, pp.1-15, 2017.

International Conference (Review)

1) **Mohd Azrul Hisham Mohd Adib**, Satoshi Ii, Yoshiyuki Watanabe, Shigeo Wada, "Patient-specific blood flows simulation on cerebral aneurysm based on physically consistency feedback control", IEEE 16th International Conference on Bioinformatics and Bioengineering (IEEE-BIBE), Taichung, Taiwan, pp. 334-337, 2016.

International Conferences

1) **Mohd Azrul Hisham Mohd Adib**, Satoshi Ii, Yoshiyuki Watanabe, Shigeo Wada, "Patient-specific blood flows simulation on cerebral aneurysm based on physically consistency feedback control", 29th Bioengineering Conference, Nagoya, Japan, pp. 1-2, 2017.

2) **Mohd Azrul Hisham Mohd Adib**, Satoshi Ii, Yoshiyuki Watanabe, Shigeo Wada, "Error estimation of blood flow velocities in the cerebral artery between PC-MRI measurement and CFD simulation: Effect of the extracted geometries and boundary conditions", International Forum Medical Imaging in Asia (IFMIA), Tainan, Taiwan, OS. 1 (462), pp. 1-4, 2015.

3) **Mohd Azrul Hisham Mohd Adib**, Satoshi Ii, Yoshiyuki Watanabe, Shigeo Wada, "Effect of extracted geometries with different threshold image intensities on the patient-specific blood flow analysis with the PC-MRI based data assimilation technique", 27th Bioengineering Conference, Niigata, Japan, pp. 1-2, 2015.

ACKNOWLEDGEMENTS

Alhamdulillah. Foremost, I wish to express my deepest thankfulness to my supervisor Professor Dr. Shigeo Wada for his great supervision throughout this study and providing me numerous opportunities for growth. The whole work was carried out under his supervision in his laboratory (Biomechanics Lab.) at the Graduate School of Engineering Science, Osaka University.

I would like to express my gratitude to Associate Professor Dr. Satoshi Ii for valuable discussions about the numerical computational methodologies and critical comments throughout this study. He also continuously teach me for high research skill.

I am deeply grateful to the following collaborator at Department of Radiology, Graduate School of Medicine, Osaka University, with Associate Professor Dr. Yoshiyuki Watanabe for providing me lots of clinical data and clinical motivation to tackle in this study.

I sincerely thank Professor Dr. Kazuyasu Sugiyama and Professor Dr. Masao Tanaka for their support as the thesis defense committee members. It is a great chance for me to have a discussion with the expert in their field of study and give me the informative comments to improve the quality of this thesis.

I am pleasured to thank Associate Professor Dr. Kenichiro Koshiyama for critical comments and continuous encouragements for both research and private topics.

My sincere thanks go to all my labmates from Biomechanics Lab (Wada Lab), who helped me in many ways and made my stay at Osaka pleasant and unforgettable.

I would like to acknowledge special thanks to my beautiful wife, Nur Hazreen Binti Mohd Hasni for her great understanding and support and for taking care our kids Muhammad Akhtar Haziq and Muhammad Arsyad Hazim when I was busy working in this research.

I acknowledge my sincere indebtedness and gratitude to my parents Hj. Mohd Adib Bin Mat Yacob and Hjh. Zawiyah Binti Md. Ariff for their love, dream and sacrifice thoughout my life. I acknowledge the sincerity of my parent-in-law Mohd Hasni Bin Mat Hassan and Wan Zaihan Binti Wan Ab. Rahman, who consistently encouraged me to carry on my higher studies in Japan. Also, thanks to my brother Mohd Aidinniza Bin Mohd Adib and my sister Noor Azliza Binti Mohd Adib for their assistance since I was little.

And finally, I would like to thanks, Universiti Malaysia Pahang (UMP) and Kementerian Pendidikan Malaysia (KPM) for providing scholarship and for giving me this opportunity to pursue this qualification. Coming from a middle family would make me remember this contribution.

Mohd Azrul Hisham Bin Mohd Adib

Department of Mechanical Science and Bioengineering

Graduate School of Engineering Science

Osaka University